Dynamics of Anions Probed by Photoelectron Imaging

LAURENCE HARRY STANLEY

Dynamics of Anions Probed by Photoelectron Imaging

Laurence Harry Stanley

Department of Chemistry

University of Durham

2017

A thesis submitted in partial fulfilment of the requirements for the degree of *Doctor of Philosophy*.

Declaration

The material contained within this thesis has not previously been submitted for a degree at the University of Durham or any other university. The research reported within this thesis has been conducted by the author unless indicated otherwise.

Copyright Notice

Abstract

This work comprises of the design and construction of a novel ion trap and guide system for the existing photoelectron spectrometer along with the study of two molecular systems.

The redesigning of the system was to address shortcomings in the previous design and to open the door to new possibilities of research. The new components have been installed and proof-of-concept data has been taken that shows the success of the new cryogenic cooling system upon the ions.

The anionic resonances of anthracene, a polyaromatic hydrocarbon (PAH), were studied using the new apparatus. This allowed for the use of a new methodology to produce ions of interest that were previously impossible to study. While we found that photodissociation gave better regioselectivity, it was possible to generate the most stable deprotonated from of the anthracenyl anion. Considering the formation of the anions in the interstellar medium, it was shown that it is likely that the anthracenyl resonances preferred to decay by autodetachment. This would result in little formation of the anion from the approach of an electron upon the neutral.

The chromophore of the Green Fluorescent Protein (GFP) has been extensively studied by other researchers. We investigated the dynamics of an isomer of that chromophore. The movement of a single functional group from the para- to the meta- position completely alters the energetics of the system along with the dynamics. It was shown that this structural change would make for a significantly poorer choice as a chromophore for a fluorescent protein.

Acknowledgements

It is said that no man is an island and the completion of a PhD thesis is no exception, and as such I would like to take the opportunity to thank the following people:

Firstly, I must express my thanks to my supervisor, Jan. Without your guidance, contribution, and significant patience this work would have been vastly less comprehensive and significantly poorer for it!

I must also thank those I have worked with on my experiment, Chris West and James Bull, with a special thanks to Cate Anstöter for her computational work.

Next, I would like to acknowledge my father, William for his invaluable discussions of possible electronic solutions, especially during the deeply frustrating period once the instrument had been rebuilt but was stubbornly refusing to detect any signal. Articulating the issues with the system helped considerably in finding solutions to the problem.

Outside of work I must thank my significant other, Meg, for her continued support at all times during this work. Similarly, I am grateful that my parents have been so understanding while I've been doing this. Your enduring belief in me has managed to make this whole process a lot more bearable – though I'd rather not do it again!

A final thank you to all my friends who have helped keep me (mostly) socially adjusted with a special thanks to my fellow PhD-survivors!

Contents

1. Introduction

This chapter provides a review of the techniques used in this thesis and the energy storage mechanisms and transfer mechanisms of molecules studied during the course of this work.

1.1. Temperature and Statistical Mechanics

Understanding the fundamentals of the processes of chemistry is to consider energy; how much and where is it going? Knowing the answers to both questions will inherently describe many of the particulars of any given reaction. Answering the first question is generally the simpler – knowing the initial conditions of our reactions provides a reasonable estimate of the amount of energy available. However, a moment's consideration reveals this to be only an estimate. Given the inherent inaccuracy of an estimation, the assumptions made to produce it need to be examined thoroughly.

One can consider a reaction from two extreme perspectives – that of molecules or that of mixing two bulk substances together. The latter involves easily measured quantities (e.g. temperature, pressure, volume) and forms the macroscopic description of the system. Linking the large-scale phenomena with the experience of the individual molecules is the basis of statistical mechanics.

Statistical mechanics began with classical thermodynamics which primarily concerns itself with macroscopic properties of systems in equilibrium.[1] However, in doing so, thermodynamics neglects the details of molecular or atomic structure. Thus, it is impossible from this framework alone to draw any conclusions about the underlying molecules and their behaviour. However, even for molecularly complicated systems, the thermodynamic relations hold true.

The connection between how classical thermodynamics succeeded at predicting macroscopic quantities without a microscopic viewpoint is down to the statistics of large groups and degeneracy.* Avogadro's number (6×10^{23} mol^{-1}) defines the number of particles in a mole and highlights the reasoning behind using a statistical approach. It is obvious when considering a group of particles of even modest size that there are vast numbers of ways to arrange the energy across the group.

* In the physics sense – of being in the same state. Not the other meaning. This isn't that sort of thesis.

This consideration of possible states of the system is the ensemble and which properties are fixed defines the ensemble.[2] Most ensembles have 3 defined quantities, such as: volume (*V*), temperature (*T*), number of particles (*N*), total energy (*E*), and pressure (*p*). Every ensemble has a central statistical thermodynamic function that is present in all expressions for thermodynamic properties – this is the partition function.

Putting all this together for a system starts to demonstrate the various possibilities of energy storage. The simplest system to model would be an ideal monatomic gas – the results of which hold true for helium under many circumstances. Given the ideal gas law,

$$pV = Nk_{\mathrm{B}}T \ , \tag{1.1}$$

and that the canonical ensemble is defined by *N*, *V*, and *T*, the canonical ensemble will be used for this discussion.[1,3] Such a system has 3 forms of energy storage. The standard form of the canonical partition function is:

$$Q(N,V,T) = \sum_j e^{-\frac{E_j(N,V)}{k_{\mathrm{B}}T}} \ , \tag{1.2}$$

where *j* is a state and thus E_j is the energy of the *j*-th state.[1] The eigenvalues of $E_j(N,V)$ would ideally be those of an *N*-body Schrödinger equation. However, this is impossible to solve exactly.

The simplest way to resolve this is to split the Hamiltonian into its various degrees of freedom,

$$\hat{H} \cong \hat{H}_{\mathrm{trans}} + \hat{H}_{\mathrm{elec}} + \hat{H}_{\mathrm{nuc}} \, . \tag{1.3}$$

This allows the partition function to be evaluated as,

$$q(V,T) = q_{\mathrm{trans}} q_{\mathrm{elec}} q_{\mathrm{nuc}} \ , \tag{1.4}$$

where q_{trans} is the partition function for the translational degrees of freedom, q_{elec} is the partition function for the electronic degrees of freedom, and q_{nuc} is the

partition function for nuclear degrees of freedom.[1†] Of these, only the first two are of interest under most conditions. The reason is the degree of separation between energy levels that describe the various degrees of freedom. The energy separation for nuclear energy states is of the order of 10^6 eV, thus to have even 1% of a group in the first excited nuclear state would require temperatures in the region of 10^{10} K.[1] When considering q_{elec}, the contributions from excited states are often negligible due to their energy relative to the ground state. For helium, our simplest case, the difference between the ground state, $^1S_0$, and the first excited state, $^3S_1$, is nearly 20 eV.[4] This means that for a 1% probability of finding He in its $^3S_1$ state, the temperature would need to be around 5×10^4 K. There are situations where the energy gap is considerably less, and these will be covered later. Finally, there is the translational energy contribution. The energy gaps between the translational levels are the smallest of all. Considering the simplest quantum system, a particle in an infinitely deep 3D cubic well, gives the energy levels to be:

$$E_{\text{trans}} = \frac{h^2(n_x^2 + n_y^2 + n_z^2)}{8mL^2}\ , \tag{1.5}$$

where n_x, n_y, n_z are the quantum numbers in each of the three Cartesian coordinates, *m* is the mass of the particle, and *L* is the length of the side of the cubic container.[1] The one-dimensional equivalent has energy levels that become further apart as the energy increases because the levels are proportional to n^2. However, the 3D box has inherent degeneracy due to the independence of the three quantum numbers. This allows for the density of states to increase faster than the gap between levels as can be seen in Figure 1.1. For very large values of *n*, the degeneracy is proportional to $\sqrt{E}$.[1]

Attempting to evaluate the sum of the partition function directly runs into a problem; the total is impossible to express as an analytical function. This could be rectified by considering the summation as continuous rather than discrete and performing an integration. To do this, it is worth evaluating the difference between

† As this is considering a single atom, this nuclear component is the internal energy states of the nucleus. When discussing relative nuclear motion in section 1.1.1, more terms will be described.

sequential energy levels to establish the validity of this approach. The difference in the exponential argument in eq. (1.2) going from *n* to (*n* +1), Δ, is:

$$\Delta = \frac{h^2 (n+1)^2}{8mk_B TL^2} - \frac{h^2 n^2}{8mk_B TL^2} = \frac{h^2 (2n+1)}{8mk_B TL^2} , \tag{1.6}$$

where *n* is any of the above quantum numbers. Substituting values in for helium in a cubic meter box at 300 K this reduces to:

$$\Delta \cong (2n+1) \times 10^{-20} . \tag{1.7}$$

Assuming all three quantum numbers to be the same gives an estimate of the magnitude of *n* for an average helium atom:

$$n_{\text{average}} \approx 10^9 . \tag{1.8}$$

This shows that for the average molecule in this situation, the discrete nature of the partition function can be neglected in favour of a continuous approach. Assuming a value of $\Delta \approx 10^{-5}$ as a point where the assumption might fail, would imply a molecule having $10^{10} k_B T$ of translational energy.[1] This demonstrates that extreme systems are required before the discrete nature of this summation becomes in any way noticeable.

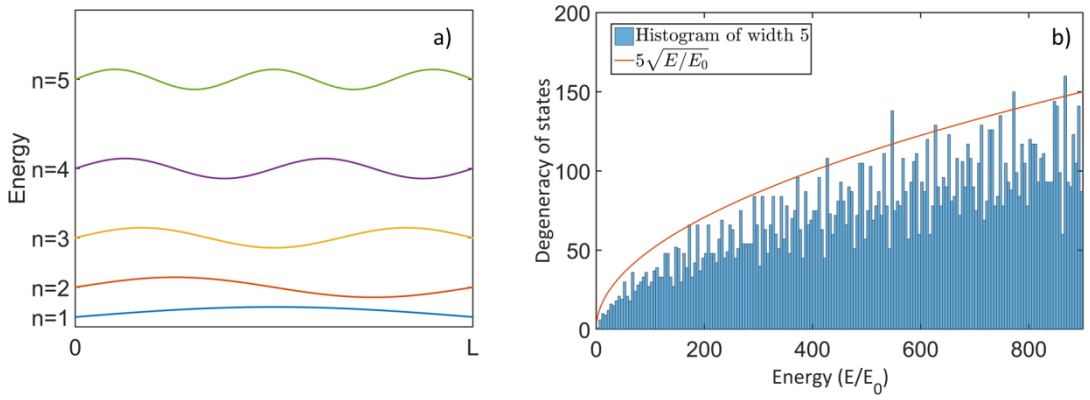

Figure 1.1 Relative energy levels of an infinitely deep square potential well. a) Initial wavefunction shape plotted at the energy level for the ground state and the first 4 excited states of the one-dimensional well. b) Histogram of the degeneracy of translational states in a 3D infinite square well. Also shown is a constant-adjusted curve that predicts the degeneracy for large values of n.

Considering the sum of eq. (1.2) as an integral of the form:

$$\int_0^\infty e^{-an^2} dn = \sqrt{\frac{\pi}{4a}} \ , \tag{1.9}$$

results in

$$q_x = \frac{\sqrt{2\pi m k_B T}}{h} L = \frac{L}{\Lambda} \ , \tag{1.10}$$

where Λ is known as the thermal de Broglie wavelength.[1] As the Cartesian coordinates are independent, the partition functions can simply be multiplied to give the familiar form,

$$q_{trans} = q_x q_y q_z = \frac{L^3}{\Lambda^3} = \frac{V}{\Lambda^3} \ . \tag{1.11}$$

This result allows a check on statistics – the above are based on simple Boltzmann statistics. [1] Both of the two quantum statistical distributions tend to a classical Boltzmann distribution under high temperature or low density. This implies that the number of available states is much greater than the number of particles. Thus, the likelihood of multiply-occupied states is low. One methodology of testing this is evaluating the translational partition function as shown above. The condition is that

$$\frac{\Lambda^3}{V} \ll 1 \ . \tag{1.12}$$

Thus, if the translational partition function is sizeable then classical statistics are justified.

1.1.1. Rotation and Vibration

Moving to consider a slightly more complex system opens new energy storage possibilities. This is easily demonstrated by considering a diatomic gas. Immediately this makes use of two new degrees of freedom, rotation and vibration, for which

we can define partition functions q_{rot} and q_{vib} , respectively. However, it also opens up a different problem – more atoms and bonds.

To evaluate and consider the vibrational and rotational partition functions and therefore their relative contribution to thermal effects, we need to know their relative energy. However, to solve the Schrödinger equation for that many bodies and interactions is impossible with exact methods. The first approximation to be made is the Born-Oppenheimer approximation. [1] It allows the motion of the nuclei and the electrons to be considered separately. The logic is that the huge difference in mass between the nuclei and the electrons, $\left(\frac{m_{\text{proton}}}{m_{\text{electron}}}\right) \cong 1800$, means that the electronic motion can be calculated relative to stationary nuclei. [2] Considering the mutual attraction and that $\text{acceleration} = \frac{\text{force}}{\text{mass}}$, this means that the electrons will be experiencing accelerations three orders of magnitude greater than the nuclei.

The Born-Oppenheimer approximation splits the Schrödinger equation into two parts – one that describes the motion of the electrons in the field of the fixed nuclei, the other the motion of the nuclei in the electronic potential set up by the electrons. [2] This latter is the sum of the all the contributions from the individual states which each have a characteristic internuclear potential.

As with all approximations, there are some situations where the assumptions are invalid. This assumption breaks when there is significant coupling between the movement of the electrons and the nuclei and there is only a small energy gap between two electronic states. Many of these are true when considering chemical dynamics, however it allows for a meaningful discussion due to the predictions of the adiabatic states.

Applying the Born-Oppenheimer approximation to the problem of rotational and vibrational partition functions moves the methodology forward but we again encounter a problem. A way to visualise the situation is to consider the motion as the combination of two separate processes, the motion of the centre of mass and the relative motion of the individual atoms relative to this centre. Given that the

frequency of the vibrations is much faster than that of the rotations, a further approximation is made.[5] The rotational motion is considered for a rigid "dumbbell" of fixed length as the vibrational motion will be averaged out. The vibrational motion is considered totally separately to that of the rotational and is known as the rigid rotor-harmonic oscillator approximation, so that the total partition function can be written as:

$$q(V,T) = q_{\text{trans}} q_{\text{rot}} q_{\text{vib}} q_{\text{elec}} q_{\text{nuc}} \ . \tag{1.13}$$

This is in order of increasing energy.

The energy levels for rotation of a diatomic molecule are given by:

$$E_{\text{rot}} = BJ(J+1) \text{ where } B = \frac{h^2}{8\pi^2 I} \ , \tag{1.14}$$

B is the rotational constant for the molecule, which is defined by its moment of inertia, *I*.[1] When it comes to computing the partition function based on this, the degeneracy of the states becomes important. The sum is:

$$q_{\text{rot}} = \sum_{J=0} (2J+1) e^{-\frac{BJ(J+1)}{k_B T}} \ . \tag{1.15}$$

Another useful measurement is the rotational temperature, defined by:

$$\Theta_{\text{rot}} = \frac{h^2}{8\pi^2 k_B I} = \frac{B}{k_B} \ . \tag{1.16}$$

Mathematically, the solution to eq.(1.15) is impossible to write in a closed form. However, if considered as an integral similar to eq. (1.9), a simple result emerges:

$$q_{\text{rot}} = \frac{T}{\Theta_{\text{rot}}} \ . \tag{1.17}$$

The simplicity of this result is due to the assumptions made.[1] It is only valid for temperatures of molecules where *T* is considerably larger than the characteristic temperature of rotation. Furthermore, when considering homonuclear diatomics,

this result overestimates the number of accessible states. A symmetry number, σ, is used to correct for this – for which it has the value of 2 for homonuclear diatomics,

$$q_{\text{rot}} = \frac{T}{\Theta_{\text{rot}}\sigma} \ . \tag{1.18}$$

Vibrational motion can be considered similarly, with the energy levels being:

$$E_{\text{vib}} = \left(v + \frac{1}{2}\right) h\nu_{\text{e}} \ , \tag{1.19}$$

where v is the vibrational quantum number and ν_{e} is the vibrational frequency.[1] The characteristic temperature of vibration is defined as:

$$\Theta_{\text{vib}} = \frac{h\nu_{\text{e}}}{k_B} \ . \tag{1.20}$$

When considering the partition function, the geometric series converges to:

$$q_{\text{vib}} = e^{-\frac{\Theta_{\text{vib}}}{2T}} \sum_{n=0}^{\infty} e^{-\frac{n\Theta_{\text{vib}}}{T}} = \frac{e^{-\frac{\Theta_{\text{vib}}}{2T}}}{1 - e^{-\frac{\Theta_{\text{vib}}}{T}}} \ .^{1} \tag{1.21}$$

While all the above expressions are derived for a diatomic, the fundamental mechanics are the same for polyatomic systems. Instead of a single vibrational mode there are several in a polyatomic molecule. For a non-linear polyatomic there are three degrees of rotational freedom that each contribute.

1.1.2. A Large Polyatomic Example

To illustrate the distribution of energy among various vibrational modes, we consider the chromophore of the green fluorescent protein (GFP), which is often taken to be the anion of para-hydroxybenzilidene-2,3-dimethylimidazolinone ($HBDI^-$), a molecule previously studied by this lab and shown in Figure 1.2.[6]

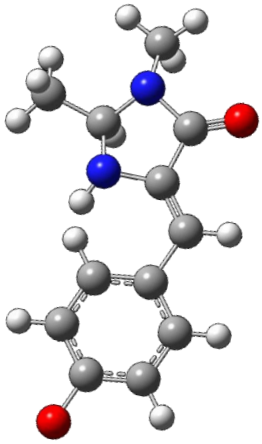

Figure 1.2 Ball-and-stick representation of the 4-(*para*hydroxybenzylidene)-5-imidazolinone (*para*-HBDI) anion.

The fundamental frequencies of the vibrational modes have been calculated previously using density functional theory (DFT) at the CAM-B3LYP/aug-cc-pVDZ level of theory.[7] As this molecule is non-linear, the formula for the number of degrees of freedom and vibrational modes, α, is:

$$\alpha = 3N - 6 \ , \tag{1.22}$$

with N as the number of atoms in the molecule.[1] For $HBDI^-$, we would therefore expect 75 different vibrational modes, due to 27 atoms. Each mode has its own distribution associated with it at a given temperature. Considering the relative energies of the modes in terms of the vibrational temperature defined in eq. (1.20), they range non-linearly from 67 K (47 cm^{-1}) to 4629 K (3217 cm^{-1}). The amount of energy stored in vibration is given by:

$$E_{\text{vib}} = k_{\text{B}} \sum_{j=1}^{\alpha} \left(\frac{\Theta_{\text{vib}\,j}}{2} + \frac{\Theta_{\text{vib}\,j} e^{-\frac{\Theta_{\text{vib}\,j}}{T}}}{1 - e^{-\frac{\Theta_{\text{vib}\,j}}{T}}} \right), \tag{1.23}$$

where j denotes the vibrational mode and $\Theta_{\text{vib}\,j}$ as the vibrational temperature for that mode.[1] This sum also includes the zero-point energy in the $\frac{\Theta_{\text{vib}\,j}}{2}$ terms.

While this is entirely accurate, for the purposes of clarity, the constant offset present from the zero-point energy will be subtracted to consider a relative energy. The relative energy thus given is a measure of the way that the energy distribution within the vibrational manifold changes as the temperature changes. Unsurprisingly, the whole trend is some form of exponential, but the actual values are more relevant in this case.

Table 1.1 The relative energy present in vibrational modes for the molecule para-hydroxybenzilidene-2,3-dimethylimidazolinone at various temperatures.

Temperature (K)	Relative Energy (eV)
10	8×10^{-6}
80	0.02
150	0.08
300	0.3

Previous work from this lab has been conducted at a minimum of ~298 K.[8] The ions underwent no thermal alterations from their surroundings – the previous equipment had neither heating nor cooling capability for the ions in the trap. However, upon extraction, it is likely that some collisions occurred after considerable acceleration. This will be discussed more thoroughly in the experimental chapter. At 300 K the relative vibrational energy is ~ 0.3 eV. For comparison, the average translational energy of a molecule at 300 K is 0.03 eV.

The amount of energy available to the molecule defines the likelihood of excited level occupation for each of the 75 different available vibrational modes. Considering the distribution of excited vibrational levels makes the thermal difference particularly clear. The proportion of molecules in vibrational energy levels above v = 0 for each mode is given by:

$$f_{v>0} = 1 - f_0 = e^{-\frac{\Theta_{vib}}{T}}.^{1} \tag{1.24}$$

Plotting the excited vibrational level fraction for a few temperatures is shown in Figure 1.3.

As can be seen in Figure 1.3, at 300 K there is population in excited levels of vibrational modes with characteristic temperatures much greater than 300 K. There is ~10% for a vibrational temperature of 700 K. Contrastingly at 80 K there are only 5 modes with more than 10% population in higher energy levels.

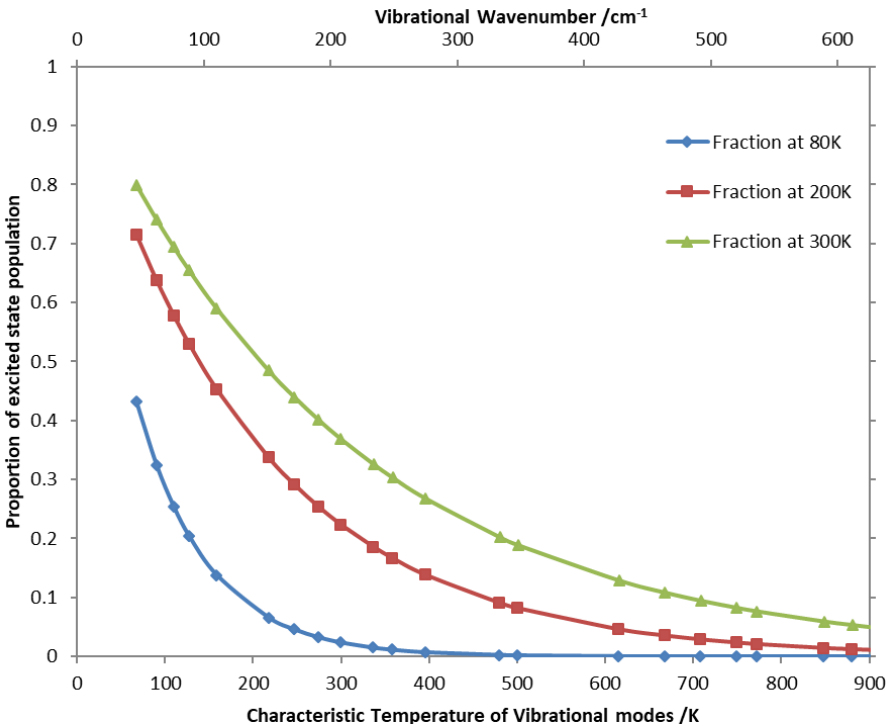

Figure 1.3 Excited state proportions of vibration at 80, 200, and 300K for the para-hydroxybenzilidene-2,3-dimethylimidazolinone anion. The horizontal axis is presented as the vibrational temperature of the various modes.

1.1.3. Angular Momentum & Term Symbols

Electronic states other than the ground state may also contribute to the partition function. Electronic states are usually defined in terms of their term symbols. For an atom, this is

$$^{2S+1}L_J\,, \tag{1.25}$$

where S is the total spin quantum number, J is the total angular momentum quantum number and L is the total orbital quantum number.[2] When considering a

system of monatomic oxygen (deliberately discounting the physical impossibility of this), the possible configurations of the electrons, while confining the electrons to the p orbitals, are shown in Table 1.2.

This shows that monoatomic oxygen gas would have a significant contribution from the first two excited states at room temperature.

Table 1.2 The relative energies and degeneracies of the first 5 states of monoatomic oxygen. T_{av} is the temperature where the average translational energy , $(3/2)k_B T$, is equal to the relative energy shown.[1]

Term Symbol	Degeneracy	Relative energy /eV	T_{av} /K
$^3P_2$	5	0	
$^3P_1$	3	0.02	150
$^3P_0$	1	0.03	220
$^1D_2$	5	1.97	15200
$^1S_0$	1	4.19	32400

The form for the term symbol in a diatomic molecule is more or less the same:

$$^{2S+1}\Lambda^{(+/-)}_{\Omega,(u/g)} , \tag{1.26}$$

where Λ is the projection of the orbital angular momentum along the internuclear axis, Ω is the total angular momentum along the internuclear axis, u/g is the parity and +/– is the reflection symmetry with respect to a plane containing the inter-nuclear axis. [2]

This provides a considerable amount of information about the electronic state of the system. However, for large systems this may be almost impossible to truly define. A simpler example will help illustrate a few useful points. Singlet oxygen describes one of the first two excited states of the oxygen molecule.

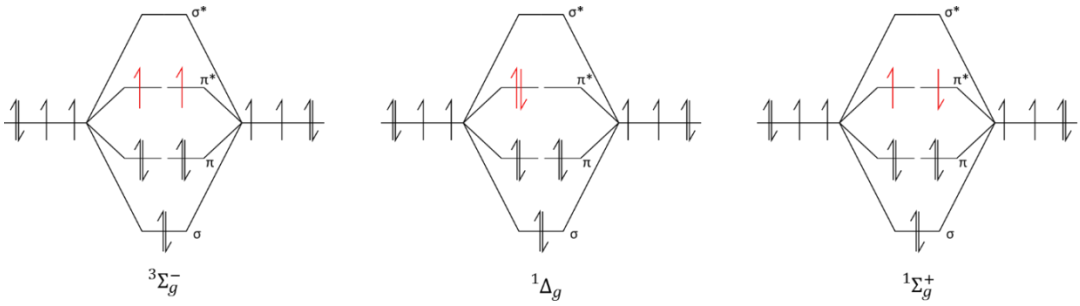

Figure 1.4 The ground state, left, and the first two excited states of molecular oxygen. Increasing in energy from left to right, the first excited state is 0.98 eV and the second is 1.63 eV above the ground state. [9] These would correspond to an average translational energy temperature of 7500 K and 12500 K respectively.

While the electronic configuration of both the excited states displayed in Figure 1.4 lead to singlet states, it is the $^1\Delta_g$ state that is generally referred to by the moniker of singlet oxygen. The $^1\Sigma_g^+$ state is highly reactive and also quickly decays into the $^1\Delta_g$ state.[9] Decay to the ground state is spin forbidden, this means that the lifetime of the $^1\Delta_g$ state is surprisingly long, up to 45 minutes in the gas phase.[10]

1.2. Energy Transfer Mechanisms

All of the above topics discussed thus far have been formulated under thermal equilibrium. While this is entirely valid and contains valuable information about the energy distribution in molecules, many more processes occur when a system is perturbed, such as by the absorption of a photon. While this specific process will be covered more explicitly in Section 1.3.4, here we consider the processes that transfer energy in molecules, in particular those associated with relaxation.

The first distinction to make is between radiative and non-radiative processes. The former involves the emission of electromagnetic radiation. Non-radiative processes involve the transfer of energy between states of the molecule and often also between different forms of energy (e.g. electronic to vibrational). To discuss this further a visual aid is helpful.

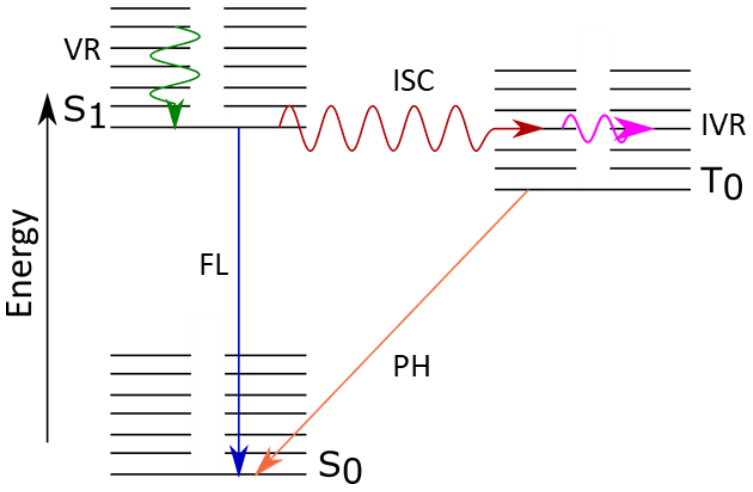

Figure 1.5 Jablonski diagram illustrating different relaxation processes that can occur. This shows intersystem crossing (ISC), red, from one spin state to another; in this case from an excited singlet, S_1, to the lowest triplet state, T_0. There is intramolecular vibrational redistribution (IVR), magenta, from vibrational levels to other isoenergetic vibrational levels. Relatedly there is vibrational relaxation (VR), green, from excited vibrational levels to lower vibrational levels. There is also fluorescence (FL) from one excited electronic state to another of similar spin, blue, and phosphorescence (PH) from one excited state to a lower one of different spin, orange.

The most common form of visual representation of the internal energy processes of a molecule is a Jablonski diagram as shown in Figure 1.5.[11] Radiative processes are

represented as straight arrows while non-radiative processes are represented by squiggly arrows.

1.2.1. Intramolecular Vibrational Redistribution (IVR)

Starting from a vibrationally excited state, a molecule can undergo intramolecular vibrational redistribution (IVR). This process allows for the energy to be distributed over other vibrational modes. If the molecule is isolated and thus cannot lose energy to its surroundings, then the energy stored in the other modes exactly corresponds with that lost from another. [12] However, if the molecule can interact with others nearby, the energy can be redistributed across the system as heat. This process is generally referred to as vibrational relaxation (VR) as the process is irreversible.

How the energy passes between the vibrational modes is primarily due to the shape of the potential wells. When considering the vibrational partition function, the assumption was that the motion was harmonic and of the form r^2, where r is the internuclear distance. [1]

While a harmonic potential makes the mathematical formulation easier and is a good approximation for small amplitude vibrations, as can be seen in Figure 1.6, real molecules have anharmonic potentials such as the Lennard-Jones (L-J) potential shown in Figure 1.6.[13,14] The much shallower gradient extending to larger internuclear spacing arises because eventually, the bond must break.

For small molecules, this redistribution can be reversible,[12] as evidenced by a periodic revival of population in time-resolved experiments.[12,15] When considering a larger molecule, the sheer number of other vibrational levels and modes causes the process to be dephase rapidly and IVR becomes irreversible. This can be considered a statistical process so long as there is a sufficient density of states. The rate of

migration into other levels is then predicted by Fermi's Golden Rule.[16,17] Despite being known as Fermi's rule, most of the preparatory work was done by Dirac.[18]

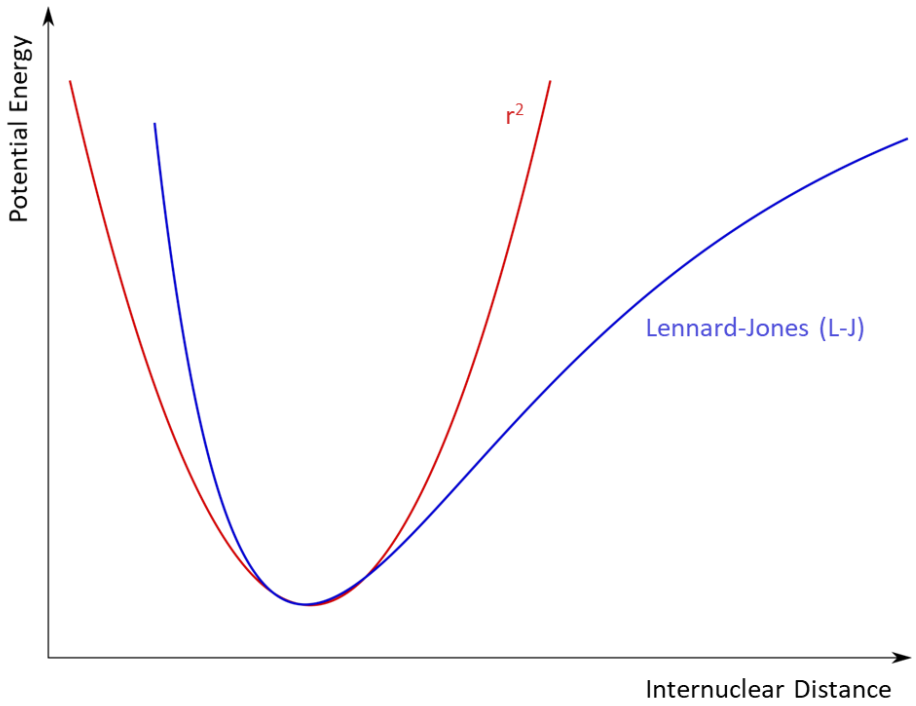

Figure 1.6 Comparison of the r^2 harmonic potential well, in red, and the Lennard-Jones potential in blue. [13]

Fermi's Golden Rule covers the general situation where one state (or vibrational level) is coupled to a large number of similar other states, up to and including a full continuum of states.[2,16] Under these conditions, the rate of transfer from an initial state a can be considered to be:

$$k_{\text{IVR}} = \frac{2\pi}{\hbar}\sum_j \left|V_{aj}\right|^2 \delta(E_a - E_j)\ , \tag{1.27}$$

where E_j is the energy of final states j, $\left|V_{aj}\right|$ is the strength of the coupling between a and j, and $\delta(E_a - E_j)$ is the delta function acting upon the difference in energy between the initial and final state. [2] Given the properties of the delta function, that:

$$\int_{-\infty}^{\infty}\delta(\omega)d\omega = 1 \text{ and } \int_{-\infty}^{\infty} f(\omega)\delta(\omega) = f(0)\,, \tag{1.28}$$

where $f(\omega)$ is any generalised function of ω, a generalised variable, it is no surprise that the summation predicts transitions primarily to states where $E_j \cong E_a$.[16] The derivation of the rate expression comes from considering a perturbation to the potential energy. This requires both that the coupling between the states be small but also that it be much larger than the energy spacing between the final states. Given the large number of the final states that are defined as being almost degenerate, this is easily justified. While the exact couplings between different final states are expected to be different, it is very difficult to practically measure these. Furthermore, often when considering the results of an experiment, it is entirely possible to have a manifold of similar initial states as well as final states. This would be considered as a further sum of the form above but now over all starting states, *a*, as well. When dealing with experimental results, the rate is often expressed as:

$$k_{\text{IVR}} = \frac{2\pi}{\hbar}\left|V_{av}\right|^2 \rho(E_a) \ , \tag{1.29}$$

where V_{av} is the average coupling and $\rho(E_a)$ is the density of final states (at the initial energy).[12]

When comparing competing relaxation pathways, it useful to have some typical values. IVR for many molecules takes place on the timescale of 1 to 10s of picoseconds.[12]

1.2.2. Internal Conversion (IC) & Intersystem Crossing (ISC)

Internal conversion (IC) and intersystem crossing (ISC) are the non-radiative processes that link between different electronic states in a similar manner to the vibrational states of IVR.[17] The difference between IC and ISC is that IC moves between electronic states of the same spin while ISC has a change in spin. A system undergoing IC most often moves population from some vibrational level of an excited electronic state to an excited vibrational level of a lower-lying electronic

state. As energy must be conserved, the electronic energy is changed into vibrational energy, that can then be subject to IVR. The IC mechanism relies on electronic-vibrational coupling and, given that the Born-Oppenheimer approximation explicitly ignores any coupling between the electronic and nuclear motion, this process is clearly non-adiabatic.[17]

The rate of IC can be considered in a similar manner to that of IVR, by a Golden Rule approach, replacing the anharmonic vibrational coupling with an electronic coupling. Often this coupling is assumed to be constant across the states and so the rate becomes dependent on just the overlap of the wavefunction of the vibrational levels. This is the foundation of the Franck-Condon (FC) factor and will be discussed in more detail in section 1.3.4.[16,17,19] As can be expected, some modes are vastly more important than others due to much stronger coupling between initial and end states and these are known as the promoting modes. Experimentally is has been observed that the rate of internal conversion has a dependence on the energy gap between the states, ΔE , and the frequency of the promoting modes, ω : [20,21]

$$k_{\mathrm{IC}} \propto e^{-\frac{\Delta E}{\hbar\omega}} \ . \tag{1.30}$$

Obviously, the more states and modes available to couple to and from, the more efficient this process becomes. A further special case occurs when the states have the same energy, as discussed in the next section.[16,17]

When the two electronic states have differing spin, the process of IC described above is formally forbidden by selection rules. If spin-orbit coupling is considered and is of a sufficient magnitude, this can be overcome and is known as ISC.[2,16,17] As with IC, the overlap of the wavefunctions is important, but now also the spin-orbit interaction. The spin-orbit coupling generally increases going right and down the periodic table, but ISC can occur without particularly heavy elements. A typical timescale for ISC is between 10 ps to some μs, but some systems have a particularly efficient spin state conversion rate, such as the dye molecules in dye-sensitised solar cells.[22] It has also been observed that the presence of paramagnetic species in solution will considerably increase the rate of intersystem crossing.[23]

1.2.3. Conical Intersections (CI)

As alluded to earlier, the rate of IC given by eq.(1.30) has a special case when the energy difference between the states approaches zero. Under these conditions the states are said to have a conical intersection (CI). This situation is completely at odds with the Born-Oppenheimer approximation as there is inherently a strong coupling between the electronic and nuclear modes close to a conical intersection.[17,24,25] When considering the dynamics through such a conical intersection, a mere Jablonksi diagram is insufficient. The potential energy requires consideration as a variable of at least two independent internal coordinates.

A generic conical intersection is shown in Figure 1.7. A molecule traversing the excited state could approach the intersection and quickly couple to the ground state. However, the final product can be in different positions on that ground state surface. The motion though the intersection describes the likelihood of the possible outcomes from the CI.[25] Looking at Figure 1.7 would predict two products, corresponding to departing in opposite directions from the CI roughly along $\overline{Q}_{x_1}$.

For diatomic molecules there is a strict non-crossing rule for two states of the same symmetry, however polyatomic systems can have intersections even between states of the same symmetry and spin multiplicity.[24] When dealing with large system, it becomes clear that while it is simple to visualise the intersection as a point of contact between two surfaces, this is a simplification – the intersection forms a seam in $N-2$ dimensions of the available N nuclear coordinates present in the molecule.[24]

A conical intersection is the fastest variation of internal conversion, allowing for efficient energy conversion to vibrations within the manifold of the lower electronic state. The frequency of the mode present in eq. (1.30) could be viewed in a classical sense as how often the molecule passes through the appropriate geometry. For a conical intersection, the approach to the geometry can be longer in time than that of the passage to the lower electronic state, evidenced by timeframes shorter than

that of a vibrational period.[25,26] A typical timeframe for passage through a conical intersection is in the 10s of femtoseconds.

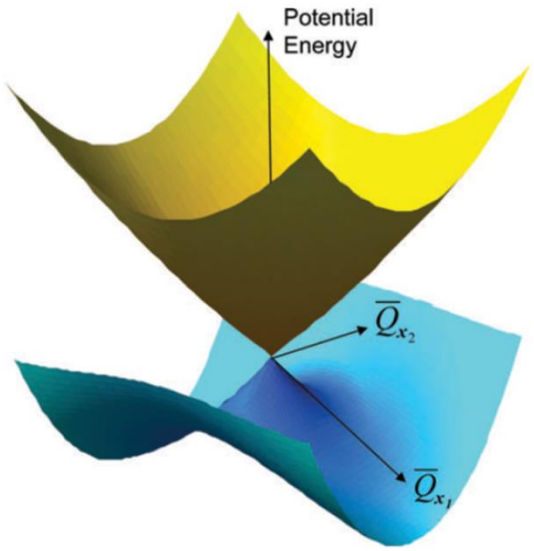

Figure 1.7 Example of a conical intersection, motion across the excited (yellow) state can cause a transition through the intersection with multiple products being possible. Adapted from Ref. 27 with permission of the PCCP Owner Societies.

1.2.4. Radiative Relaxation and Rate Comparison

Luminescent processes allow for the true ejection of energy from an individual molecule. In a manner similar to IC and ISC, the two radiative relaxation processes are different in their total spin conversion.[16,17] Fluorescence takes place between states of the same spin and most likely from the first excited state due to a preference to undergo IC between higher excited states. Phosphorescence takes place with a change in total spin. Both processes occur after the IVR process that operates on a faster timescale than the emission of a photon. The typical timescales of the various processes are shown in Table 1.3.[16,17] Further discussion of absorption/emission of photons will be in Section 1.3.2.

Table 1.3 Comparative timescales of the various excited state relation methods presented above.

Process	Typical timescale (sec)
IC via CI	$10^{-14} - 10^{-13}$
IC	$\leq 10^{-11}$
IVR	$10^{-12} - 10^{-10}$
ISC	$10^{-11} - 10^{-6}$
Fluorescence	$10^{-9} - 10^{-6}$
Phosphorescence	$10^{-3} - 10^{1}$

1.3. Lasers and Dynamics

1.3.1. Pump-Probe Methodology

Understanding the process behind a chemical reaction is one of the most fundamental goals of chemistry. The study of reaction dynamics is focussed on movement of the various components of the reactants as they rearrange to form the products of the reaction. From an experimental perspective, the ability to study this is entirely dependent on the temporal resolution of the equipment. A useful analogy is that of the shutter in a camera. Taking a photo with too long an exposure, possibly caused by low light, causes the all-too-familiar blurry mess of movement through the frame. So it is with chemical dynamics. The shorter time period that the experiment interrogates, the more precise and useful the information gleaned. The other fundamental problem to be solved before very fast reactions can be observed is that of synchronising both the reaction and observation systems. Flash photolysis in the 1950s opened a new pathway to better resolution; by using a photon, the reaction can be started with considerably higher precision.[28] At the time, the shortest pulse of light easily available was a flash lamp. The reaction would be started with a flash of light and then some property would be measured at a defined delay. This is the driving principle of pump-probe spectroscopy.[29] The system is perturbed by an initial "pump" pulse to a new excited state and then interrogated at some time later by the "probe" pulse. With considerable repetition, this allows for a time-based map of the reaction to be constructed.

The next breakthrough was to reduce the length of the light pulses. This was achieved with the invention of the laser.[19] Subsequent developments have seen all technical aspects of lasers improve, unsurprisingly; be it more power, shorter pulses or more wavelengths becoming available.

1.3.2. Spontaneous and Stimulated Emission

While the properties of light are well understood, mostly due to the inspired work of Maxwell, there are a few particular properties of femtosecond laser pulses that are worth describing and considering.[30]

A laser relies on a situation of population inversion and is driven by a radiative emission process. The crucial difference between the fluorescence described earlier and laser action is that the laser action makes use of an incoming photon to drive the process. The relative rates of excited state decay between the spontaneous and stimulated emission are described by the Einstein *A* and *B* coefficients.[2,19] Consider a simple 2 level system as in Figure 1.8.

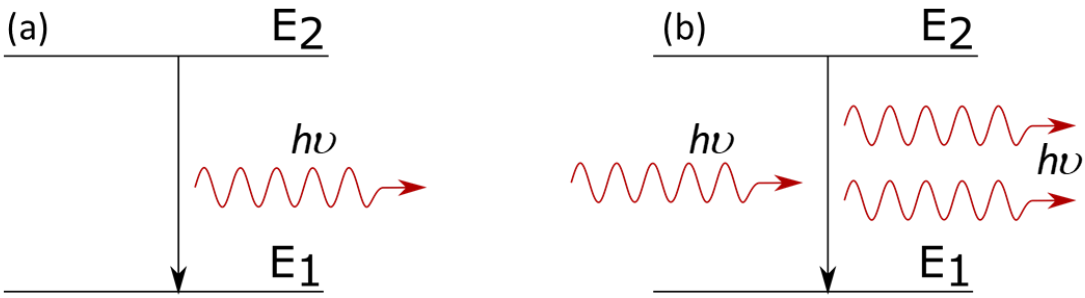

Figure 1.8 Schematic representation of a two-level system for a) spontaneous emission and b) stimulated emission.

Spontaneous emission can be easily considered as only dependent on the number of particles in the upper state. The rate of population loss from the upper state is thus defined by:

$$\left(\frac{dN_{E_2}}{dt}\right) = -A_{21}N_{E_2}\ , \tag{1.31}$$

where N_{E_2} is the number density of particles in the upper energy state, E_2, and A_{21} as the Einstein A coefficient that describes the probability of spontaneous decay from the upper to the lower state.[19] The resultant photon has energy $E_2 - E_1 = h\nu_{21}$ but a range of broadening effects cause this transition to actually emit over a range

of frequencies known as the linewidth.[19] An isolated atom would still have a linewidth due to the uncertainty principle in energy and time:

$$\Delta E \Delta t > \frac{\hbar}{2} \ , \tag{1.32}$$

where Δ is the uncertainty in the subsequent variable. This demonstrates that a slow decay, one associated with a large uncertainty as to the lifetime of the excited state, will have the narrowest linewidth.

Stimulated emission is similar but now the probability is modified by the incoming photons. Representing the photons with a spectral energy density, $\rho(\nu)$, defining the number of photons and their energy, the rate of stimulated emission is:

$$\left(\frac{dN_{E_2}}{dt} \right) = -B_{21} N_{E_2} \rho(\nu_{21}) \ , \tag{1.33}$$

where B_{21} is the Einstein B coefficient describing the probability for the transition from state 2 to 1 under an isotropic radiation field.[19] This same coefficient describes absorption as these processes are analogous, though the rate of absorption is dependent on the ground state population, rather than that of the excited state. This subtle difference in population dependence demonstrates the population inversion required for light amplification, so that the stimulated emission occurs more often than the absorption of the relevant photons.

The *A* and *B* coefficients are mathematically linked by:

$$A_{21} = \frac{8\pi h \upsilon_{21}^3}{c^3} B_{21} \ , \tag{1.34}$$

where c is the speed of light.[19] This expression demonstrates the relative likelihood of spontaneous emission as a function of increasing gap between energy levels. This increase explains one of the major difficulties of high energy lasers – the larger the *A* coefficient, the higher likelihood of a spontaneous emission and a decoherent beam.

A population inversion is impossible to obtain with a two-level system. Any process that would promote population from one state to the other, would also induce decay and result in a maximum of equal populations.[19] The simplest feasible solution is a three-level system, as shown in Figure 1.9 (a). This operates by absorption of the pump energy, then quick decay to another excited state. This can produce a population inversion, but only under pulsed conditions. This is due to the use of the ground state as the lower level, which is where most population will reside. This challenge is overcome with a four-level scheme, shown in Figure 1.9 (b). The relies on a fast decay from both E_4 and E_2, resulting in a pronounced inversion between E_3 and E_2.[19] This arrangement is considerably more energetically efficient than that of the three-level system and can also run continuously.

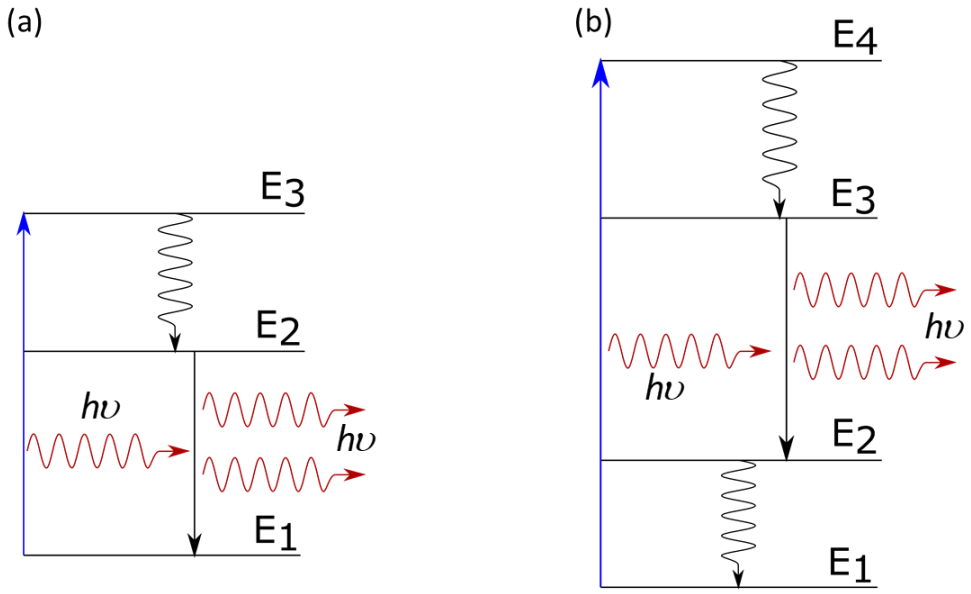

Figure 1.9 Schematic representation of a (a) three-level laser and (b) four-level laser.

1.3.3. Mode Locking

A typical laser contains 2 major elements: a gain medium capable of frequent or continuous population inversion and an optical cavity.[19] How these relate defines the laser's output. A given medium will have a frequency range over which light

amplification is possible. For example, a simple He-Ne laser has a gain bandwidth of ~1.5 GHz, while the Ti:sapphire laser common in femtosecond laser labs has a bandwidth of nearly 130 THz.[31,32] A further restriction on the possible output frequencies is enforced by the cavity of the laser. There are some types of laser that operate without a reflecting cavity, such as X-ray free electron lasers, but they will not be discussed here.[33] The resonant cavity causes constructive and destructive interference to form standing waves in the structure and as such only some frequencies are stable within. Putting these two constraints together shows the output of a laser to consist of a succession of fixed frequencies allowed by the cavity within the gain envelope of the medium.

While there are only fixed frequencies stable within the cavity, the relative phase between these is not defined by default. When the relative phase between different modes is fixed, different behaviour is seen. If there are but a couple of modes, due to a narrow gain bandwidth or a particular cavity design, the amplitude of a continuous laser would rise and fall as these different frequencies interacted in time. However, as more modes are linked the output tends toward an intense pulsed output.[19] This can be seen as a sum of waves and is illustrated in Figure 1.10.

Figure 1.10 only shows the contribution of relatively few modes, a Ti:sapphire laser can easily have 10^5 or more modes contributing. The more modes that contribute to the pulse, the shorter it becomes. This corresponds with eq.(1.32) as the shorter in duration the pulse becomes the broader the energy distribution within it.

How a laser system achieves the mode-locking phenomenon can be considered as either an active or a passive process. Both rely on some process to cause the mode-locked state to be more favourable than not. While there are various methodologies, the relevant one for the laser systems of this lab is Kerr-lens mode-locking.[34] The Kerr effect is the change in the refractive index of a material in response to an applied electric field. In the case of the optical elements in the laser path, the applied electric field is that of the light itself. This causes different intensities of light to experience different refractive indices, allowing the use of an aperture to prefer a mode-locked pulsed operation to a continuous wave.

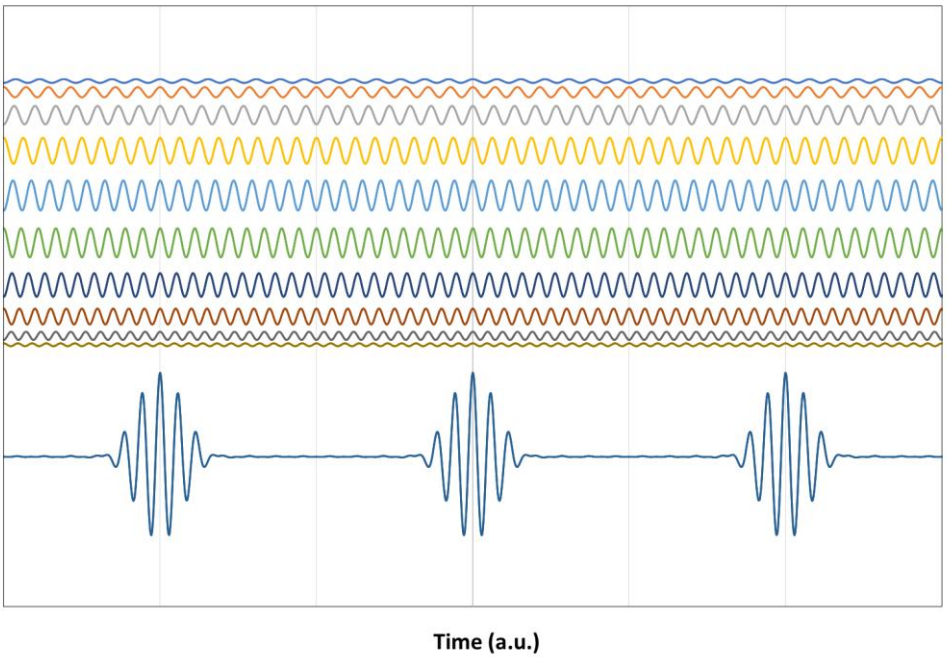

Figure 1.10 Summation of coherent cosine waves demonstrating the formation of a train of short intense peaks. The summation (shown lower) is of 10 consecutive individual modes (shown upper in descending order). Gridlines highlight points of maxima and minima.

1.3.4. Franck-Condon Principle and Transition Moments

When discussing internal conversion in section 1.2.2, mention was made of the Franck-Condon factor. The factor comes from a numerical approach to the Franck-Condon principle. This can be seen as an extension of the Born-Oppenheimer (B-O) approximation discussed earlier in section 1.1.1. As previously stated, the electronic transition takes place considerably faster than any nuclear motion. Thus, it takes place relative to static nuclear geometry. This corresponds to a vertical transition on a potential energy diagram, such as Figure 1.11. Once it has taken place the nuclei resume their previous motion and react to the new electron cloud. [19,35–37]

Considering a more mathematical treatment of the interaction of a molecule with a photon requires the use of dipole moments. The electric dipole moment, $\vec{\mu}$, is the summation of all products of the charge and the positions.[19] This distribution of charge then interacts with the electric field of the photon, $\vec{\varepsilon}$.

The energy of this interaction is:

$$E = \vec{\mu} \cdot \vec{\varepsilon} \ , \tag{1.35}$$

with $\cdot$ being the scalar product. When considering the majority of electronic transitions, and indeed all the work from this lab, the wavelength of the light is vastly larger than the molecule being irradiated. When considering a larger molecule in section 1.1.2, we made use of the chromophore of the Green Fluorescent Protein (GFP), for comparison, the entire protein is around 50-60 Å.[38] This means that the electric field of the incident photon is effectively constant over the 5-6 nm of the molecule. A photon with a wavelength of 12 nm, twice that of the molecule, would have an energy in excess of 100 eV.

The strength of the interaction that governs the transition between the states is known as the transition dipole moment.[19] Considering a transition between an initial state ψ_{i} to a final state ψ_{f} ,this is given as:

$$\vec{\mu}_{\mathrm{T}} = \left\langle \psi_{\mathrm{f}}^{*} \middle| \hat{\mu} \middle| \psi_{\mathrm{i}} \right\rangle \ , \tag{1.36}$$

where the previous vector quantity of the electric dipole has been replaced by the electric dipole moment operator:

$$\hat{\mu} = \sum_{j} q_j \vec{\boldsymbol{r}}_j \tag{1.37}$$

with q_i and $\vec{\boldsymbol{r}}_i$ being the charge and position vector of the *j*-th particle.[19] As it is written in eq. (1.36), the initial and final states are defined in both electronic and nuclear coordinates. Using the B-O approximation to allow for the separation of the variables, the transition in purely electronic coordinates for a fixed nuclear geometry becomes a constant. The transition dipole moment can then be expressed as a constant and a vibrational overlap integral.

$$\vec{\mu}_{\mathrm{T}} = \vec{\mu}_{\mathrm{e}} \int \psi_{\mathrm{f,vib}}^{*} \psi_{\mathrm{i,vib}} \mathrm{d}r \ , \tag{1.38}$$

where:

$$\bar{\mu}_{e} = \int \psi^{*}_{f,elec} \hat{\mu} \psi_{i,elec} \, d\tau_{e} \ . \tag{1.39}$$

Within this framework, τ_e and r are the electron coordinates and nuclear coordinates respectively, and the further subscript on the wavefunctions defines the vibrational or electronic component. The electronic transition dipole moment is often treated as a constant, but it depends parametrically on the nuclear geometry. Typically, the electronic transition dipole moment does not change radically with geometry, unless near curve crossings where the B-O approximation breaks down The absolute square of the vibrational wavefunction overlap integral in eq.(1.38) is proportional to the transition probability and this is the quantity that is known as the Franck-Condon factor.[19] This can be seen visually in Figure 1.11, where the wavefunction overlap is best aligned with the fifth excited vibrational level. Thus, the intensity of this transition would be the strongest. However, when dealing with the short pulses and thus large bandwidth of femtosecond laser excitation, many final vibrational states are populated, a phenomenon that will be covered in section 1.3.5.

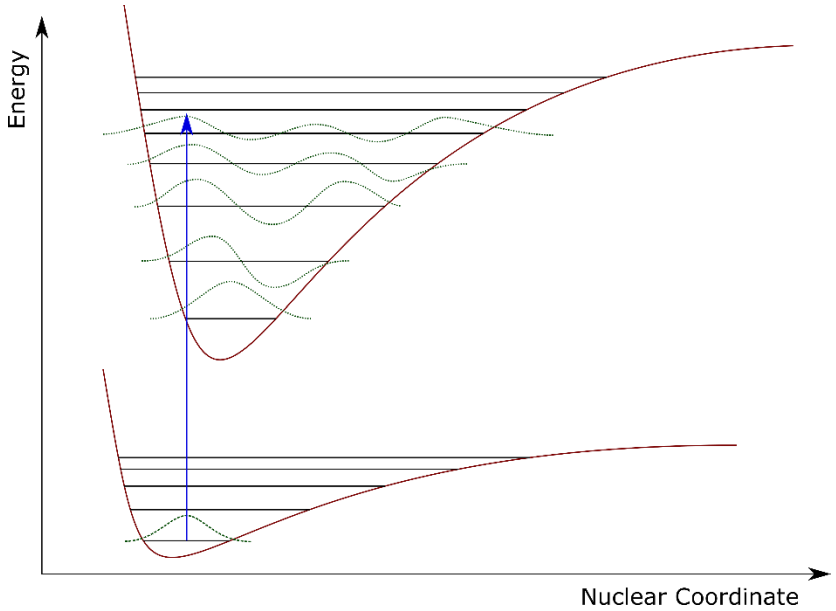

Figure 1.11 Transitions from a lower to a higher electronic state are most often dominated by the vertical transition, the transition with the largest Franck-Condon factor with no nuclear movement. In the above, this would be to the 5th excited vibrational level shown here.

The Franck-Condon factor is also related the Einstein B coefficient covered in section 1.3.2.[19] This is to be expected as absorption and stimulated emission are related processes. Thus, in keeping with eq.(1.33), but now for an absorption process: [19]

$$\left(\frac{dN_{E_2}}{dt}\right) = B_{21}N_{E_1}\rho(\nu_{21}) = \frac{|\mu_T|^2}{6\varepsilon_0\hbar^2}N_{E_1}\rho(\nu_{21}) \tag{1.40}$$

1.3.5. Wavepackets

In ultrafast excitation processes the large energy bandwidth involved causes the formation of a coherent superposition of a variety of excited vibrational states, forming a so-called wavepacket. [2]

The motion of a wavepacket often seems similar to that of a classical particle due to their localisation in space and time. A visualisation of this is given in Figure 1.10, which shows a linear superposition of coherent oscillations. This wavepacket is only the solution at the instant of excitation, the system will then evolve with time. Mathematically, this is represented as the sum of waves with a time dependent phase factor.

$$|\Psi(t)\rangle = \sum_a c_a(t_0)e^{-\frac{iE_a(t-t_0)}{\hbar}}|\psi_a\rangle \ , \tag{1.41}$$

with $c_a(t_0)$ being the initial state condition, i being the imaginary number and E_a being the respective energy of eigenstate ψ_a.[17] In a perfectly harmonic potential such as the one shown in Figure 1.6, this wavepacket will oscillate between the edges of the potential indefinitely. However, in reality the packet will dephase.

When dealing with a large system with many states in close proximity it is often preferable to replace the discrete summation of eq. (1.41) with an integral and the initial shape of the wavepacket given by a shape function, $g(k)$:

$$\Psi(x,t) = \int g(k)\psi_k(x,t)\mathrm{d}k \tag{1.42}$$

The shape function for a Gaussian wavepacket is defined by a general parameter, *k*, with a central value, k_0 and a width factor, Γ , with a normalisation factor, *N*.

$$g(k) = Ne^{-\frac{(k-k_0)^2}{2\Gamma^{-2}}} \tag{1.43}$$

1.4. Photoelectron Spectroscopy

Photoelectron spectroscopy (PES) has become a very versatile and important tool for the study of electronic states and dynamics. The fundamental principles behind it are conservation of energy and the photoelectric effect, the latter of which gained Einstein his Nobel prize.[39]

By considering light as photons, each with energy $h\upsilon$, means that electrons ejected after a photoelectric event contain information about the system they were ejected from. By measuring the kinetic energy of these escaped electrons and knowing the wavelength of the light used, allows for evaluating the binding energy of the original system.

$$h\upsilon = eBE + eKE\,. \tag{1.44}$$

PES will work on any range of anionic, neutral and cationic species. The major difference is the quantity of energy required to remove the electron.[19] This means that anionic and neutral PES experiments are relatively abundant, cationic variations are rarer.[40] For familiarity, this discussion will assume starting from an anion resulting in a neutral molecule and a photoelectron. This has been the process behind the work presented here. The process is described in Figure 1.12.

A further aid to PES experimental data is that the selection rules for the process are extremely relaxed, especially relative to other optical detection techniques such as laser induced fluorescence (LIF). The intensity of the transitions in the PES spectra, as indicated below in Figure 1.12, depends on the Franck-Condon factors discussed

previously and the photodetachment cross section of the parent molecule.[19] The latter is a measure of the initial system's likelihood of absorbing the photon, thus if this is low, very few photoelectrons result. However, this would not change the relative intensities of the vibrational level transitions.

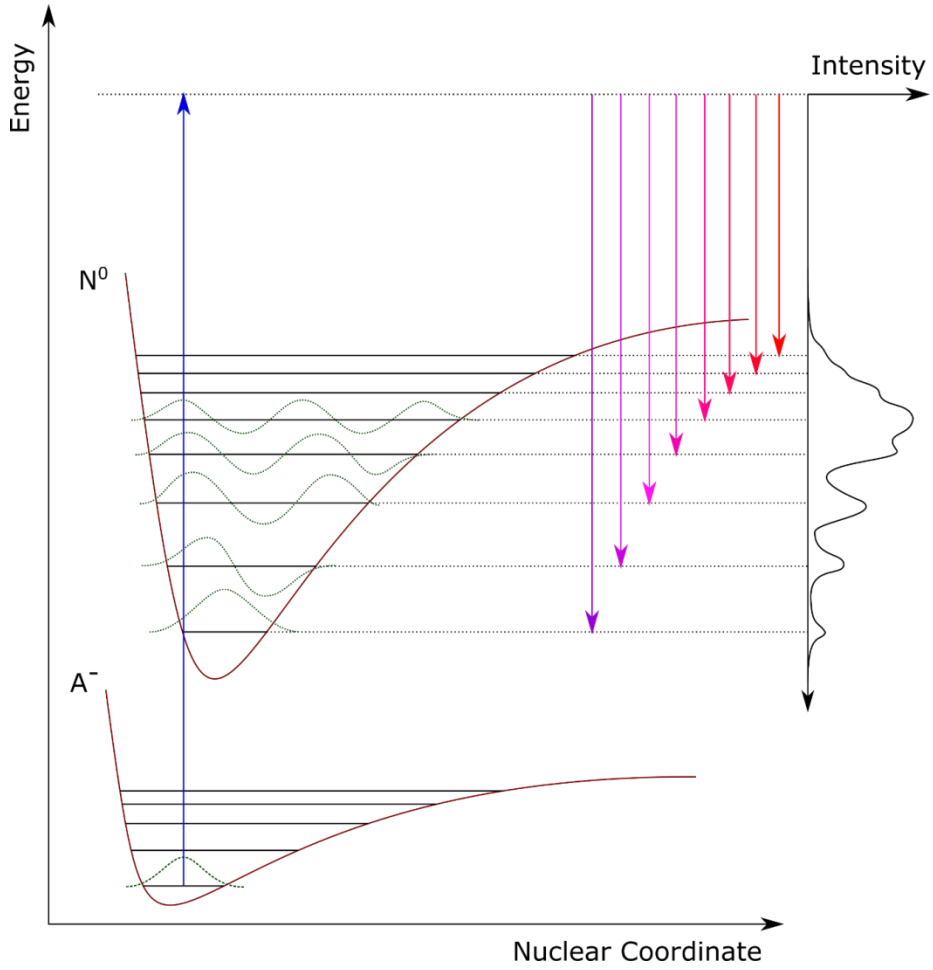

Figure 1.12 Schematic representation of photoelectron spectroscopy (PES). Starting from the ground state of the anion, A^-, the input of a photon promotes the system to a virtual state above the neutral ground state, N^0. Upon falling back to a lower energy state, in this case vibrational levels of the ground state, the intensity of the emitted photoelectrons is defined by the Franck Condon factor described in section 1.3.4 and in Figure 1.11.

The photodetachment cross section is known to have an energy dependence once above the energy threshold for the transition. This is known as the Wigner threshold law.[41–43] Once above threshold, the cross section increases, but at different rates depending on the orbital angular momentum of the outgoing electron, ℓ .

The cross section, σ, behaves as:

$$\sigma \propto (\Delta E)^{\ell+\frac{1}{2}}, \tag{1.45}$$

where ΔE is the energy above the threshold value (the electron kinetic energy). Considering outgoing electrons of *s*, *p* or *d* character reveals that higher angular momentum results in an eventually faster growing cross section. The lowest kinetic energy electrons are preferentially of *s* character but all electrons have zero cross section at zero kinetic energy. This implies that any photoelectrons detected as having zero eKE has come from an indirect detachment process, such as thermionic emission.

Thermionic emission is a statistical process that takes place from a highly vibrationally excited level of the ground electronic state. This often is produced by an approach from higher lying electronic states which then internally convert[‡]. The highly excited vibrational level eventually "boils" off an electron.

As the selection rules for PES are relaxed, other considerations are required to predict the final states of a PES experiment. One of these is Koopmans' correlations.[44,45] The theory is that there is no other rearrangement of electrons after electron loss. This is illustrated in Figure 1.133. A transition from the excited anionic state, S_1, to the ground state of the neutral molecule, D_0, would only involve the loss of the single most energetic electron.

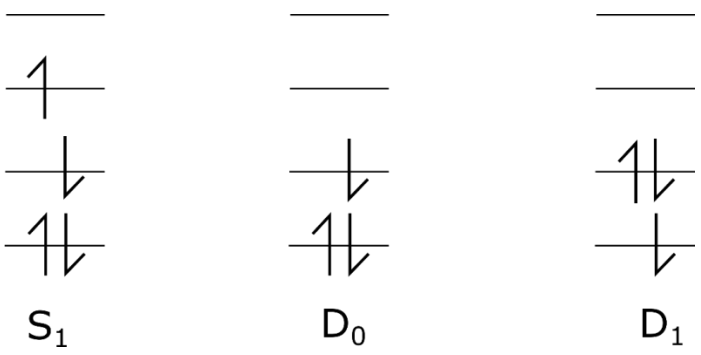

Figure 1.13 Illustrating Koopmans' correlations along with shape and Feshbach resonances. For the purposes of understanding, S_1 would be the first excited state of the anion, with D_0 and D_1 being the ground state and first excited state of the corresponding neutral molecule respectively.

[‡]See Section 1.2.2

There is no other electron movement between those two states. These states are thus described as Koopmans correlated.

Contrastingly, a transition to the first neutral excited state, D_1, would require the loss of the same electron as before and then a promotion of one of the lower lying electrons. These would not be Koopmans correlated. However, two-electron processes can and do occur.

The loss of the electron from the S_1 state shown in Figure 1.13 can occur by photon absorption or spontaneously (autodetachment) if the S_1 state lies above the D_0 state energetically. In the latter case, the S_1 state is embedded in the continuum and therefore is a resonance. There are two types of resonances: shape and Feshbach. [46] A single electron movement comprises a shape resonance ($S_1 \rightarrow D_0 + e^-$) while a two-electron movement corresponds with a Feshbach resonance ($S_1 \rightarrow D_1 + e^-$). Shape resonances typically undergo faster autodetachment than Feshbach resonances.[46,47]

1.4.1. Time Resolved Photoelectron Spectroscopy

A time-resolved PES (TRPES) experiment makes use of several of the concepts presented earlier. An initial pump[§] laser pulse promotes the system into an excited state. This generates a wavepacket that then propagates according to the dynamics of the system. The wavepacket is interrogated by the application of a probe pulse that then photodetaches the molecule at some delay. The kinetic energy of the resultant electron presents information as to the relative energy of the system as it evolves in time. This is shown schematically in Figure 1.14.

While the schematic form of the experiment presented in Figure 1.14 shows clearly defined temporally-resolved data, often the reality of doing the experiment makes this an oversimplification.

One of the major challenges is that the temporal signal is often obscured due to it being inherently a sequential two photon process.[48] Thus, the molecule has to "be

[§] See section 1.3.1.

lucky" twice, once to interact with the laser the first time and then again for the second pulse. This means that the actual raw signal from such an experiment can often be dominated by single-colour events. The simplest way to fix this is to perform a background subtraction. The choice of background to subtract is often decided by the controls of the experiment. For this lab, negative time delays are often used.

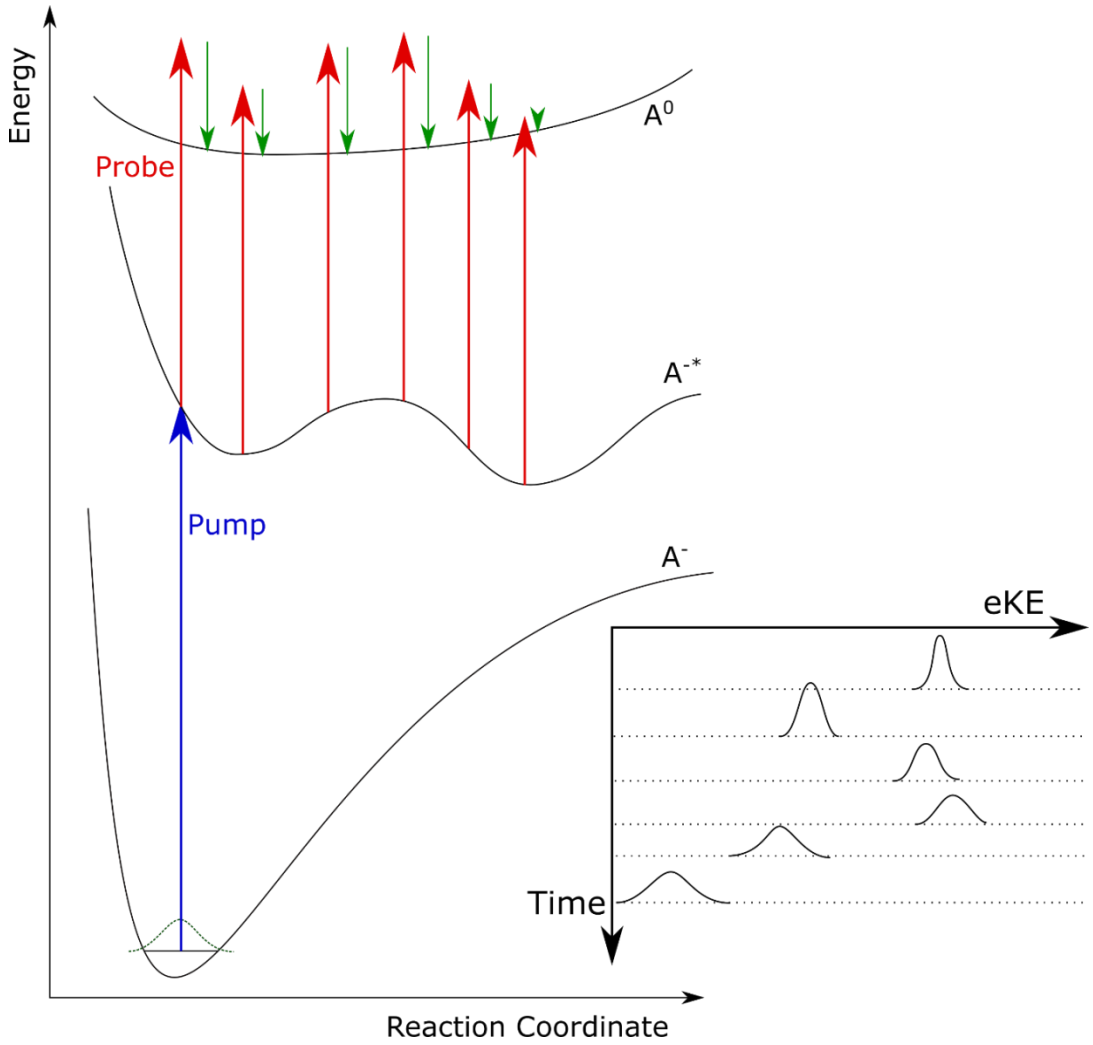

Figure 1.14 Schematic of time-resolved photoelectron spectroscopy (TRPES). An anionic ground state, A^-, is initially excited by a pump pulse (blue) to an excited anionic state, A^{-*}. Subsequently a probe pulse (red) photodetaches the electron, returning the molecule to the neutral ground state, A^0, and ejecting the electron with some kinetic energy (green). It is possible to introduce a delay between pump and probe pulse such that the excited state wavepacket is probed as it moves across the A^{-*} surface. Interrogating this at different times produces photoelectrons with different kinetic energies depending on how they map between states, a pictorial representation of which is shown inset lower right.

Negative time delays occur when the probe pulse arrives before the pump. This choice of background is especially simple to acquire, however does rely on the assumption that there are no dynamics for a sequential two-photon process in that configuration. Data can still be analysed if this is true, that a probe pulse can access a state that the pump then subsequently ionises, but the analysis is more challenging.

When discussing the temporal position as being either positive or negative, the physical control over which beam is delayed is irrelevant, it is the difference that is important. Similarly, it is the breadth of the pulses that defines the temporal resolution more than the control over the relative delay.

Interpreting the data from a TR experiment can often include features that change in intensity and energy, often indicating the stretching of bonds causing different FC factors, or the movement of population as one feature decays as another rises.

1.4.2. Frequency- and Angle-Resolved Photoelectron Imaging

In frequency-resolved photoelectron spectroscopy (FR-PES), one acquires photoelectron spectra at a wide range of photon energy. FR-PES imparts more information than single frequency PES as different excited-state dynamics and processes have different energy dependencies. The 2D map of photoelectron signal as a function of both electron kinetic energy and photon energy clearly shows the locations of various energy levels, whether they are neutral or anionic states. Relative to the schematic representation in Figure 1.122, FR-PES corresponds to varying the length of the arrow representing the incident photon.

The complementary technique is to look at the photoelectron angular distribution (PAD).[49] This is the spatial arrangement that the electrons make as they leave the anion in question. When considering a generalised system, the PAD is defined by symmetry and is the sum of spherical harmonic functions.[49] Because of the summation of photoelectron partial waves of different character, interference

patterns can emerge and cause specific directions to be favoured. The most general form for the PAD is given by:

$$I(\theta,\varphi) \propto \sum_{L=0}^{L_{\max}} \sum_{M=-L}^{L} B_{LM} Y_{LM}(\theta,\varphi), \tag{1.46}$$

where Y_{LM} are spherical harmonic functions and B_{LM} are the expansion parameters. M is the order of the spherical harmonic and L is the rank of the spherical harmonic. $L_{\max}$ is usually twice the number of photons that interact with the system, thus this corresponds to a value of 2 for a single photon experiment and 4 for a standard 1-pump, 1-probe time resolved measurement.[50] The use of linearly polarised light applies a cylindrical symmetry and restricts terms to $M = 0$. For simplicity, the spherical harmonics are often replaced with Legendre polynomials in $\cos(\theta)$, thus:[50,51]

$$I(\theta) \propto \sum_{L=0}^{L_{\max}} \beta_L P_L(\cos(\theta)) , \tag{1.47}$$

where P_L is the L-th order Legendre polynomial and β_L are anisotropy parameters. Odd terms, 3 5, 7 or higher would only occur if the molecules have been oriented and the electrons could only leave in one direction. The β_2 parameter, corresponding to a single photon photoelectron, is often used to characterise the anisotropy of a given photodetachment. The parameter ranges in value from –1 to +2 and defines the angular anisotropy relative to the axis of the laser polarisation.

When taken together with the frequency-resolved data, various trends become more visible. Previous work from this lab on para-benzoquinone will serve as an example.[52] A combination of frequency and angularly resolved data is presented in Figure 1.15. Upon excitation at 2.48 eV, the main photoelectron feature is a peak at ~ 0.4 eV that corresponds to a direct detachment. At 4.13 eV excitation, the major photoelectron feature is a peak at ~ 2 eV that would be energetically consistent with direct detachment as well. However, it is clear upon looking at the total frequency-resolved spectra that some other process can be seen between these two photon energies.

The proximity and parallel nature of the highest eKE feature to the line of maximum energy indicates that this is indeed the direct detachment process peak. This feature also highlights the difference between the adiabatic electron affinity and the vertical detachment energy. The adiabatic energy is the difference in energy between the vibrational ground states of the anion and the neutral molecule. The vertical detachment energy is that of the most intense transition as predicted by the Frank-Condon principle. This is seen here in the data as the horizontal breadth of the direct detachment feature. A small feature can be seen appearing at $h\upsilon \geq 4.2$ eV. This corresponds with the opening of channels to neutral excited states. The diagonal leading edge would be expected to continue for higher photon energies as this is another direct detachment process.

Photoelectron signal very close to zero kinetic energy is usually assigned to thermionic emission as mentioned in section 1.4. This involves loss from a vibrationally hot anion ground state. The similar process of autodetachment would be from an excited state anion resonance to form a vibrationally hot neutral. Crucially, this process would be subject to the Wigner threshold law and thus the considerable intensity cannot be from an autodetachment process.

The most complex region in Figure 1.15 is from 2.5 to 3.3 eV in photon energy. The reduction in intensity of the direct detachment peak and the increase in low kinetic energy electrons is often indicative of the onset of anionic excited-state resonances. Further evidence of this sudden change is given by the sharp change in the angular distribution as the photon energy increases past ~ 2.75 eV. Here, the excited state can clearly recover to the ground anionic state as seen by the continued thermionic emission peak at near zero kinetic energy. Computational work allowed for more understanding of this state and predicted a shape resonance between this and the ground neutral state. This autodetachment process is responsible for the broad feature at $\text{eKE} \sim 0.4$ eV.

This understanding is then used to construct the time-resolved experiment to consider the rate of the dynamics caused by the competing processes.

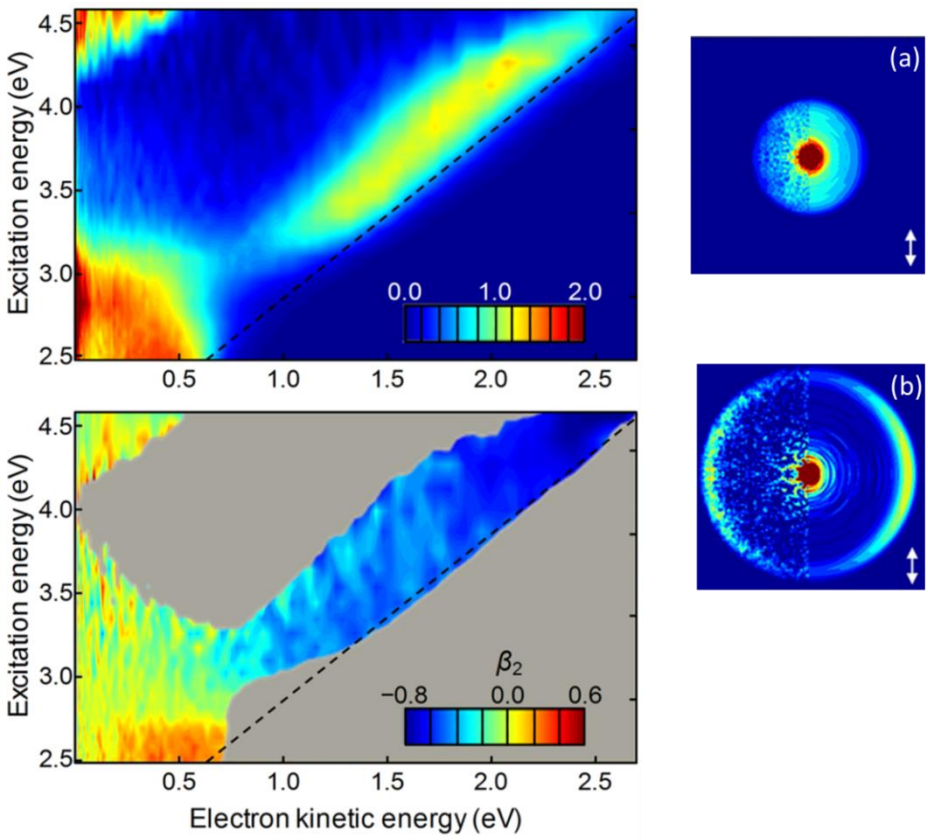

Figure 1.15 (Left, upper) False colour representation of the frequency-resolved photoelectron spectra of *para*-benzoquinone normalised to the total integrated signal in each spectrum. (Left, lower) β_2 anisotropy parameter for the same features shown above, while shaded areas indicate areas of low normalised photoelectron signal (<0.375), and as such high uncertainty in the angular distribution. The diagonal dashed line shows the maximum single-photon photoelectron kinetic energy based on an adiabatic electron affinity of 1.86 eV. (a) The central slice through the photoelectron image at 2.48 eV. The left-hand-side is experimental data retained in the algorithm, the right is the fitted polynomials. (b) As (a) but for a photon energy of 4.13 eV. Adapted with permission from Ref. 52. Copyright (2014) American Chemical Society.

1.5. References

1 D. A. McQuarrie, *Statistical Mechanics*, University Science Books, Sausalito, Calif, 2000 edition., 2000.
2 P. Atkins and J. de Paula, *Atkins' Physical Chemistry*, OUP Oxford, 8th edn., 2006.
3 T. Guenault, *Statistical Physics (Student Physics Series): Enlarged Edition*, Springer, Dordrecht, Revised edition., 2007.
4 W. C. Martin, *J. Phys. Chem. Ref. Data*, 1973, **2**, 257–266.
5 E. J. Baran, *Z. Für Naturforschung A*, 2014, **58**, 36–38.
6 C. W. West, J. N. Bull, A. S. Hudson, S. L. Cobb and J. R. R. Verlet, *J. Phys. Chem. B*, 2015, **119**, 3982–3987.
7 D. A. Horke and J. R. R. Verlet, *Phys. Chem. Chem. Phys.*, 2012, **14**, 8511–8515.
8 D. A. Horke, A. S. Chatterley and J. R. R. Verlet, *J. Phys. Chem. Lett.*, 2012, **3**, 834–838.
9 M. C. DeRosa and R. J. Crutchley, *Coord. Chem. Rev.*, 2002, **233**, 351–371.
10 S. J. Arnold, M. Kubi and E. A. Ogryzlo in *Oxidation of Organic Compounds*, American Chemical Society, 1968, vol. 77, pp. 133–142.
11 A. Jabłoński, *Nature*, 1933, **131**, 839–840.
12 K. L. Reid, *Int. Rev. Phys. Chem.*, 2008, **27**, 607–628.
13 J. E. Jones, *Proc. R. Soc. Lond. Math. Phys. Eng. Sci.*, 1924, **106**, 463–477.
14 L. Verlet, *Phys. Rev.*, 1967, **159**, 98–103.
15 Q. Hao, X. Deng, J. Long, Y. Wang, B. Abulimiti and B. Zhang, *Spectrochim. Acta. A. Mol. Biomol. Spectrosc.*, 2017, **183**, 109–115.
16 J. T. Yardley, *Introduction to Molecular Energy Transfer*, Academic Press, 2012.
17 P. W. Atkins and R. S. Friedman, *Molecular Quantum Mechanics*, OUP, New York, 4th edition., 2004.
18 P. A. M. Dirac, *Proc. R. Soc. Lond. Math. Phys. Eng. Sci.*, 1927, **114**, 243–265.
19 J. M. Hollas, *Modern Spectroscopy*, Wiley, 4th edition, 2004.
20 R. Englman and J. Jortner, *Mol. Phys.*, 1970, **18**, 145–164.
21 I. V. Hertel and W. Radloff, *Rep. Prog. Phys.*, 2006, **69**, 1897.
22 N. H. Damrauer, G. Cerullo, A. Yeh, T. R. Boussie, C. V. Shank and J. K. McCusker, *Science*, 1997, **275**, 54–57.
23 S. Tobita, M. Arakawa and I. Tanaka, *J. Phys. Chem.*, 1985, **89**, 5649–5654.
24 M. A. Robb, M. Garavelli, M. Olivucci and F. Bernardi, in *Reviews in Computational Chemistry, Volume 15*, John Wiley & Sons, Inc., 2007, pp. 87–146.
25 F. Bernardi, M. Olivucci and M. A. Robb, *Chem. Soc. Rev.*, 1996, **25**, 321–328.
26 D. A. Farrow, W. Qian, E. R. Smith, A. A. Ferro and D. M. Jonas, *J. Chem. Phys.*, 2008, **128**, 144510.
27 M. J. Paterson, M. J. Bearpark, M. A. Robb, L. Blancafort and G. A. Worth, *Phys. Chem. Chem. Phys.*, 2005, **7**, 2100–2115.
28 M. Eigen, *Discuss. Faraday Soc.*, 1954, **17**, 194–205.
29 D. M. Neumark, *Annu. Rev. Phys. Chem.*, 2001, **52**, 255–277.
30 J. C. Maxwell, *A treatise on electricity and magnetism, by James Clerk Maxwell*, Oxford, Clarendon Press, 1873.
31 P. F. Moulton, *JOSA B*, 1986, **3**, 125–133.

32 T. M. Niebauer, J. E. Faller, H. M. Godwin, J. L. Hall and R. L. Barger, *Appl. Opt.*, 1988, **27**, 1285–1289.

33 R. Abela, A. Aghababyan, M. Altarelli, C. Altucci, G. Amatuni, P. Anfinrud, P. Audebert, V. Ayvazyan, N. Baboi, J. Baehr, V. Balandin, R. Bandelmann, J. Becker, B. Beutner, C. Blome, I. Bohnet, A. Bolzmann, C. Bostedt, Y. Bozhko, A. Brandt, S. Bratos, C. Bressler, O. Brovko, H. Brück, J.-P. Carneiro, S. Casalbuoni, M. Castellano, P. Castro, L. Catani, A. Cavalleri, S. Celik, H. Chapman, D. Charalambidis, J. Chen, M. Chergui, S. Choroba, A. Cianchi, M. Clausen, E. Collet, H. Danared, C. David, W. Decking, M. Dehler, H. Delsim-Hashemi, G. Dipirro, B. Dobson, M. Dohlus, S. Duesterer, A. Eckhardt, H.-J. Eckoldt, H. Edwards, B. Faatz, M. Fajardo, A. Fateev, J. Feldhaus, Y. Filipov, K. Floettmann, R. Follath, B. Fominykh, M. French, J. Frisch, L. Froehlich, E. Gadwinkel, L. García-Tabarés, J. J. Gareta, T. Garvey, F. Gel'mukhanov, U. Gensch, C. Gerth, M. Goerler, N. Golubeva, H. Graafsma, W. Graeff, O. Grimm, B. Griogoryan, G. Grübel, C. Gutt, K. Hacker, L. Haenisch, U. Hahn, J. Hajdu, J. H. Han, M. Hartrott, J. Havlicek, O. Hensler, K. Honkavaara, V. Honkimäki, T. Hott, M. R. Howells, M. Huening, H. Ihee, F. Ö. Ilday, R. Ischebeck, M. Jablonka, E. Jaeschke, K. Jensch, J.-P. Jensen, S. Johnson, L. Juha, F. Kaerntner, R. Kammering, H. Kapitza, V. Katalev, B. Keil, S. Khodyachykh, R. Kienberger, J.-W. Kim, Y. Kim, K. Klose, V. Kocharyan, W. Koehler, M. Koerfer, M. Kollewe, Q. Kong, W. Kook, D. Kostin, O. Kozlov, D. Kraemer, M. Krasilnikov, B. Krause, O. Krebs, J. Krzywinski, G. Kube, M. Kuhlmann, H. Laich, R. Lange, M. Larsson, R. W. Lee, A. Leuschner, H. Lierl, L. Lilje, T. Limberg, A. Lindenberg, D. Lipka, F. Loehl, K. Ludwig, M. Luong, C. Magne, A. Maquet, J. Marangos, C. Masciovecchio, M. Maslov, A. Matheisen, E. Matyushevskiy, O. Matzen, H.-J. May, I. McNulty, D. McCormick, P. Meulen, N. Meyners, P. Michelato, N. Mildner, V. Miltchev, M. Minty, W.-D. Moeller, T. Möller, L. Monaco, M. Nagl, O. Napoly, G. Neubauer, P. Nicolosi, A. Nienhaus, D. Noelle, T. Nunez, F. Obier, A. Oppelt, C. Pagani, R. Paparella, H. B. Pedersen, B. Petersen, B. Petrosyan, L. Petrosyan, A. Petrov, P. Piot, J. Pflueger, A. Plech, E. Ploenjes, L. Poletto, G. Pöplau, E. Prat, S. Prat, J. Prenting, D. Proch, D. Pugachov, H. Quack, B. Racky, D. Ramert, H. Redlin, K. Rehlich, R. Reininger, H. Remde, D. Reschke, D. Richter, M. Richter, S. Riemann, D. Riley, I. Robinson, J. Roensch, F. Rosmej, M. Ross, J. Rossbach, V. Rybnikov, M. Sachwitz, E. Saldin, W. Sandner, J. Schäfer, T. Schilcher, H. Schlarb, M. Schloesser, V. Schlott, B. Schmidt, M. Schmitz, P. Schmueser, J. Schneider, E. Schneidmiller, F. Schotte, S. Schrader, S. Schreiber, C. Schroer, R. Schuch, H. Schulte-Schrepping, A. Schwarz, M. Seidel, J. Sekutowicz, P. Seller, D. Sellmann, F. Senf, D. Sertore, A. Shabunov, S. Simrock, W. Singer, H. Sinn, R. Smith, E. Sombrowski, A. A. Sorokin, E. Springate, M. Staack, L. Staykov, B. Steffen, B. Stephenson, F. Stephan, F. Stulle, E. Syresin, K. Sytchev, V. Sytchev, G. Tallents, S. Techert, N. Tesch, H. Thom, K. Tiedtke, M. Tischer, M. Tolan, S. Toleikis, F. Toral, R. Treusch, D. Trines, V. Tsakanov, I. Tsakov, T. Tschentscher, F.-R. Ullrich, U. van Rienen, A. Variola, I. Vartaniants, E. Vogel, J. Vogel, R. Vuilleumier, H. Wabnitz, R. Wanzenberg, J. S. Wark, H. Weddig, T. Weiland, H. Weise, M. Wendt, R. Wenndorff, R. Wichmann, I. Will, A. Winter, K. Witte, K. Wittenburg, P. Wochner, T. Wohlenberg, J. Wojtkiewicz, A. Wolf, M. Wulff, M. Yurkov, I. Zagorodnov, P. Zambolin, K. Zapfe, P. Zeitoun, V. Ziemann, A. Zolotov, R. Brinkmann and H.-J. Grabosch, *XFEL: The*

European X-Ray Free-Electron Laser - Technical Design Report, DESY, Hamburg, 2006.
34 G. Cerullo, S. D. Silvestri and V. Magni, *Opt. Lett.*, 1994, **19**, 1040–1042.
35 J. Franck and E. G. Dymond, *Trans. Faraday Soc.*, 1926, **21**, 536–542.
36 E. U. Condon, *Phys. Rev.*, 1926, **28**, 1182–1201.
37 E. U. Condon, *Phys. Rev.*, 1928, **32**, 858–872.
38 M. Ormö, A. B. Cubitt, K. Kallio, L. A. Gross, R. Y. Tsien and S. J. Remington, *Science*, 1996, **273**, 1392–1395.
39 A. Einstein, *Ann. Phys.*, 1905, **322**, 132–148.
40 D. M. Neumark, *Annu. Rev. Phys. Chem.*, 2001, **52**, 255–277.
41 A. Sanov and R. Mabbs, *Int. Rev. Phys. Chem.*, 2008, **27**, 53–85.
42 E. P. Wigner, *Phys. Rev.*, 1948, **73**, 1002–1009.
43 D. J. Pegg, *Rep. Prog. Phys.*, 2004, **67**, 857.
44 T. Koopmans, *Physica*, 1934, **1**, 104–113.
45 A. Stolow, *Annu. Rev. Phys. Chem.*, 2003, **54**, 89–119.
46 J. Schiedt and R. Weinkauf, *J. Chem. Phys.*, 1999, **110**, 304–314.
47 A. V. Bochenkova, B. Klærke, D. B. Rahbek, J. Rajput, Y. Toker and L. H. Andersen, *Angew. Chem. Int. Ed.*, 2014, **53**, 9797–9801.
48 J. N. Bull, C. W. West and J. R. R. Verlet, *Chem. Sci.*, 2015, **6**, 1578–1589.
49 K. L. Reid, *Annu. Rev. Phys. Chem.*, 2003, **54**, 397–424.
50 G. Wu, P. Hockett and A. Stolow, *Phys. Chem. Chem. Phys.*, 2011, **13**, 18447–18467.
51 R. N. Zare, *Mol. Photochem.*, 1972, **4**, 1.
52 C. W. West, J. N. Bull, E. Antonkov and J. R. R. Verlet, *J. Phys. Chem. A*, 2014, **118**, 11346–11354.

2. Build and Design

This chapter describes the design and build of a new ion trap and guide system for the existing photoelectron spectrometer. The various limitations of the previous setup are discussed before considering the design requirements for the replacement. The trap design is simulated and tested against a list of criteria, with changes made to improve performance relative to described metrics. The electronic design of the system is briefly discussed with reference to the effect on the ions as they pass through the design. This then leads to a discussion on the vacuum pressure considerations concluding with a review of the final design and proof-of-concept data.

2.1. The Previous Apparatus and Limitations

2.1.1. Pre-existing Spectrometer

The internal working of the existing spectrometer has been covered in significant detail elsewhere.[1–4] While this is in total a comprehensive description, it is worth compiling the relevant information here. The pre-existing setup can be presented schematically as seen in Figure 2.1. Moving from source to detection the process is as follows.

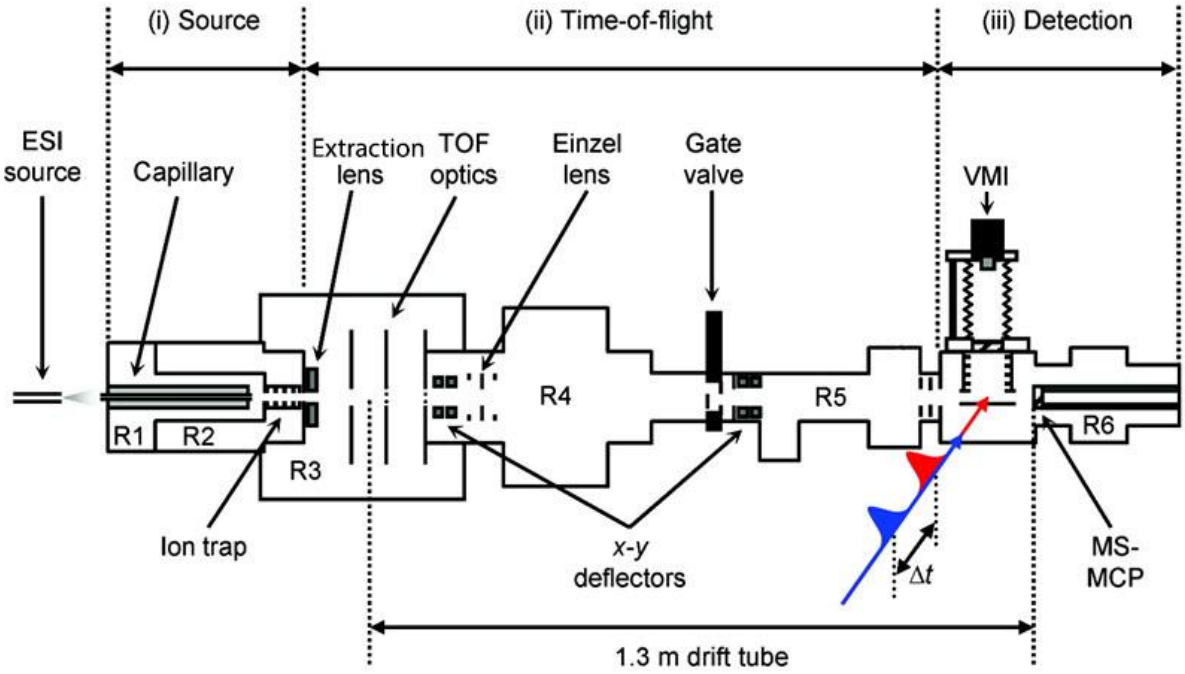

Figure 2.1 Schematic representation of the pre-existing spectrometer. Briefly, this comprises an electrospray ionisation source (ESI), a capillary to introduce the ions into the vacuum chamber, an ion trap extracting into a time-of-flight (TOF) mass spectrometer and a velocity map imaging(VMI) stack arranged about the point of interaction with laser beams. This will be discussed more thoroughly in the text. The sections labelled as R numerate the individual vacuum regions. Adapted with permission from Ref. 4. Copyright (2010) American Chemical Society.

Anions are initially produced by electrospray ionisation. This is a familiar technique in mass spectrometry for making ions in the gas phase. It is known particularly for its use in with large or otherwise fragile ions such as those of whole proteins or multiply charged ions.[5,6] In our particular experimental setup, the target molecule is dissolved in a suitable solvent. This is most often methanol, but has also been

water, acetonitrile, toluene, or any combination of the above. Sometimes a weak proton acceptor is added, such as ammonia in methanol, to facilitate the production of the molecular anion. A $\sim 1\ \mathrm{mM}$ solution of the species of interest is made up and expelled from a syringe using a commercial syringe pump (World Precision Instrument, Aladdin 1000) at a rate of $\sim 200\ \mu\mathrm{L/hr}$. The solution passes through a fine capillary needle with a large negative potential, $\sim -5\ \mathrm{kV}$. The value of this potential is varied to produce the best ion signal at the detector. Since the last description, the power supply for this needle has been replaced with a custom-housed HV supply (Applied Kilovolts, HP010NAA025). Having passed through this needle, the strong electric field at its tip causes the formation of a Taylor cone.[5] This generates a very fine mist of charge droplets with the same polarity as that applied to the needle. Once free of the bulk, solvent molecules start evaporating until the stabilising effect of the solvation is overcome by the repulsion between the similar charges present in the droplet. At this point the droplet undergoes a Coulombic explosion, whereupon the cycle of evaporation and explosion continues until bare ions or small clusters are left. It has been noted that different ions seem to prefer different electrospray conditions. Such differences include different potentials, various positions of the needle, differing pressures in the first vacuum region and even extraneous gas flow.

Having formed ions close to the front of the entrance to the vacuum instrument the ions are drawn through a transfer capillary into the first vacuum region, labelled as R1 in Figure 2.1. This capillary has an internal diameter of 600 µm and a length of 18 cm. From here the ions pass through a pinhole into a second differentially pumped region (R2) with an ion trap. The design of this ion trap will be discussed in more detail in section 2.1.3. The trap extracts the ions into the next region, (R3), containing the electrodes for a collinear Wiley-McLaren type time-of-flight (TOF) mass spectrometer.[7] The electrodes are comprised of three successive electrodes, named repeller, accelerator, and ground. All consist of relatively large thin flat plates with holes along the central axis. The accelerator and ground have the hole covered with a fine high-transmission mesh allowing ion passage but limiting the formation of inhomogeneous fringe fields. The first and second plates are pulsed

from ground to –2.3 kV and –1.9 kV, respectively, as the ion packet passes through between them. The difference in the potential applied to these plates defines the focal length of the TOF system.[7] The ions then travel the length of the drift tube, 1.3 m, with kinetic energies of the order of $\sim 2\ \mathrm{keV}$. At the beginning and end of the drift tube are a set of deflectors and an einzel lens. More will be said on the principles behind the einzel lens in section 2.2.1, but it suffices here to consider it to be the analogue of an optical lens but for charged particles. The deflectors consist of pairs of parallel plates arranged orthogonally to each other along the beam path. When a potential difference is applied across a pair of plates a linear field is produced that allows the beam to be steered in one direction, using both sets allows for control of the beam's trajectory in both off-axis directions. Approximately half-way along the drift tube is a pneumatically actuated gate valve to isolate the high vacuum detection region for the lower vacuum section of the machine. This is especially useful given the much higher occurrence of requiring access to the inside of the lower vacuum chambers.

The photoionization takes place in the final pressure region, R6. The laser beam enters through a calcium fluoride (CaF_2) window mounted perpendicular to the beam. The beam propagates across the chamber and interacts with the selected ion packet at the centre of a Velocity Map Imaging (VMI) stack. The light then continues until exiting the chamber through another CaF_2 window, this time at Brewster's angle to reduce the reflection back into the chamber. The reduction of scattered light is aided by having the windows mounted on narrow chamber extensions with light baffles present. However, electron noise is still seen for photon energies above the work function of the steel of the instrument. This is around 4.3 eV or 290 nm.[8]

The design parameters and intent of the VMI setup have been covered in depth before.[2,3,9] The original Eppink and Parker design has some design similarity to the geometry of the TOF optics, however, no meshes are used due to imaging requirements.[10] In our variation shown in Figure 2.2, the high voltages often used would be challenging as they would deflect the anion beam. Instead a reduced extraction field is used to pass the electrons into a resistive glass tube. This is achieved by imparting the same voltage to both of the external plates and

grounding the far end of the tube. The resistive glass allows for a particularly even gradient to the focal point of the electrostatic lens formed by the VMI plates. The smooth nature of the field allows for the minimum disruption to the electron path. The electrons finally are incident upon a dual micro-channel plate (MCP) arranged in a chevron configuration. This is then coupled to a phosphor screen which is subsequently imaged with a camera. The entire system is shielded using μ-metal, known for its high magnetic permeability. This property means that any magnetic flux in the vicinity would rather be present in the metal than the space inside, forming a magnetic shield. The MCPs are gated by a ~300 ns pulse. This allows for the reduction in background noise from the chamber by only allowing for detection for a period after the passage of the laser beam.

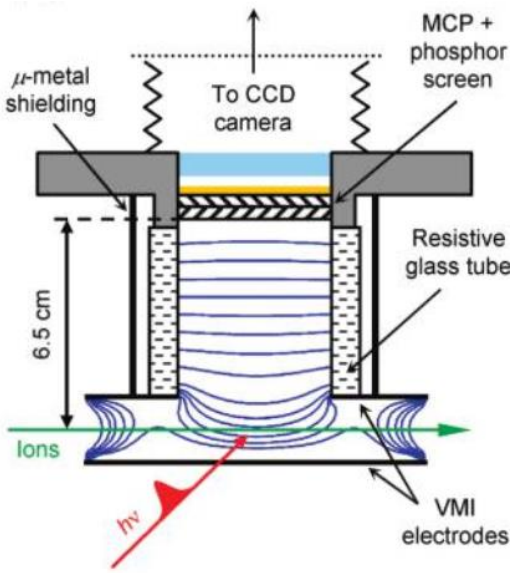

Figure 2.2 Schematic of the VMI setup of the experiment. The blue lines represent electric field lines as calculated by SIMION 8.0. Reproduced with permission from Ref. 4. Copyright (2010) American Chemical Society.

The photoionization event causes the production of a cloud of electrons that move up towards the MCP detectors. This then is flattened by collision with the detector. For the purposes of analysis, the 3D sphere data is required, thus it is necessary to reconstruct the sphere from the crushed 2D image. A deconvolution algorithm is used. The preferred methodology of this lab is that of Polar Onion Peeling (POP), a basis-set subtraction algorithm developed here previously.[11] This converts the flattened image that is seen on the detector into the relative components of the

central slice. This contains all the information for the subsequent analysis, including the radial intensity and anisotropy data.

The time of flight of the ions is measured after the VMI interaction region. This is done using another MCP chevron pair, but this is placed parallel to the incoming beam and ions are deflected onto it using a parallel plate at high voltage (–2 kV). This was the existing design with an original plan to implement a relectron, however, this is not currently in use.

Calibration is most often performed using the spin-orbit splitting of iodine. Atomic iodine produces extremely sharp photodetachment energy peaks, making it particularly useful for the calibration of the VMI stack. The first two states of the iodine atom are the $^2P_{3/2}$ and $^2P_{1/2}$ states with the $^2P_{3/2}$ state being the ground state.[**] Iodine has an electron affinity of 3.05905 eV with the $^2P_{1/2}$ state a further 0.94265 eV above that.[12,13] This means that for photon energies above 4 eV, or wavelengths below 310 nm, two peaks should be present in the photoelectron spectrum, as clearly visible in Figure 2.3. The data from the POP algorithm is initially only given in terms of the pixel radius relative to the defined centre of the feature. However, the kinetic energy of the electron (*eKE*) is proportional to the square of the radial position.

$$eKE \propto r^2 \tag{2.1}$$

Using this fact, and the spin orbit splitting above, two Gaussian functions are fit to the spectrum and a proportionality constant can be evaluated to map the radial position to kinetic energy space.

The spectrometer has a resolution of $\frac{\Delta E}{E} = 5\%$.

[**] See Section 1.1.3 for a recap of term symbols.

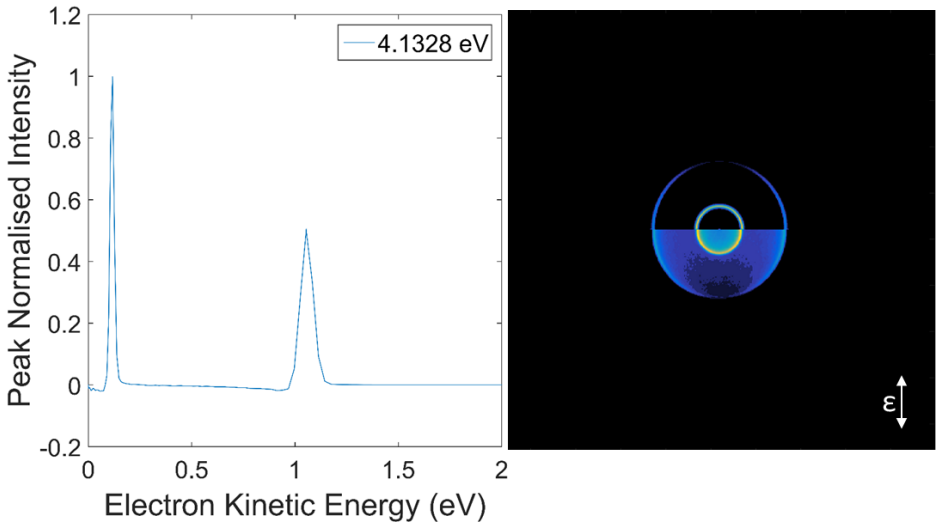

Figure 2.3 (Left) Example photoelectron spectrum of I^- at a VMI voltage of -500 V. The horizontal axis has been calibrated and truncated – data continues from approximately 0 to 11 eV. (Right) Both the raw image data, presented below, and the simulated central slice fit to the Legendre polynomials, upper. Laser polarisation axis indicated by the arrow down bottom right.

2.1.2. Laser System

A pair of laser systems have been employed for the data acquisition for this work. Both have been covered in more intricate detail in previous work, but a summary will be provided here for reference.[1]

The two systems provide contrasting and complementary experimental options. The physically simpler system is the nanosecond pulsed system. The main strength of this system is the variability of output wavelengths, as shown in Figure 2.4. The system comprises of two parts – a Q-switched Nd:YAG (Continuum, Surelite II) laser, the third harmonic (355 nm) of which pumps an optical parametric oscillator (OPO) (Continuum, Horizon I). The OPO relies on non-linear optical processes to split a portion of the pump beam into two different beams, the sum of which (in terms of energy) being equal to the pump photon wavelength.

Figure 2.4 shows the spectral range from the OPO, which spans from 192 nm to 2750 nm.[14] The pulses produced are $\sim$6 ns in length ($\sim$7 cm^{-1} spectral width) and are invaluable for the frequency-resolved photoelectron spectroscopy presented in later chapters.

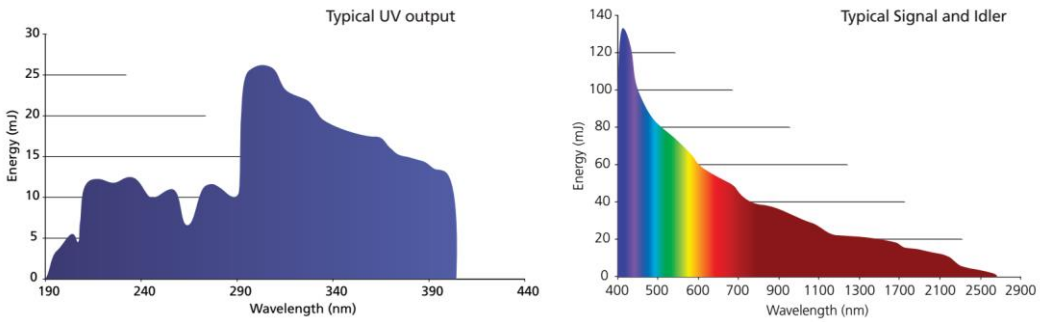

Figure 2.4 Typical power output from the Horizon OPO using a PL 8000 pump. Note the change in scale between UV and >400 nm performance. Reproduced from Continuumlasers.com[14]

The other laser system is a femtosecond laser system used for the time-resolved experiments. The primary components of this system are a mode-locked Ti:Sapphire oscillator coupled into a regenerative chirped-pulse amplifier.[††] Each of these systems requires a pump laser thus the process is as follows. The second harmonic (532 nm) of a 5 W continuous Nd:YVO_4 laser (Spectra Physics Millenia) pumps the primary Ti:Sapphire oscillator (Spectra Physics Tsunami) to produce a train of pulses at the fundamental frequency, 800 nm. This pulse train is characterised as having pulses of width ~ 35 fs at a repetition rate of ~ 76 Mhz with an average power of 0.5 W. This is then fed into the chirped pulse amplifier. To amplify the pulses, they are initially temporally broadened, otherwise the intensities could damage the gain medium. Once the pulse has been stretched, it is then amplified in the usual laser manner and then recompressed. In our system, the amplifier (Spectra Physics, Spitfire Pro XL) is pumped by the second harmonic of a 30 W pulsed Nd:YLF (Spectra Physics, Empower). The final output produces pulses of 800 nm fundamental frequency at a repetition rate of ~ 1 kHz and a power of 2.3 W. In recent time, we have chosen to run at a frequency slightly under 1 kHz (975 Hz) to avoid overtones from the mains power at 50 Hz.

The output beam is split and can be sent to a harmonic-generation stage to produce 400 nm, 266 nm or 200 nm using various β-barium borate crystals. An optical parametric amplifier is also available to produce wavelengths between 1140 nm and 2600 nm. The split beam also has one path interact with a mobile delay stage. This allows for the variability in relative delay between the pulses required for a

[††] See Section 1.3.3 for information on mode locking.

time-resolved experiment. The delay is afforded by simply increasing the relative path length of one beam.

2.1.3. Limitations

While this setup has been invaluable in the research undertaken by this lab since its construction, it has been observed to have some limitations. One of the major outcomes of this thesis was to resolve two of these limitations by altering the design of the ion trap.

The existing trap is based on a stacked ring trap similar to that proposed by Gerlich.[15] The major limitation of the design as it stands is that of scale. As can be seen in Figure 2.5, the internal volume available for trapping is quite small. Simulations estimate the trap volume as $\sim 0.2\ \mathrm{mm}^3$.[3] When considered with the space-charge limit of $10^3\ \mathrm{charges\ mm}^{-3}$, the estimated ion packet size was ~ 200 ions.

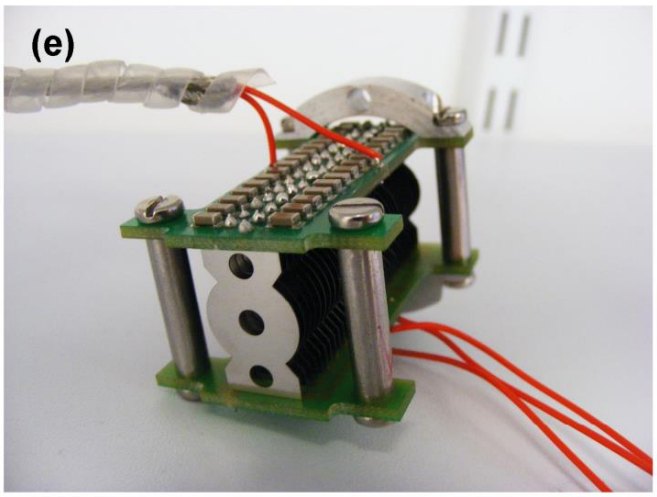

Figure 2.5 Existing ion trap shown from the end. For scale, the central axis hole is 3.2 mm in diameter. Reproduced from [3]

This low number increases the duration of data acquisition for all experiments and precludes study of any species with too small a photodetachment cross section. This is especially noticeable when performing time-resolved measurements, due to

the number of repeat measurements required to build up data at all time delays. The longer the data acquisition, the more challenging it is to maintain the constants of the experiment, such as laser power and ion packet size. The first design requirement was therefore to increase the ion throughput of the trap.

The other limitation is best discussed with reference to some previous work. When studying the dynamics of nucleotides, differences were observed between the solution phase and the isolated gas phase.

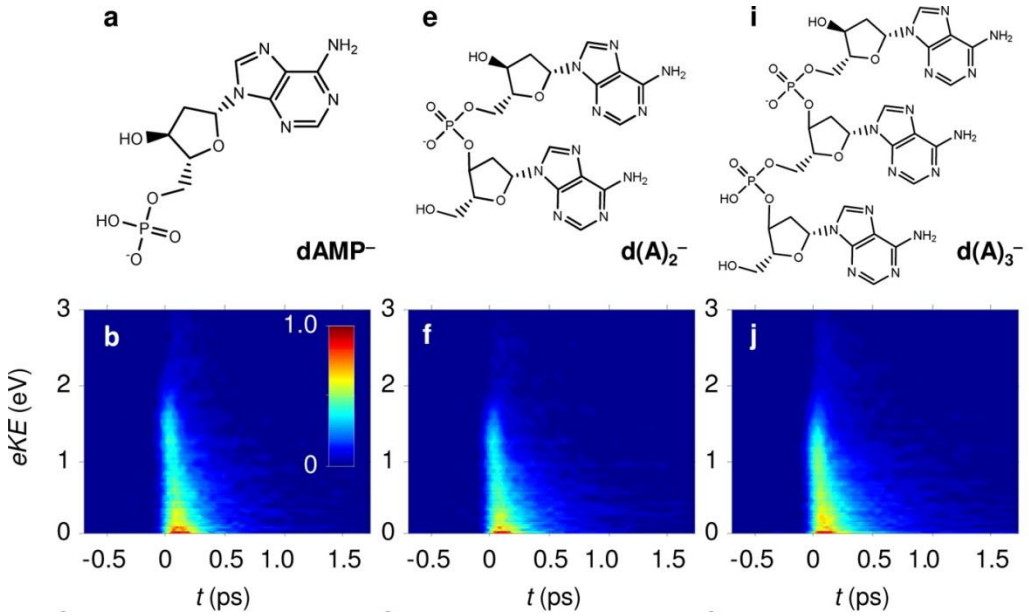

Figure 2.6 The structure, (a, e, i) and corresponding time resolved photoelectron spectra for increasing sections of adenosine based oligonucleotides. Reprinted with permission from Ref 16. Copyright (2014) American Chemical Society.

Without going into detail as to the exact mechanism of the excited state decay of each of the oligonucleotides, what is immediately obvious from Figure 2.6 is that there is no major alteration of the decay mechanism as the phosphate backbone of the DNA is increased in length. The spectra shown were subject to a global fit and produced a two-component decay, the lifetimes of which are listed in Table 2.1. These values numerically confirm the visual hypothesis that there was little difference in the speed of the decay between the molecules.

Table 2.1 Decay lifetimes for the two decay processes present in the global fit to the time-resolved data of $dAMP^-$ and subsequent oligonucleotides. Data from Ref.16

Decay lifetime	$dAMP^-$	$d(A)_2^-$	$d(A)_3^-$
τ_1	26 fs	26 fs	28 fs
τ_2	288 fs	337 fs	380 fs

Contrast this with Figure 2.7, showing transient absorption of similar oligonucleotides, but now present in a solution rather than as unrestricted gas molecules. The crucial contrast is that in solution the addition of a second monomer to form $d(A)_2^-$ immediately makes a marked change to the decay process. Signal is still measured out after 100 ps, while the gas phase decay is all but complete after 1 ps.

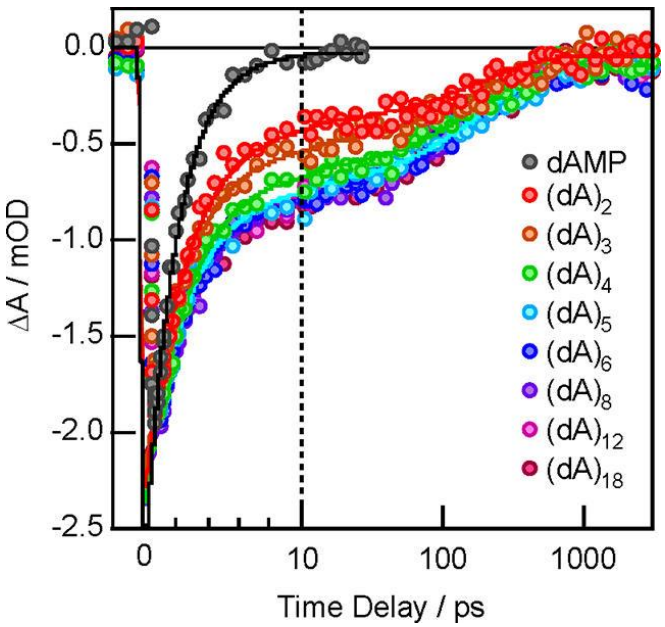

Figure 2.7 Transient absorption signals of dAMP and similar adenine homo-oligonucleotides in water. The horizontal axis is linear to 10 ps and then logarithmic. Reprinted with permission from Ref. 17. Copyright (2012) American Chemical Society

The mechanism proposed for this change was linked to the physical structure of the system in solution. In aqueous solution, the hydrophobic bases are preferentially brought together and undergo a stacking process. Visually, this corresponds with the standard picture of DNA, with the phosphate groups forming a helical backbone and the bases stacked alongside. However, this was not occurring when in isolation,

as seen by the lack of long-lived decay in Figure 2.6. Several reasons were expounded as possible causes, including the solvent causing stacking by the unfavourable base interactions, destabilisation due to the nearby charge on the phosphate group or that the entropic cost of the stacking process at the temperature of the ions is too great.

The relative population of these two conformers, stacked and unfolded, as a function of temperature has been established by ion-mobility spectrometry (IMS).[17,18] This technique separates molecules by their collisional cross-section, which is considerably different for these two conformers. For $d(A)_2$, Bowers and coworkers showed that the stacked configuration is the lower energy conformer, but at 300 K both the stacked and the open conformer are present because of the entropic contribution. Upon cooling to 80 K, the stacked arrangement was preferred at a ratio of 3:1.

As mentioned previously the temperature of the ions in our experiments is at least 298 K.[19] While this is the lowest expected temperature, it is entirely plausible that the actual temperature is considerably higher. Trap extraction voltages used were quite high, $\sim 100\ \mathrm{V}$, and the pressure in the trap, $\sim 1\times10^{-3}$ Torr, is too high for all of that energy to be converted into kinetic energy, some collisions with the background gas will occur and thus the ions will be heated. The second design requirement was therefore to allow for temperature control and in particular cryogenic (77K) temperatures for the ion packets.

2.2. Ion Trap Design

2.2.1. Ion Control and Confinement

Before covering the details of the new design, there will be a discussion of ion control.

The simplest form of ion control is that of electrostatics. This works by utilising some combination of the attractive and repulsive nature of similarly charged

particles. The planar deflectors mentioned in section 2.1.1 and einzel lenses are both good examples of electrostatic ion control.

The einzel lens, at its simplest, consists of three identical ring-like electrodes arranged in sequence that the charged particles pass through. Typically, the first and last elements are grounded while the central portion is raised or lowered in potential to achieve the appropriate lensing. The principle has much in common with a biconvex optical lens. A simple ion guide can be constructed of sequential einzel lenses.[20] While this is an appealingly simple concept, in practice it is significantly more challenging. As with einzel lenses, a critical requirement is the relatively unhindered and rapid motion through the lens assembly. While it is entirely possible to construct an einzel lens using either an attractive or repulsive central barrier, the incoming kinetic energy is crucial as to the outcome.

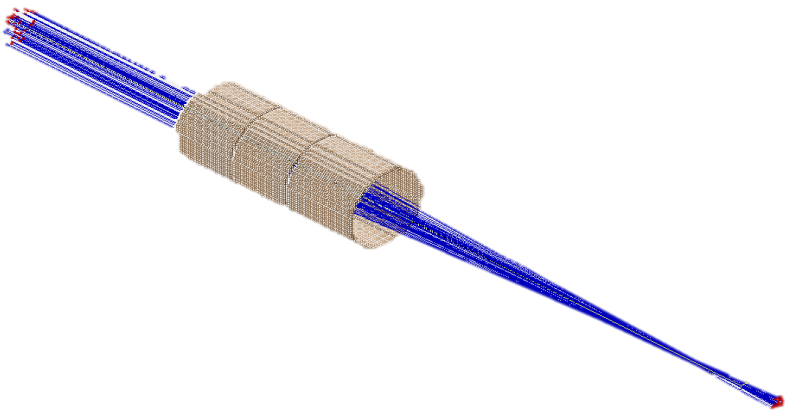

Figure 2.8 SIMION representation of a typical einzel lens operating under ideal conditions. The red points denote either initial or final positions with the blue lines as the trajectories between them.

Under normal conditions the ions will experience the curved field between the elements and convene on some focal point. If there is insufficient lateral motion, for example when ions are in a stationary gas at rough vacuum, then ions will simply react to the potentials and most likely crash into an attractive element or ground.

One last similarity with optical lenses is worth noting. Just as an optical lens will focus different wavelengths of light at slightly different distances, an einzel lens will focus different kinetic energy particles at different distances. This becomes

particularly noticeable when the spread of kinetic energy is large as a proportion of the total kinetic energy.

When considering that a trap requires the ion to be as close to stationary as possible, it is clear that simple electrostatics are insufficient to achieve this. This is overcome by the use of inhomogeneous radio-frequency (RF) fields.[15] Consider the motion of a particle in a homogeneous oscillating field as in Figure 2.9. As (b) shows, the particle will move in response to the oscillating field but averaged over time there is no net movement of the particle. If the previously parallel electrodes are bent into a concentric circle arrangement, shown in dotted lines in (a), the field is no longer homogeneous, and the particle is seen to drift slowly towards the weaker field region. It is this net movement that is critical to the success of RF traps.

The geometry is the key to controlling the inhomogeneity required to coax the ions towards a point. One of the most well-known of the design for this is a Paul trap.

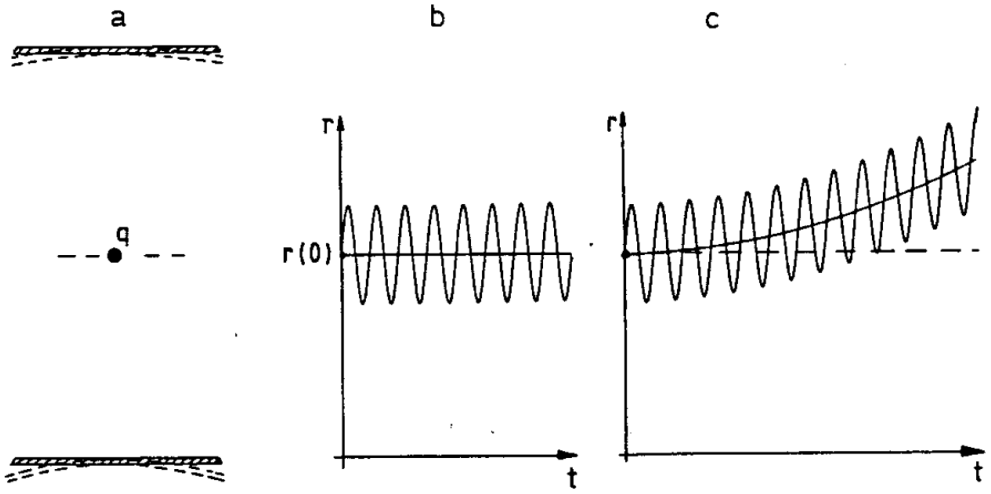

Figure 2.9 Motion of a charged particle in a varying electric field. (a) Schematic of the physical situation. (b) Motion of the charged particle, q, around its average position, r(0), under the conditions of flat parallel electrodes. (c) Motion under the inhomogeneous conditions of bent electrodes – dashed lines in (a). Reproduced from Ref. 15 with permission from John Wiley & Sons, Inc., Hoboken, NJ, USA.

The Paul trap usually consists of 3 parts, a ring and two end caps. The inside surfaces are ideally shaped as hyperbolae. The ring has an oscillating RF applied to it, while the end caps receive a signal that is in antiphase with that of the ring. This produces a “saddle” potential that oscillates, as shown in Figure 2.10 (b).

The potential inverts and charged particles are drawn to the centre. This can be mechanically demonstrated, by machining a part with the surface like the potential and rotating the part. A sphere can then be introduced to the centre and it will remain there.

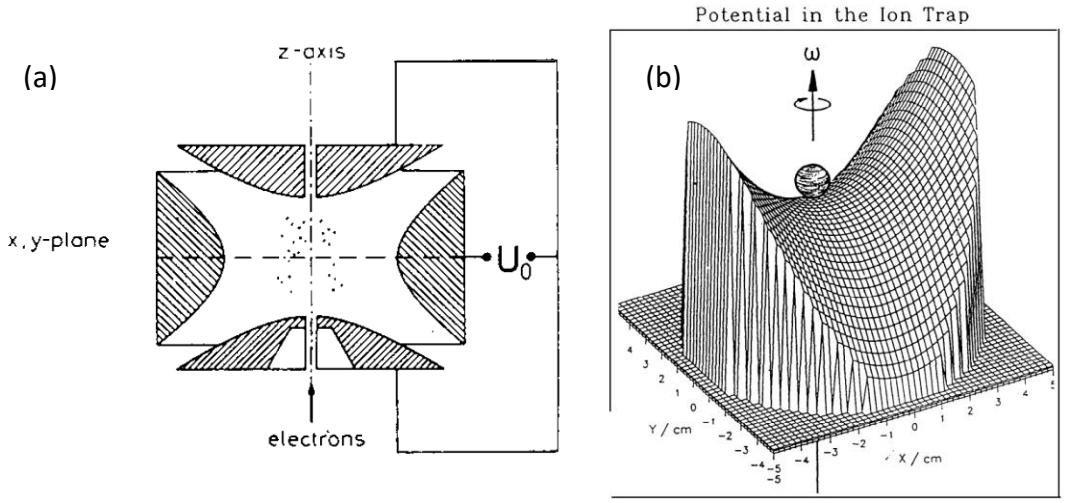

Figure 2.10 (a) Cross-section of a conventional Paul trap, showing the hyperbolic surfaces and central trapping location. (b) Representation of the potential within the trap. Adapted from Ref. 21

This standard design can be seen as a "point" trap as it has a confining force in all three dimensions, there are variations that only confine in two. These are often known as guides as they can confine ions along a central axis. The simplest of these consists of four parallel bars connected such that adjacent bars are in antiphase. This quadrupole again produces something of a saddle and as such the ions are confined to the central axis. Linear traps can be constructed by adding end caps to such an arrangement. It is entirely possible to add more poles to the system, such as the octupole guide shown in Figure 2.11. The central region shows the confinement area.

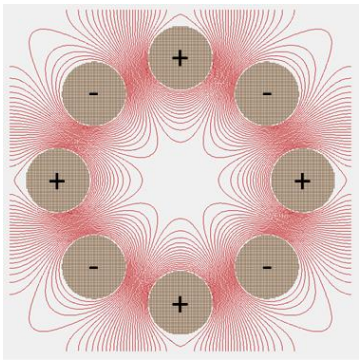

Figure 2.11 Cross-section across an octupole ion guide with red lines showing contours of electric potential. + and – indicate the relative phase of the RF applied to the rods.

When considering the confining qualities of multi-pole electrode systems such as the quadrupole ion guide, it is worth being aware of the effective trapping potential. When considered as a radial function from the centre, a particle in a quadrupole experiences a quadratic effective potential as seen in Figure 2.12. Further pole additions cause the potential to have a higher radial dependence until the ring electrode trap. This is the design of the existing spectrometer, where instead of alternating phases applied to electrodes that continue along the axis of movement, alternating phases are applied to adjacent rings that are perpendicular to the central axis as seen in Figure 2.5. A key benefit of the ring-electrode trap is that its radial volume is in principle the largest of all RF traps.

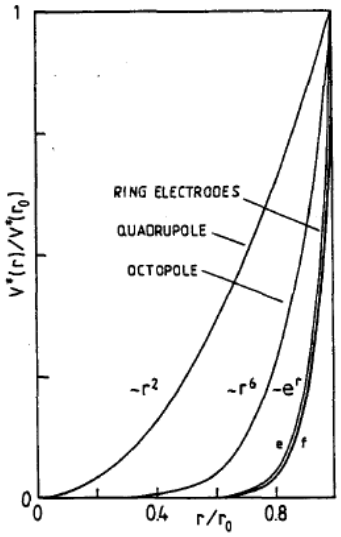

Figure 2.12 Effective potential, V*(r), scaled relative to the maximum internal radius, r_0. Reproduced from [15] with permission from John Wiley & Sons, Inc., Hoboken, NJ, USA.

The above discussion has been considered under a perfect vacuum with no considerations for collisions. However, collisions are complementary to the small central force of an ion trap. By an energy conservation argument, it can be seen that an ion entering a trap with significant kinetic energy could just bounce straight back out the way it came in, thus collisions can help to reduce the kinetic energy of the ions to keep them in the trap. For a Paul trap, the usual methodology is to introduce a small pulse of gas that is then pumped away. This means that there is initially gas around to absorb the kinetic energy of the incoming ions, but it is not present when the ions are extracted. However, this methodology comes at a price, time. Getting the gas in and out of the trap takes a finite quantity of time and as such Paul traps are more comfortable running at low repetition rates. While this is not a major consideration when used with the nanosecond laser system described earlier which typically operates at 10 Hz, it becomes positively wasteful when combined with the femtosecond system, as most laser pulses do not interact with an ion packet. Thus, the final design requirement was a trap that can operate at the repetition rate of the femtosecond laser, $\sim$ 1 kHz .

2.2.2. New Trap Design

Having covered the principles behind ion trapping and the major design requirements, the actual design process required a large quantity of gradual refinement. This was made more challenging by the sheer number of interlinked variables present. The final design consists of a long linear stacked ring-electrode trap with a two-part gradient and a repulsive end wall. The reasoning for these decisions will be discussed here. The ion trap was modelled in the SIMION 8.0 package using parametric geometry and a selection of custom Lua scripts to control both the AC and DC voltages along with a hard-sphere collision model adapted from the examples given with the software. [22]

The simple representation is that the ion is radially confined by the application of the RF field from the stacked ring electrodes forming a wide tube in potential energy space. This is then “tilted” by the application of a potential difference across the trap, with each ring having a slightly different DC point. This causes the ions to

have a net motion along the cylindrical axis of the trap. Finally, the end is sealed using the repulsive wall and a trap volume is created very close to the extraction pinhole.

The ideal trap should allow for sufficient collisions with background gas to remove kinetic energy and enable trapping, while also avoiding collisions with background gas when extracting from the trap as this would heat the ions. We decided to resolve this conundrum by using a long asymmetric trap with a final storage volume near the end, relying on the fact that the number of collisions is proportional to the distance an ion travels.

A pressure regime was found, coupled to a long travel length along the trap, that allowed for the right number of collisions. Upon first entering the trap the ion would bounce off the repulsive wall at the far end, usually only colliding with a buffer gas molecule at most once per repulsive wall oscillation. The two-part gradient allowed for a much steeper gradient to be present at the culmination of the trap and, as such, a much more confined trapping volume. While an increased trapping volume was a desired outcome, the shape of the trap volume is still important. Too long a trap volume along the cylindrical axis of the machine could cause a significant stretching of the packet when it was extracted into the TOF region and thus a significantly worse TOF resolution.

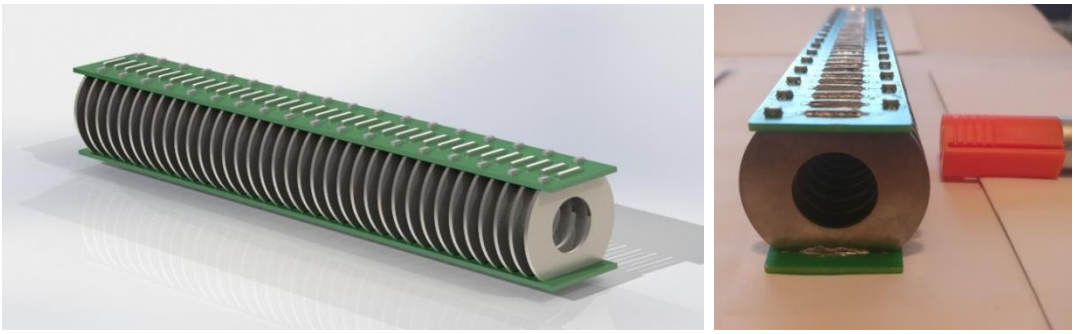

Figure 2.13(Left) Rendered image of the final trap design. (Right) End view of a completed trap, whiteboard marker for scale.

The final physical design for the trap consists of 36 identical stainless-steel electrodes with an internal diameter of 18 mm. The electrodes themselves are 1.5 mm thick with a repetitive spacing of 5 mm. Due to the colossal size of the variable

space it would be overconfident to establish these as a global maximum of design, however simulations indicated very good radial trapping and storage at the end of the design, as shown in Figure 2.14.

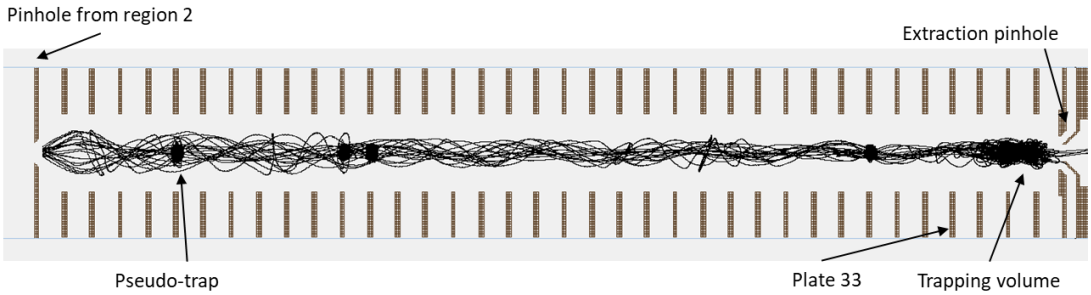

Figure 2.14 Cross sectional view along the trap during a simulation in SIMION. Particles were given a single charge and mass of 25 amu. The simulation also used a hard-sphere collision model at a pressure of 5 x 10^{-4} Torr.

The potentials applied to the electrodes consisted of the RF for the radial confinement as discussed previously but with each electrode subject to a different DC potential. The final design uses two linear gradients along the length of the trap, with the transition at plate 33, labelled in Figure 2.14. Other possibilities were evaluated, such as flat wells for a trap and even quadratic and exponential curves. The gradient of the DC potential at the end-cap defines the depth of the trap volume in that dimension. While both of the alternative curves also generated a compact trap volume, there was little dramatic improvement over the linear variation. The steeper trap gradient was applied over the final 4 electrodes of the trap. This is visualised along with the relevant control points in Figure 2.28.

2.2.3. Theoretical Trap Performance

When attempting to establish the performance of a trap, criteria are required to numerically compare assorted designs and configurations. Various criteria for performance were proposed, the following were used:

- Fast accumulation
- Low trap losses
- Large trap volume
- High pulse throughput
- Short extracted pulse length

Fast accumulation was evaluated as the proportion of molecules that were in the trap after a certain time. It was observed early on that if there was insufficient DC gradient along the trap, pseudo-traps would form parallel to the plates. A few can be seen in Figure 2.14, with the labelled one above the fifth plate especially noticeable. Trap designs with too great a plate spacing were especially prone to this.

Trap losses were defined as those ions that crashed into an electrode before such time as the extraction pulse was triggered. This could be considered as the sum of two different possibilities – escaping radially due to insufficient confining force or colliding with the end cap due to having too much kinetic energy for the barrier.

The trap volume is representative of the maximum number of ions that can be stored, due to the space charge limit. This is set at $\sim 10^3$ charges per mm^3, allowing for multiply charged ions.[23] Attempting to simulate the trap filling by concurrently simulating all the ions was almost instantly impractical. Running 100 concurrent ions through the simulation could easily take a weekend of run time. The trap shape was evaluated by applying an increased Coulombic repulsion between the ions, such that for their mutual interaction, their effective charge was equivalent to 100 electrons. This simulated the effect of Coulombic repulsion, but for a much larger

number of ions than was actually run. It is assumed that the density of charge in the trap does not affect the surface charge of any of the electrodes. The volume generated was approximated to a cylinder and measured from the ion trajectories.

The final two criteria – high pulse throughput and short pulse length - deal with the ions' extraction from the trap. The design of the extraction optics/repulsive barrier went through many iterations before the final one was chosen. The cross-section of this can just be seen on the far-right of Figure 2.14, and in much more detail in Figure 2.15. The end cap was split into two parts, labelled in Figure 2.15 – one that remained at constant repelling potential, (a), and the other that switched to change the nature of the end of the trap from confinement to extraction, (b). When the narrower aperture component was switched, the nearby repulsive field from the other component caused a marked lensing effect. This allowed for the passage of an ion packet that was of considerably larger dimensions through the pinhole into the next chamber. The extraction parameters were optimised under a different simulation once a good storage regime was found, this was then passed back and forth as changes were made and checked for alterations in behaviour. The extraction simulation was designed to start from a condition of trapped ions rather than checking for trapping – this made for much faster evaluation.

The pulse throughput was evaluated as the proportion of the ions contained within the trap that were successfully extracted. The plates for the existing TOF setup were added to the simulation and made for an ideal zone for measurement. Successful extraction consisted of entering the space between the first two TOF plates through the 5 mm diameter hole in the first plate.

The pulse length at this point was also important for TOF resolution. A temporally broad extracted pulse would struggle to be properly focussed by the TOF optics, and completely ruined if the ion packet was so spread out in space and time that some ions could pass through the TOF plates before others had arrived. A perfect scenario would move the disc-like distribution of the trap to the centre of the space between the repeller and accelerator plates of the TOF optics. This was impossible to achieve, as the aperture between the two vacuum regions had to be smaller than

the radial dimension of the trap volume. Pressure considerations will be discussed properly in section 2.3.2 but it is sufficient to say here that a conductance restriction was required between the trap conditions, where occasional collisions are expected and beneficial, and the TOF region where collisions are to be avoided.

Considering the passage of the ions from the disc-like trapping region through the smaller aperture into field-free space, it is immediately obvious that such a beam will be divergent and in particular, more divergent the closer the trapping region is to the aperture. Thus, a trapping region closer to the end cap will be more likely to form a temporally cohesive bunch but is also likely to be physically sparse due to divergence. To deal with the divergence, an einzel lens was added after the extraction plate and before the TOF optics to collimate the divergent beam, as shown in Figure 2.15. As noted, this einzel lens has an increasing internal diameter along its length. This is due to requiring slightly different radii of convergence and divergence caused by the lens.

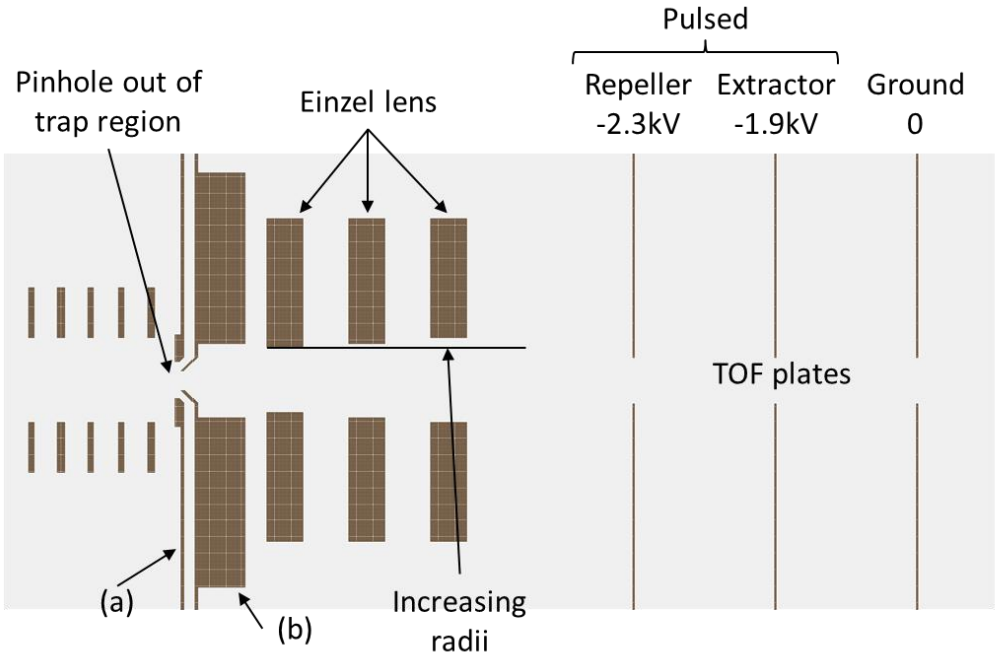

Figure 2.15 Cross section view of the extraction simulation geometry, showing the bipartite nature of the extraction pinhole along with the extra einzel lens and the three components of the TOF optics. Electrodes (a) and (b) form the end cap of the trap. Switching of (b) opens the trap for ion extraction. While the second and third TOF electrodes have mesh in this simulation, at this magnification SIMION has neglected to show this.

Evolution of the trap scheme relative to the criteria culminated in the design as shown in Figure 2.15. Pseudo-traps were avoidable with almost perfect trap retention. A typical trap volume is shown Figure 2.16. As can be seen, the volume is not a perfect cylinder, the end faces are curved. However, it was assumed that the curves were parallel for the purposes of volume calculation. Depending on the voltages applied to the system the trap volume can change dramatically. Under "realistic" conditions the estimate is that trap volume is $\sim 80\ \mathrm{mm}^3$. This would correspond to a maximum of ~ 80000 ions that could be stored.

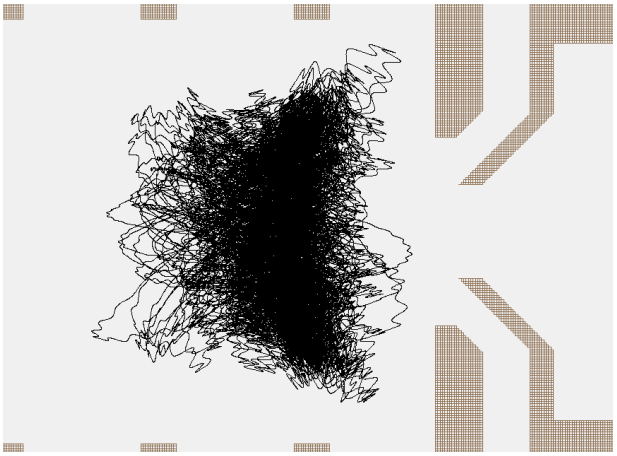

Figure 2.16 Cross section of a typical trap volume. This shows the usual shape – somewhat disc-like, but more a shape like a thickened contact lens. The trap volume here is estimated at 70 - 120 mm^3

The trap extraction efficiency is estimated at $\sim 70\%$. $\sim 75\%$ of the extracted ions followed trajectories into the TOF optics and could subsequently be accelerated as an ion packet by pulsing the repeller and extractor electrodes.

2.2.4. Ion Guides

While achieving improved throughput for the trap was an explicit design requirement, the implicit requirement was to increase influx to the trap to ensure that the increase in theoretical throughput could actually be realised. Considering the ion influx to the spectrometer as a Fermi problem gives the following estimate for ions produced by the electrospray at the front of the machine.

$$\begin{aligned} &(\text{Solution concentration}) \times (\text{Flow rate}) \\ &(1\text{mM}) \times (200\mu\text{L hr}^{-1}) \\ &(10^{-3}\ \text{mol dm}^{-3}) \times (10^{-5}\ \text{dm}^{3}\ \text{hr}^{-1}) \times (10^{-3}\ \text{hr s}^{-1}) = 10^{-11}\ \text{mol s}^{-1} \end{aligned} \tag{2.2}$$

Converting the number of moles to a raw number of ions gives an estimate for the rate of ion production from ESI:

$$(10^{-11}\ \text{mol s}^{-1}) \times (10^{23}\ \text{ions mol}^{-1}) = 10^{12}\ \text{ions s}^{-1} \tag{2.3}$$

Conversely, to run the trap at maximum throughput would need:

$$\begin{aligned} &(\text{Number of ions per pulse}) \times (\text{Number of pulses per second}) \\ &(10000\ \text{ions pulse}^{-1}) \times (1\text{kHz}) \\ &(10^{4}\ \text{ions pulse}^{-1}) \times (10^{3}\ \text{pulse s}^{-1}) = 10^{7}\ \text{ions s}^{-1} \end{aligned} \tag{2.4}$$

This shows that there are 5 orders of magnitude difference, however this does not take into account how many ions are lost by not entering the input capillary. Unfortunately, estimates of the efficiency of ESI are that only one in every $10^{3} - 10^{5}$ sprayed ions are introduced to the interior of a vacuum chamber. This means that for optimal trap pulses, almost all ions that make it into the first vacuum chamber need to reach the trap.

To achieve this quantity of throughput, ion guides were proposed. Initial designs included using the electrostatic ion guide as proposed by Guan and Marshall.[20] However, as alluded to in section 2.2.1, problems were encountered due to the pressures of the background gas. These could be overcome with the use of a considerable potential difference across the whole guide, in an analogous manner

to that of the trap. However, the uncertainty in the physical requirements quickly became too much. When considering the first vacuum region with a pressure of ~ 1 Torr, the expectation was that flow dynamics would need to be an additional consideration. The collision model of SIMION allowed for there to be a net movement of the background gas and so this was used as a quick approximation, neglecting any concept of vortices or Mach discs that would be quite possible.[24] This simplistic model showed a colossal dependency on the gas movement, resulting in orders of magnitude difference in the required potential for successful transmission. While the design was appealing from an electronics perspective, this dependency made it unfeasible in practice.

Making a minor change to the trap design resulted in a simple ion guide for higher pressure throughput. The two-part linear gradient was altered to be just a single linear gradient across the guide. The repulsive end-cap that formed the trap was also obviously removed.

2.2.5. Electronic Design

While simulating the combination of RF and DC present in the trap and ion guides was relatively simple, electronic design was required to bring this safely into the lab. The previous design, shown in Figure 2.17, was based upon a single resistor chain and would no longer be appropriate.

Having the different phases connected within the vacuum means that the maximum peak-to-peak voltage will be across the resistors. These were prone to failure due to excessive voltage. Furthermore, voltage across a resistor causes current, which generates heat. Due to the scale of the previous trap, relatively low RF voltages were required for trapping, so heating was minimal.

Simulating the voltages required for the new physical design with the previous electronic design predicted ~ 0.5 W per resistor of heating within the vacuum.

Given the intention for cooling, a trap design that generated 18 W of heat in the chamber required some changes.

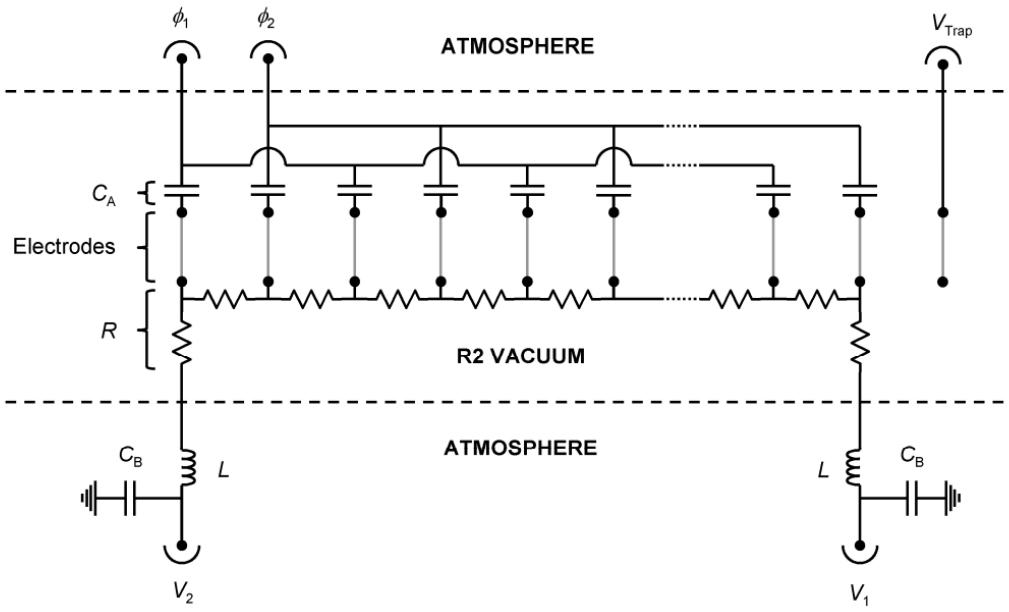

Figure 2.17 Circuit diagram of the existing trap. For the purposes of discussion here, the values of the components are not important. φ_1 and φ_2 represent the two antiphase RF voltages (1 MHz, 100-250 V peak-to-peak). Reproduced from [3].

The solution was to have two parallel resistor chains, one for each phase. This drastically reduced the power dissipation within the vacuum as the resistor chain only sees the DC voltage across it. Simulation gives an expected power of $\sim 0.5\ \mu W$ per resistor.

When considering the decoupling circuit, the preference was to have the controls for the system remain as uncluttered as possible. This meant that one voltage supply would provide the DC voltage for both phases of a guide, with the relevant offsets being handled by the circuit. For the guide circuitry, this was achieved simply by use of resistors with 1.5 x magnitude that of the rest of the chain. When designing the trap, one phase required the use of a pair of 0.5 magnitude resistors with the off-board connection between them. This was the isopotential point required for simple control.

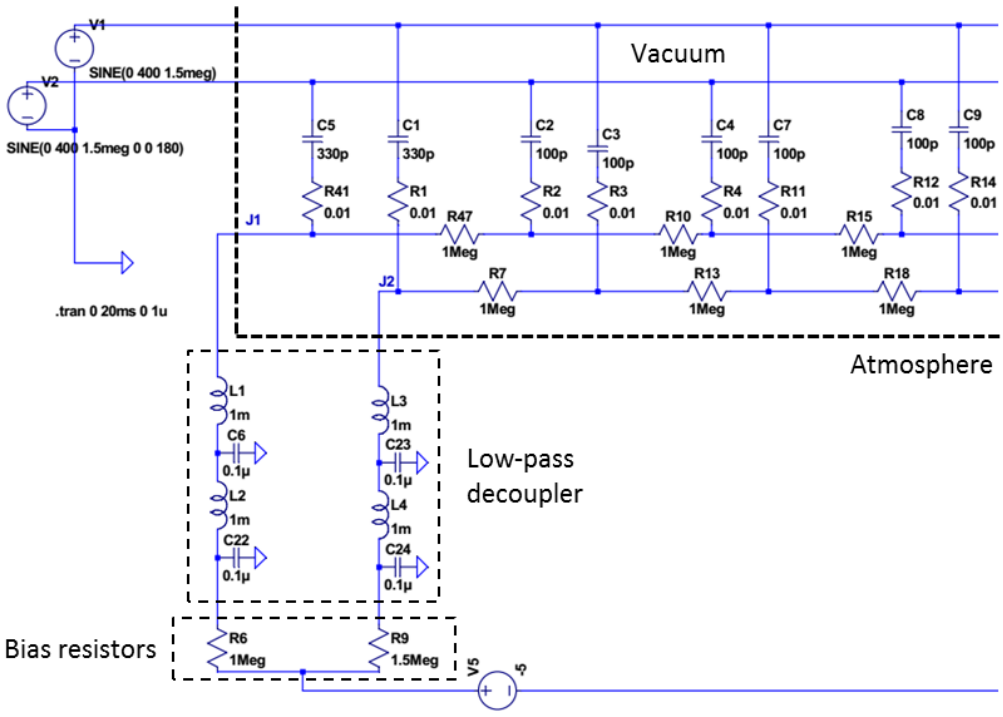

Figure 2.18 Truncated circuit diagram showing the principle of the trap electronics. Voltage sources in the upper left are the RF supply, the 0.01 Ω resistors represent the electrodes. The voltage source at the bottom provides the DC component across the trap/guide. The points labelled J1 and J2 are connections off the board in the final physical design. Both the low-pass decoupler and the bias resistors are housed outside the vacuum chamber. All values shown are correct with respect to the final design in use.

A final unexpected problem was discovered while the guides and trap were under construction. The RF amplitudes on electrodes near the ends of the guides were observed to be significantly reduced with respect to the rest of the system. This is believed to be due to the inherent capacitance between the electrodes, with the expectation that it would be different at the end due to the lack of symmetry. This was fixed by tuning the coupling capacitors for the circuit, as can be seen in Figure 2.18 where C1/5 are different value to the rest of the circuit.

Physically, the design is split to have the capacitors and RF connections on a printed circuit board (PCB) above the rings, while the resistor chain and DC connections are on a similar PCB underneath. Previous electrodes were held in place by two thin pins. To remove the possibility of non-parallel geometry due to construction, the electrodes were connected to the PCBs using a through-plated slot, shown in Figure 2.19.

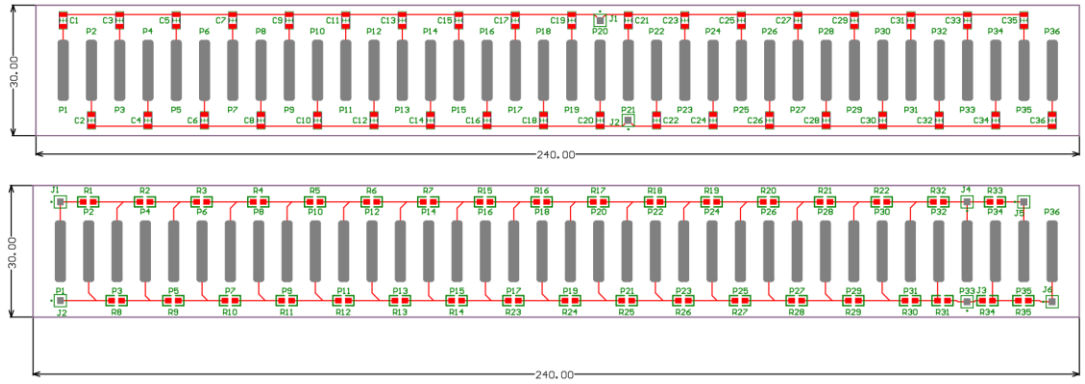

Figure 2.19 Board layout for the circuit boards for the trap.

2.3. Physical Design

2.3.1. Cooling

The simplest method of cooling an ion trap such as a Paul trap is to place it in contact with an existing cold head.[25] Thus, the gas inside will thermalize and then the ions trapped within will too. The stacked-ring electrode design shown in Figure 2.13 and Figure 2.14 should work in a similar manner, with nearby surfaces having thermalized with the backing gas.

A possible flaw in this plan comes from the difference in the electronics of these two designs within the vacuum chamber. A Paul trap has no components within the chamber, and thus the efficacy of the trap can be assumed to be constant at cryogenic temperatures. The design proposed above has components present so inevitably they will be exposed to cryogenic temperatures as they are in physical contact.

It was decided to use liquid nitrogen as the cryogen of choice, due to its abundance and relative cheapness. This would expose the materials to $\sim 80\ \mathrm{K}$. The composition of the capacitors was chosen as NPO ceramic to minimise the effect of the cryogen.[26] The resistors were shown to be relatively unaffected.[27]

The components being present raised the further problem of ensuring good thermal contact with the cold surface. As the cold surfaces are usually metallic (i.e. copper) and conductive, this would cause a short. Sapphire is a common non-electric but good thermal conductor, but would retain the contact problem. To combat this, a thermally conductive and electrically insulating gap filler was used (Parker Chomeric G580).

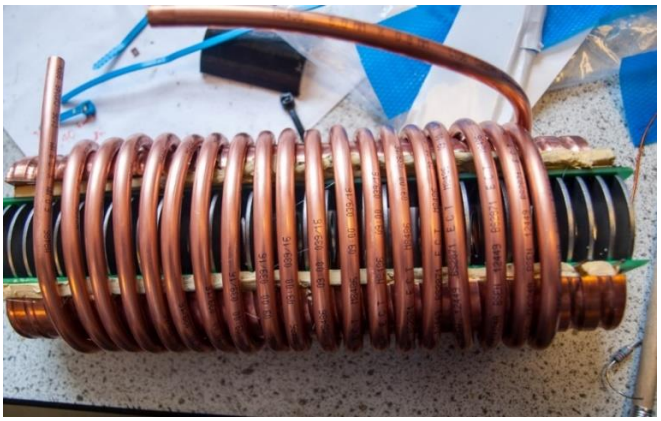

Figure 2.20 Early cooling design using pipework as the in-vacuum reservoir.

The final challenge was the shape of the liquid nitrogen container. An early attempt tried to use pipework as the container. This was achieved by “sandwiching” the trap with pair of ridged copper bars. The bars had a hemispherical cross section with spiral grooves cut into them. The pipework was then wrapped around the trap and copper to achieve the clamping force required for good thermal contact. This is shown in Figure 2.20. While all the copper pipework is visually appealing, the design did not work. Due to the custom nature of the system, a pressured liquid nitrogen system was unfeasible. Under a gravity feed, the cryogen did not make it all the way through the pipe.

A different approach was required. The next design consisted of a large reservoir above that would then be clamped around the boards using tapped posts and bolts. Ideally all would be made of copper again. Copper was chosen due to its high thermal conductivity.[28] However, using copper proved challenging to manufacture the reservoir as it invariably warped around the soldered joints. The final compromise was to construct the reservoir from stainless steel with the other components, posts and lower sheet being made from copper, shown in Figure 2.21.

This provided the best combination of thermal conductivity, strength and ease of manufacture.

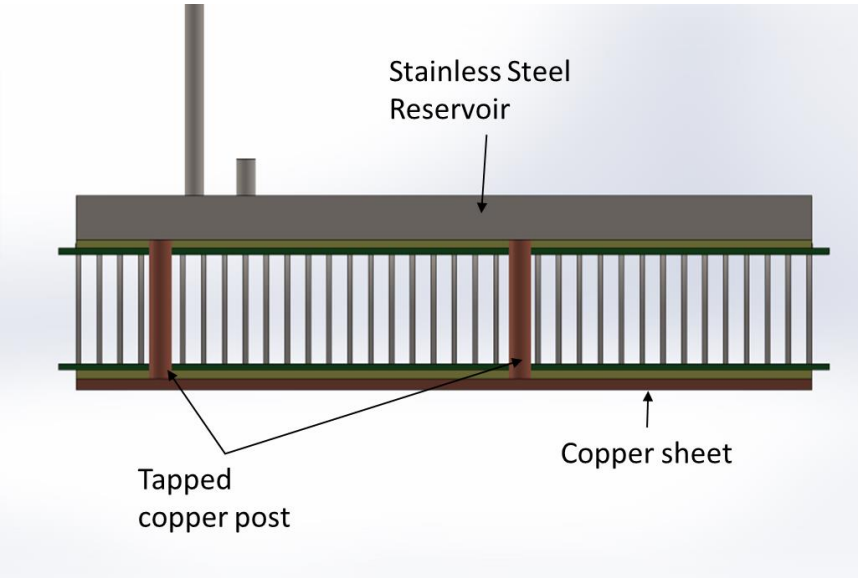

Figure 2.21 Final reservoir and clamp design for the trap.

2.3.2. Vacuum Considerations

Running a spectrometer that makes use of both electrospray ionisation and photoelectron imaging necessitates the use of different pressure regimes. ESI requires (relatively) high pressures and in our setup is run at atmospheric conditions. Conversely, techniques such as TOF mass spectrometry and VMI require high vacuums. To achieve this, the spectrometer has been divided into several differentially pumped chambers.

Considering the number of chambers required and pumping systems, the obvious preference is to achieve the most for the least waste or expense. This meant using existing pumps where possible and to thus minimise the number of extra regions added. When considering the chambers and the pumping required, there were desired pressures. These are shown in Table 2.2. For this discussion, region 3 is as labelled in Figure 2.1, containing the TOF optics.

Table 2.2 Initial vacuum conditions and desired outcomes.

Location	Known or desired pressure /Torr
Atmosphere	760
Trap	$\sim 1.0\times10^{-3}$
Region 3	$\leq 1\times10^{-6}$

The previous design had a pressure of 2.5×10^{-3} Torr within the trap region. This would be too high for the new design and was a key source of heating upon ion extraction. Furthermore, the previous pinhole into the trap had an interior dimeter of $1\ \text{mm}$. Using this diameter aperture between the regions with the simulated ion guide resulted in poor throughput due the difference in scale between the ion cloud and the pinhole. However, to increase the size of the aperture would necessarily increase the pressure in the trap region to even further from the desired pressure. To solve this, another vacuum chamber was added. A simple representation is shown in Figure 2.22. This would allow for the pressure in the trap region to be in the desired range.

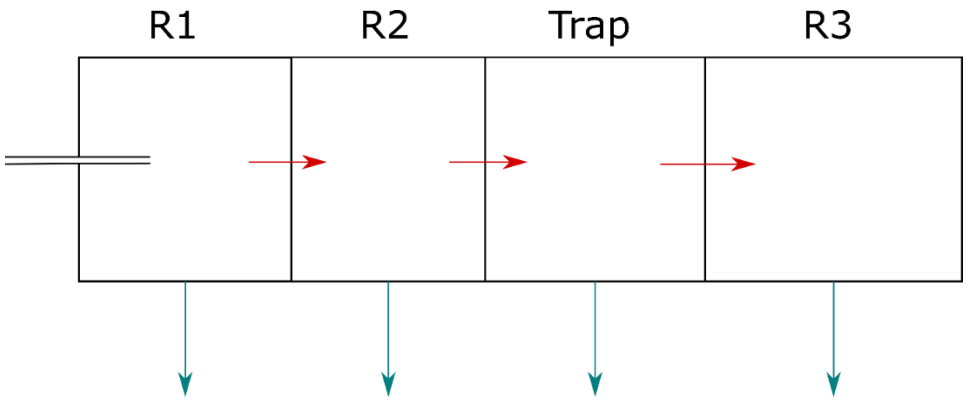

Figure 2.22 Schematic representation of the vacuum system under review. Throughput between chambers is represented by horizontal red arrows, while the throughput to the pumps is in teal. Chamber labels will be consistent with the text.

Flow into the first vacuum region through the capillary is at a high enough pressure that motion of gas through it can be considered to be flow rather than the passage of individual molecules. This is known as the viscous flow regime. Flow in this regime is categorised into two major forms, with a transition region between them. These are laminar and turbulent flow. For this calculation, laminar flow will be assumed, as calculating the exact shapes of chaotic turbulent flow is well beyond

the scope and interest of this thesis. For laminar flow of air through a pipe, the conductance, C_{pipe} is:

$$C_{pipe} = 180 \times \left(\frac{d^4}{L} \right) \times \left(\bar{P} \right) , \tag{2.5}$$

where *d* and *L* are the diameter and length of the pipe in cm and $\bar{P}$ is the average of the pressures either end of the pipe in Torr.[29] The gas throughput, Q, into the chamber can then be established as:

$$Q = C \times \Delta P , \tag{2.6}$$

with ΔP as the difference in pressure across the connection. Finally, pumps are usually measured in a pumping speed of volume per second, *S*, which is given by:

$$S = Q / P , \tag{2.7}$$

where *P* is the pressure of the chamber that the pump is connected to.

Knowing the pump and the dimensions of the capillary to be connected to R1 allows the various equations to be solved. The pump previously selected is still appropriate, as a single stage mechanical pump (Oerlikon, Sogevac 100B) with a pumping speed of 87.5 $m^3\ hr^{-1}$ or 24.3 $L\ s^{-1}$. Under these conditions, the predicted pressure is 1.5 Torr.

The next region is difficult to estimate due to the pressure regime. Between the viscous flow regime where the mean free path of the molecules is very small, and the molecular flow regime where intermolecular collisions are rare, is a transition regime. While the flow and conductance are well-defined and easily computable in both viscous and molecular regimes, transition regime conductances have no easy solution. To establish the flow regime present requires the calculation of the dimensionless Knudsen number:

$$K_n = \frac{\lambda}{L} , \tag{2.8}$$

where *L* is the characteristic length and λ is the mean free path, given by:

$$\lambda = \frac{k_B T}{\sqrt{2}\pi P d_m} \ , \tag{2.9}$$

where d_m is the molecular diameter. Knudsen numbers below 0.01 are considered viscous, while values of 10 or more are considered molecular.[30] The intended pressure for R2 is $\sim 10^{-2}$ Torr. Establishing the mean free path in both R1 and R2 allows for the calculation of the Knudsen number either side of the pinhole, assuming an aperture on the order of millimetres. On the R1 side, $K_n \approx 10^{-1}$, while at 10^{-2} Torr, $K_n \approx 10^{0}$, putting the region firmly in the transition regime.

From this information it was judged that the pinhole should be considered as a short tube under the viscous regime. The conductance of a pipe in the molecular regime is of the form:[29]

$$C_{\text{pipe,mol}} \propto \frac{d^3}{L} \ . \tag{2.10}$$

When evaluated, the viscous pipe scenario gave the highest value of conductance, thus it was used as the worst-case scenario with the hope that the system would out-perform that. A pinhole of 2 mm diameter and 1 mm thickness was chosen, combined with the $250\ \text{l s}^{-1}$ turbomolecular pump (Oerlikon, TW250S) and $40\ \text{m}^3\ \text{hr}^{-1}$ backing pump (Oerlikon, D40B) that had previously been attached to the trap region. This gave an expected pressure of 1.5×10^{-2} Torr.

When calculating the expected pressure for the trap region it was decided to aim for a lower pressure than required, as it is relatively simple to raise the pressure slightly. Pressures and pinhole scale state that the system is into the molecular flow regime once inside the trap chamber, $K_n \approx 20$ but still around the transition regime from the entrance side, $K_n \approx 2$. Modelling the pinhole as a conical pipe in the molecular regime gave the largest value of conductance. This was used so that the real system may outperform it. The conductance of a pipe in the molecular regime for air is given by:[29]

$$C_{\text{pipe,mol}} = 12.1 \times \frac{d^3}{L} \ . \tag{2.11}$$

where both d and *L* are in cm. To account for the flared nature of the aperture, see Figure 2.14 or Figure 2.24 for a visual representation, a modified diameter was used: [31]

$$d = \sqrt[3]{\frac{2d_1^2 d_2^2}{(d_1 + d_2)}} \ , \tag{2.12}$$

with d_1 and d_2 being the diameters at either end of the tapered tube. The pinhole was chosen to be a diameter of 4 mm as a compromise between the ease of ion throughput and vacuum considerations. A new turbomolecular $300\ \text{l s}^{-1}$ pump was sourced (Edwards, nEXT 300D) and was added to the backing line of an existing $25\ \text{m}^3\ \text{hr}^{-1}$ backing pump (Oerlikon, D25B) that backed to turbomolecular pump in R3. Under these conditions the predicted pressure for the trap was 6×10^{-4} Torr.

For R3 the pump was already attached, and the decision was the compromise between ease of ion extraction and pressure in the TOF. The system is into the molecular flow regime so the conductance of an orifice, such that $L < d$ is:

$$C_{hole} = A \times \frac{\bar{c}}{4} \tag{2.13}$$

where A is the area of the orifice in cm^2 and $\bar{c}$ is the mean thermal velocity given by:

$$\bar{c} = \sqrt{\frac{8k_b T}{\pi m}} \tag{2.14}$$

where *m* is the molecular mass. This means that the conductance and thus gas load into the trap region is proportional to $\sqrt{T}$. Under the principle of worst-case scenario, the temperature was taken as 300 K.

The pump attached to the chamber is a $700\ \text{l s}^{-1}$ turbomolecular pump (Oerlikon Turbovac SL700). A 4 mm diameter pinhole gave an expected pressure of 1×10^{-6}

Torr. All of the above predicted pressures and experimentally measured pressures are shown in Table 2.3.

Table 2.3 Predicted and experimentally measured pressures in the new chambers.

Region	Expected Pressure /Torr	Experimental Pressure /Torr
R1	1.5	1.28
R2	1.5×10^{-2}	8×10^{-3}
Trap	6×10^{-4}	5×10^{-4}
R3	1×10^{-6}	4×10^{-7}

2.3.3. Final Design

A brief description of each of the vacuum regions will be presented here along with any design decisions not already covered in previous discussion. Exact mechanical drawings with measurements of parts can be found in the digital appendix.

Starting from the source, the interior of R1 looks much as shown in Figure 2.23. Ions are introduced to the first region through the previous capillary assembly. The chamber body is a standard LF100 4-way cross. The central axis has been extended by an aluminium spacing ring, labelled in Figure 2.23. This was to make the chamber length compatible with the PCBs used within the trap region. An exact understanding of the ion trajectories in this region currently eludes us, however it is clear that the dominant force controlling their movement is gas flow. Various different alternative ion conduits and arrangements have been investigated including small hexapoles and the expedient approach of placing the capillary end almost touching the entry to R2. Our best solution currently seems to be having wrapped the entire PCB arrangement in Kapton tape, and move the capillary to around the position shown in Figure 2.23. This gives the best signal, but appears to be entirely insensitive to the RF or DC applied across the region. As it appears to have little effect, the RF is currently disconnected from this region. Attempting to connect the RF directly to this region caused problems with arcing. While Paschen's

law is not a perfect description of this situation due to the inhomogeneous fields produced, the main conclusion is still valid – that until the molecular flow regime is reached, the breakdown voltage often decreases with pressure.[32]

The PCBs are retained along the central axis using rectangular recesses in both pinholes and this methodology is maintained for all subsequent regions. The pressure is measured using the previous digital Pirani gauge (InstruTech, CVM-211), mounted on the top flange.

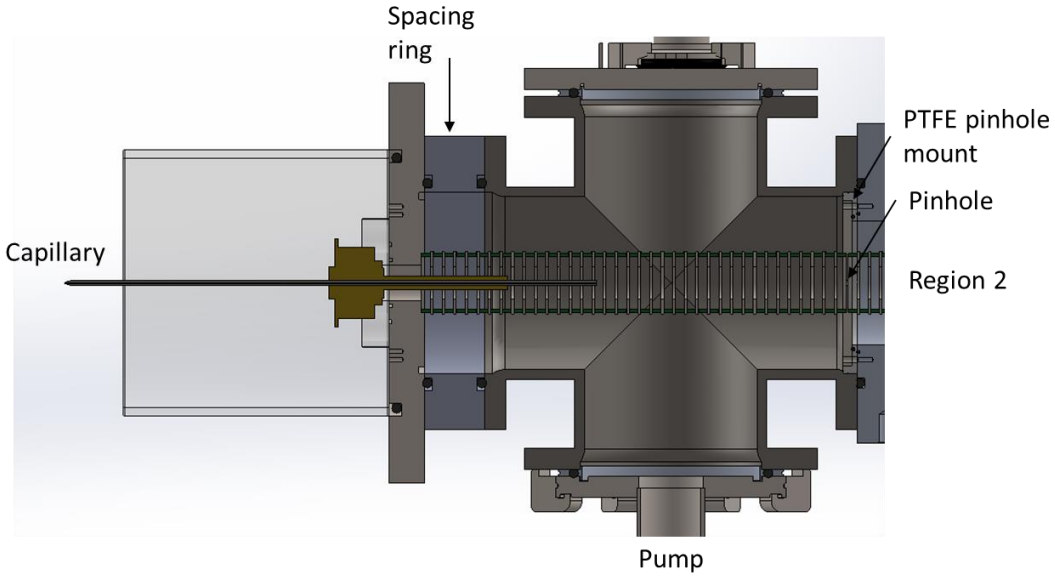

Figure 2.23 Cross-section view of R1. Parts are to scale with colour being representative of the material. Materials shown include stainless steel (4-way cross), aluminium (spacing), brass (capillary mount), Viton (O-rings) and glass fibre epoxy (PCBs). One alteration not shown, tape wrap, see text for details. Lower tube leads to the pump, with the start of R2 shown on the right. R1 is usually measured at a pressure of around 1.3 Torr.

The stainless-steel pinhole to R2 is mounted onto the chamber to R2 using M3 nylon bolts, whose holes can be seen. It is held within a PTFE mounting ring to electrically isolate it from the chamber, which is grounded. This is more clearly shown in Figure 2.24. The pinhole between the regions is flared such that the diameter is larger on the lower-vacuum side. This is difficult to see at this magnification.

R2 is housed in a custom designed and manufactured aluminium chamber. The chamber features 3 KF40 bulkhead attachments, which can be seen in Figure 2.24. The third of these, the one on the opposite face to the viewpoint, is currently in use as an extra gas feedthrough to allow for the flow of a small amount of helium into the trap region. The chamber also features a large viewport on the nearest side, more clearly shown in Figure 2.25.

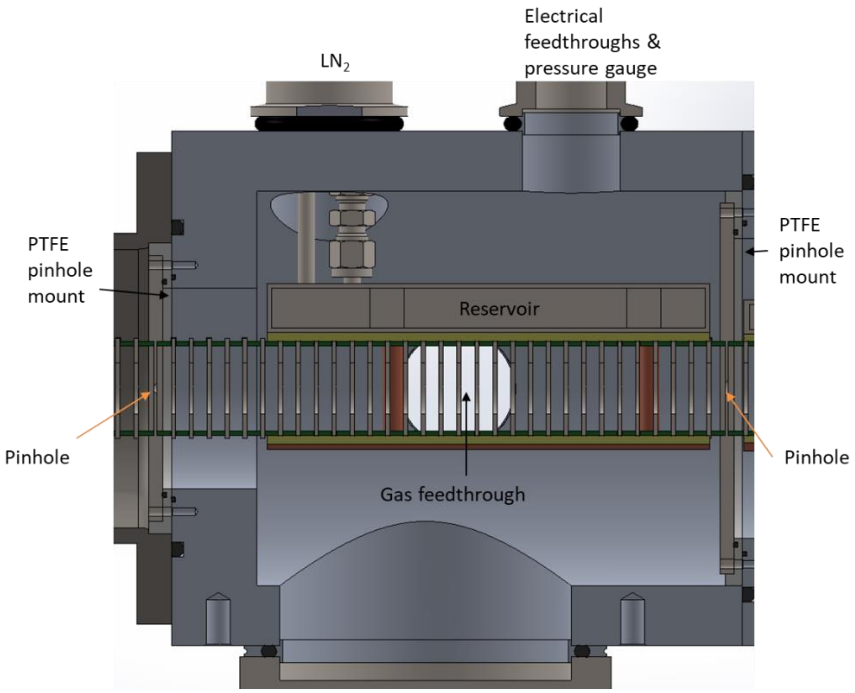

Figure 2.24 Region 2 of the spectrometer in cross section. Colour is representative of material, with dark grey being stainless steel, the main chamber being made of aluminium. Other materials shown are copper, PTFE and the gap-filling material above and below the boards.

Although it is not clear on this diagram, the connection containing the liquid nitrogen feedthrough is not a steel tube, but rather a set of edge-welded bellows. The travel on these allows for the tightening of the ferrule-based gas connections.

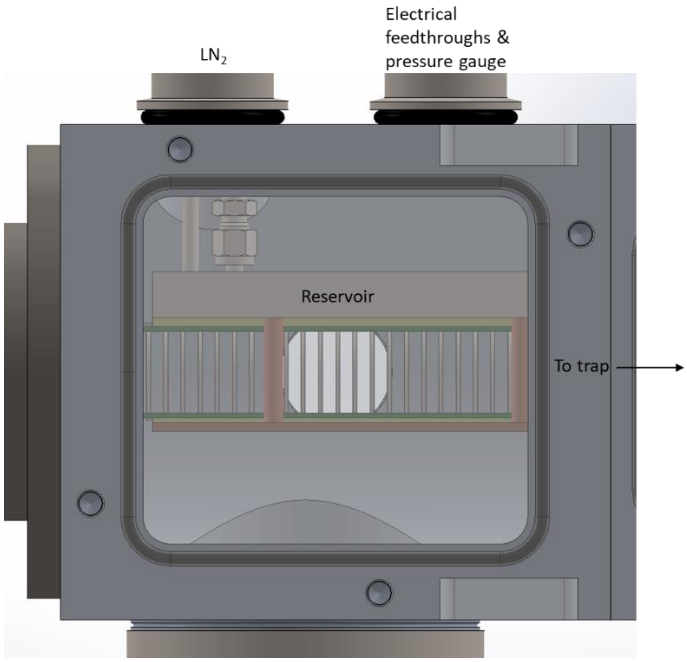

Figure 2.25 Region 2 of the spectrometer from an exterior perspective, more clearly showing the external viewports and the recesses for attaching to the trap region.

The pinhole to the trap region is again housed within a PTFE housing that is a tight tolerance fit to the inside of the R2 chamber. The pinhole is held in place with M3 nylon bolts so a potential can be applied. The pressure is measured using the previous system, a thermocouple gauge (Kurt J. Lesker, KJL-6000), able to measure to 10^{-3} Torr.

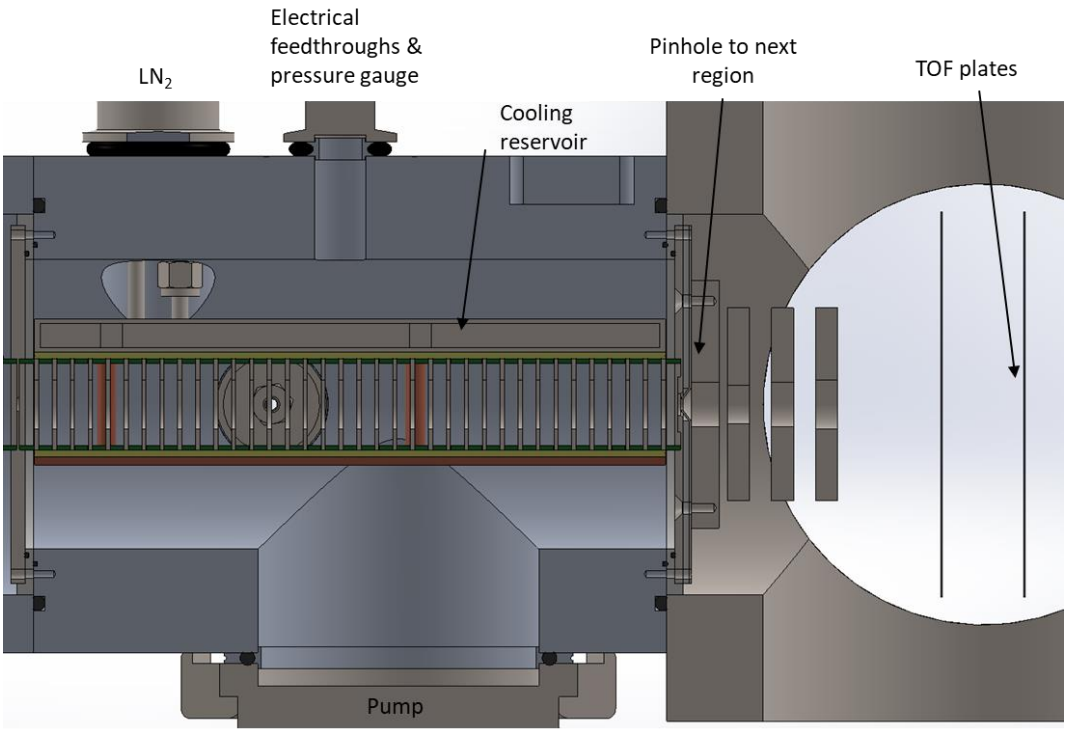

Figure 2.26 Cross-section view of the trap region of the spectrometer showing the extraction optics. All parts are to scale with colour being representative of the material. Also shown is the interior of region 3 and the start of the TOF optics. These were all drawn to ensure sufficient access for the final assembly.

The chamber for the trap region was again a custom design and incorporates 3 KF40 attachments along with a large front viewport in a similar style to that of R2. Pressure is measured using a convection-enhanced Pirani gauge (Kurt J. Lesker, KJL275808LL) capable of reading down to 1×10^{-4} Torr.

The cooling reservoirs for both regions were designed to have as large an internal volume as possible, while allowing for assembly.

The trap extraction optics require a little more explanation. The pinhole was constructed from 4 separate components, seen more clearly in Figure 2.27. The first of these, (A), contains the rectangular recess to hold the PCBs and also incorporates a slight projection to aid with the lensing action described in section 2.2.3. This part was always held at a negative potential, repulsive to anions. The second part, (B), comprised a PTFE disc to electrically isolate the front of the pinhole system from the back. The third, (C), and fourth, (D), parts are seen as one in the SIMION simulations, such as in Figure 2.16, but had to be split into two parts for

manufacturing reasons. The third part consists of a flat sheet of 1 mm stainless steel with the cone-sided hole through it. This is adjacent to a much thicker ring, (D), to form both the final part of that extraction system and physical support. The pinhole is held together using countersunk head screws, whose holes are clearly visible in Figure 2.27. The thin steel sheet part, (C), was very delicate and benefitted from being clamped between the two thicker pieces.

The fourth part, (D), also housed the mounting rods for the subsequent einzel lens. These were constructed out of PEEK for electrical insulation between both the different components of the einzel lens and the support. The whole pinhole system was then again mounted within a PTFE housing labelled below.

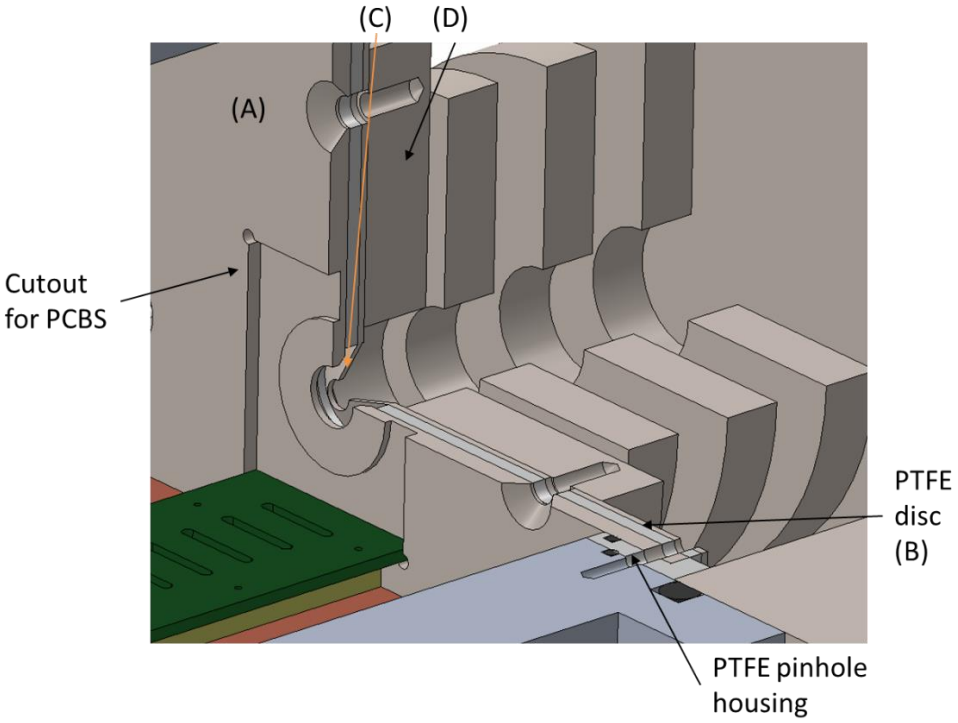

Figure 2.27 Three-quarter cut view of the trap pinhole and extraction optics, with the electrodes, upper board and liquid nitrogen reservoir removed for clarity. See text for a full description.

2.3.4. Proof of Concept

Given the amount of trepidation associated with pouring liquid nitrogen into a vacuum chamber, the machine was initially assembled without the cooling apparatus. Given the number of variables present in the control system, it was expected to take some time to initially set up the electronics to within an operational scheme.

For a discussion of the electronic controls, which reference will be made to in section 3.2.1, a diagram is necessary, Figure 2.28. The DC control system controls the potentials for the repulsive end wall of the trap, the extraction voltage, the potential across each resistor chain, and the potential between the final or first electrodes and the pinhole between them. This consists of 11 separate controls that are labelled as on the diagram.

Each of the various points of control shown in Figure 2.28 can be changed without affecting the magnitude of the any of the others. Due to the stacked nature of the system, changing the trap depth along the cylindrical axis by increasing the voltage applied to point 2 cannot cause point 2 to ever be higher in potential energy than point 3. Point 1 is an offset control to the first electrode – this gives another control over the kinetic energy of the ions upon extraction.

The RF decoupling circuits shown in Figure 2.18 are mounted to the feedthroughs within a small metal box for shielding. This is then connected to the DC supplies with the voltage stacking being accomplished using short wires from negative to positive output on adjacent supplies.

Due to a slight quirk of the design, the voltages between pinholes and guides are not solely controlled by the DC supplies attached to points 4, 5, 7, and 8. This is due to a small offset present from the decoupling circuit's bias resistors, labelled R6 and R9 in Figure 2.18. This causes the pinholes to be inherently offset from the nearest adjacent electrode by a small amount, $< 5\%$ of the voltage applied across the guide, points 2, 3, 6, and 9.

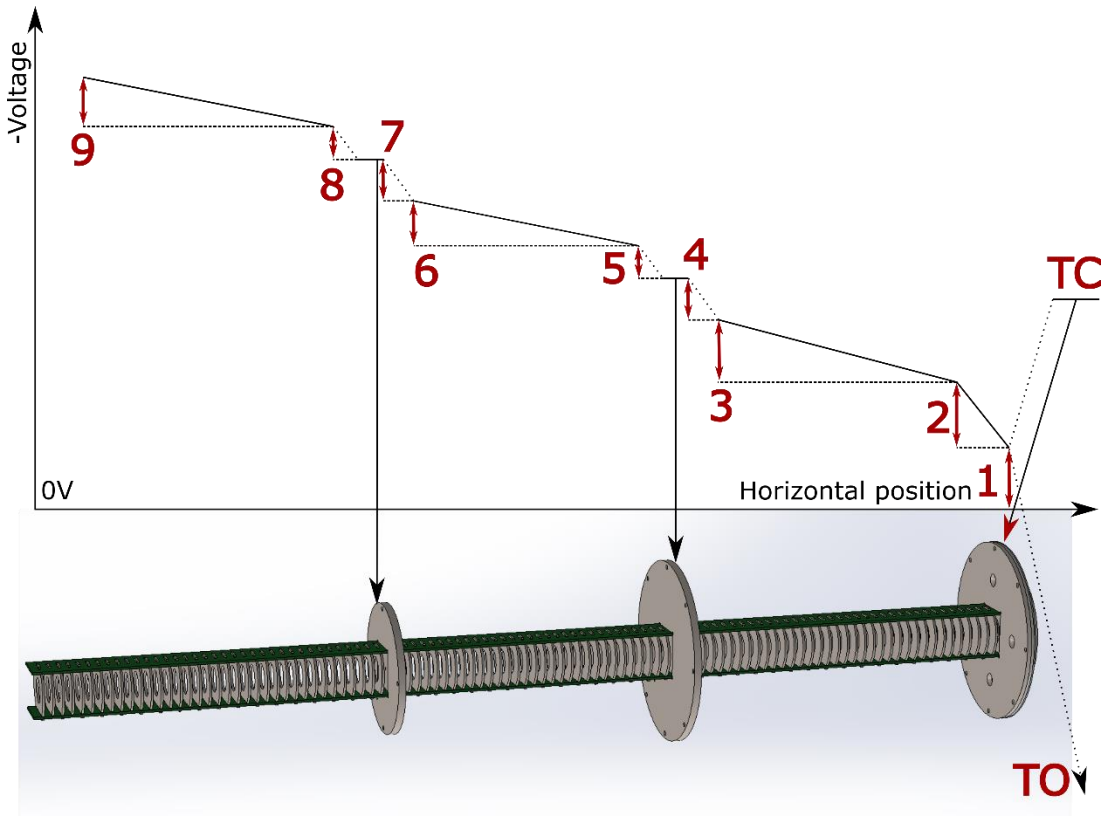

Figure 2.28 Schematic representation of the DC electrical controls for the new ion guides and trap. Red arrows define the two points of reference for the potentials, so the system stacks. Solid black lines show regions of continuous potential with dashed lines showing discontinuities. The potentials labelled TC and TO stand for Trap Closed and Trap Open respectively. The vertical axis is not to scale. Trap Open would be much further off this scale.

Understanding the full phase space of these controls will take some time. However, some interesting trends have already started to become clear. Point 4 has become relatively unused, and any voltage applied to it, above that explained above, diminishes the signal level.

When discussing the first vacuum region in section 2.3.3, the point was made that the ion signal seems to be relatively unaffected by changing the DC across the first guide, control 9. Contrastingly, controls 7 and 8 show a considerable effect on the ions and some of this will be discussed in section 3.2.1 and future work.

Since the original design work, the einzel lens immediately out of the trap has changed, not in physical shape but due to the potentials applied to it. Under the SIMION simulation, all rings had a positive potential, with the middle ring being the major focussing element. A different regime has been found by using the first ring

as the focussing element and grounding the final two. This is remarkably successful in terms of ion signal and has a smaller effect on the TOF optics between different chemical species.

It is very difficult to quantifiably compare the ion signal between the old and new designs, as the equipment has changed by getting older. Qualitatively, the signal level at 10 Hz for the nanosecond laser seems considerably increased, by about an order of magnitude. Furthermore, when attempting to run at higher repetition rates, the photoelectron signal has been noticed to increase up to at least 200 Hz which is again an improvement on the original. It is this author's firm belief that considerably more can still be achieved by further exploring all of the possible controls of the system.

While this lack of quantifiable data to compare the magnitude of the ion signal is frustrating, quantifiable data on the problem of cooling has been achieved. This was done by comparing the hot bands on chlorite, ClO_2^- , as previously done by the Wang group as shown in Figure 2.29.[33]

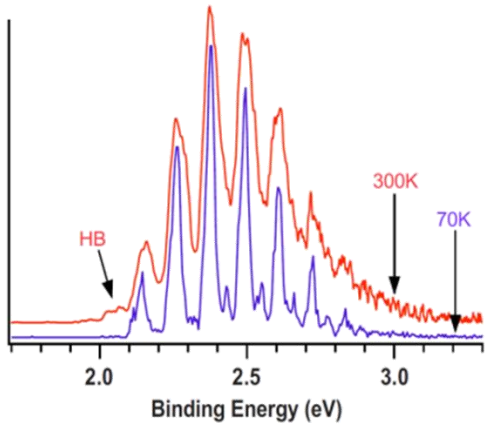

Figure 2.29 Photoelectron spectrum of chlorite taken at 355 nm (3.5 eV) at both 300 K and 70 K. The hot bands, transitions starting from vibrational level above the ground state, are labelled as HB. Reproduced from Ref. 33. Copyright 2008, American Institute of Physics.

The conditions for achieving cooling appear to be unstable and considerable work is required before the system is ready to be used to investigate the cryogenic dynamics that were originally planned. Upon starting the cooling process, with no other changes, signal levels vary considerably, initially increasing by almost a factor

of 2, then a precipitous fall to signal loss. Upon changing the electrical potentials to regain signal, hot bands are still visible. One cooled dataset has been achieved, with added helium flowed across the pinhole between R2 and trap, and the softest trapping potentials that could be suffered. This is shown relative to a dataset taken with no cooling or other alteration.

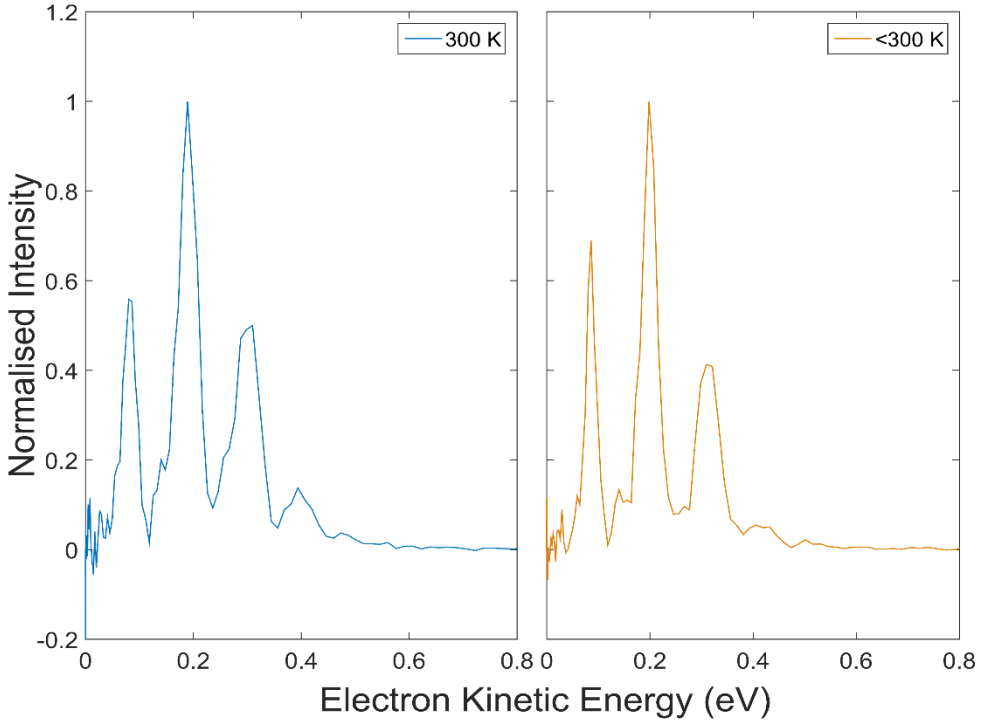

Figure 2.30 Comparison of ClO_2^- data taken with no cooling applied, blue, and under cooling, orange. Spectra were taken at 500 nm (2.47 eV) The hot bands are expected to be at around 0.4 eV. The cooled band clearly shows a reduction in that peak.

While this small success shows promise, it also highlights the quantity of work still to do to make this cooling ready for an actual experiment. The extra variables of pressure, and gas flow through/into the chambers show a huge importance to the data set and fully exploring all these is a challenge for the future of the lab.

2.4. References

1 C. West, PhD thesis, Durham University, 2016.
2 D. Horke, PhD thesis, Durham University, 2012.
3 G. Roberts, PhD thesis, Durham University, 2010.
4 J. Lecointre, G. M. Roberts, D. A. Horke and J. R. R. Verlet, *J. Phys. Chem. A*, 2010, **114**, 11216–11224.
5 J. B. Fenn, *Angew. Chem. Int. Ed.*, 2003, **42**, 3871–3894.
6 C. Ho, C. Lam, M. Chan, R. Cheung, L. Law, L. Lit, K. Ng, M. Suen and H. Tai, *Clin. Biochem. Rev.*, 2003, **24**, 3–12.
7 W. C. Wiley and I. H. McLaren, *Rev. Sci. Instrum.*, 1955, **26**, 1150–1157.
8 R. G. Wilson, *J. Appl. Phys.*, 1966, **37**, 2261–2267.
9 D. A. Horke, G. M. Roberts, J. Lecointre and J. R. R. Verlet, *Rev. Sci. Instrum.*, 2012, **83**, 063101.
10 A. T. J. B. Eppink and D. H. Parker, *Rev. Sci. Instrum.*, 1997, **68**, 3477–3484.
11 G. M. Roberts, J. L. Nixon, J. Lecointre, E. Wrede and J. R. R. Verlet, *Rev. Sci. Instrum.*, 2009, **80**, 053104.
12 R. J. Peláez, C. Blondel, C. Delsart and C. Drag, *J. Phys. B At. Mol. Opt. Phys.*, 2009, **42**, 125001.
13 E. Luc-Koenig, C. Morillon and J. Vergès, *Phys. Scr.*, 1975, **12**, 199.
14 Tunable Lasers Sources - Horizon OPO-Continuum, http://www.quantron.com/index.php?option=com_content&view=article&id=653&Itemid=582#liintroTab, (accessed 29 July 2017).
15 D. Gerlich, in *Advances in Chemical Physics*, eds. C.-Y. Ng, M. Baer, I. Prigogine and S. A. Rice, John Wiley & Sons, Inc., 2007, pp. 1–176.
16 A. S. Chatterley, C. W. West, G. M. Roberts, V. G. Stavros and J. R. R. Verlet, *J. Phys. Chem. Lett.*, 2014, **5**, 843–848.
17 J. Gidden and M. T. Bowers, *Eur. Phys. J. D*, 2002, **20**, 409–419.
18 J. Gidden, J. E. Bushnell and M. T. Bowers, *J. Am. Chem. Soc.*, 2001, **123**, 5610–5611.
19 D. A. Horke, A. S. Chatterley and J. R. R. Verlet, *J. Phys. Chem. Lett.*, 2012, **3**, 834–838.
20 S. Guan and A. G. Marshall, *J. Am. Soc. Mass Spectrom.*, 1996, **7**, 101–106.
21 Wolfgang Paul - Nobel Lecture: Electromagnetic Traps for Charged and Neutral Particles, https://www.nobelprize.org/nobel_prizes/physics/laureates/1989/paul-lecture.html, (accessed 30 July 2017).
22 D. A. Dahl, *Int. J. Mass Spectrom.*, 2000, **200**, 3–25.
23 S. Guan and A. G. Marshall, *J. Am. Soc. Mass Spectrom.*, 1994, **5**, 64–71.
24 M. D. Morse, *Exp. Methods Phys. Sci.*, 1996, **29**, 21–47.
25 D. Gerlich and G. Borodi, *Faraday Discuss.*, 2009, **142**, 57–72.
26 F. Teyssandier and D. Prêle, in *Ninth International Workshop on Low Temperature Electronics - WOLTE9*, Guaruja, Brésil, 2010.
27 R. Bara-Maillet, M. Goryachev, D. L. Creedon, J. M. L. Floch and M. E. Tobar, *IEEE Trans. Instrum. Meas.*, 2014, **63**, 628–632.
28 E. D. Marquardt, J. P. Le and R. Radebaugh, in *Cryocoolers 11*, ed. R. G. R. Jr, Springer US, 2002, pp. 681–687.

29 J. H. Moore, C. Davis, M. Coplan and S. Greer, *Building Scientific Apparatus: A Practical Guide to Design and Construction*, Westview Press Inc, Boulder, Colo. : Cambridge, Mass, 3rd Revised edition edition., 2002.
30 S. Roy, R. Raju, H. F. Chuang, B. A. Cruden and M. Meyyappan, *J. Appl. Phys.*, 2003, **93**, 4870–4879.
31 S. Zheng, *Superconducting Super Collider Lab-GEM-Technical Note 93-382*.
32 N. Spyrou, R. Peyrous, N. Soulem and B. Held, *J. Phys. Appl. Phys.*, 1995, **28**, 701.
33 X.-B. Wang and L.-S. Wang, *Rev. Sci. Instrum.*, 2008, **79**, 073108.

3. Excited States of the Anthracenyl Anion

This chapter details the study of the excited states of one isomer of deprotonated anthracene. This was done to gain insight into possible electron attachment mechanisms for anion formation in interstellar space. A novel ion production technique was developed for the experiment and resulted in good data being taken of one of the isomers of the deprotonated polyaromatic hydrocarbon (PAH). The carboxylic acids used were also briefly studied.

This chapter is based upon "Resonances of the Anthracenyl Anion Probed by Frequency-Resolved Photoelectron Imaging of Collision-Induced Dissociated Anthracene Carboxylic Acid.", L. H. Stanley, C. S. Anstöter and J. R. R. Verlet, *Chem. Sci.*, 2017, **8**, 3054–3061.

3.1. Introduction

The presence of polyaromatic hydrocarbons (PAHs) can be seen across many varied chemical environments such as part of the incredibly complex structure of coal[1] or nucleation points in soot formation of particular interest to atmospheric chemists.[2,3] The possibility of their contribution to anthropogenic pollution, current popular feelings on climate change notwithstanding, is worth considering due to their carcinogenic and mutagenic nature.[4,5] PAHs have also been considered as the basis for new organic electronics systems, such as OLEDs, photovoltaic cells, organic field-effect transistors and novel battery cathodes.[6–9] When designing these devices, the fundamentals of the electronic and redox properties of the base PAH must be known and considered. Looking further afield than our terrestrial chemistry, gas-phase PAHs are expected to make up a considerable quantity of the interstellar medium due to their considerable presence in the mid-IR spectra of star forming regions of space.[10–13] Ionised interstellar PAHs are also predicted to be in relative abundance due to the ratio of certain bending mode peaks. Both cations, such as C_{60}^{+}, and anions are expected.[14] It is the anions with which this lab is more interested.

It is in regions of space with increased electron density that anionic molecules are expected in the interstellar medium. The first few discovered were linear hydrocarbon-based anions, such as C_4H^-, C_6H^-, and C_8H^-, and were observed at the order of a few percent abundance relative to their neutral forms.[15–17] PAH anions have yet to be individually assigned in the spectra but it is considered that they may be abundant enough to be the principal negative charge carrier in some regions.[11,18–20] The mechanism of anion formation in interstellar space is somewhat unclear. Low energy electron attachment via a non-valence dipole-bound state has been the most commonly invoked mechanism.[21,22] A dipole bound state requires a dipole moment greater than ~ 2.5 Debye[23], thus most neutral PAHs do not have the requisite dipole moment for this mechanism.

An alternative mechanism involves electron attachment via valence excited states of the anion embedded in the continuum. Although the most likely outcome of electron attachment into such a resonance is rapid autodetachment, excited state relaxation processes such as internal conversion through conical intersections can compete and may cause the eventual production of the anionic ground state.[24–27] Valence resonances are particularly prevalent in highly π-conjugated systems.[23,28,29] Electron impact studies have confirmed that such resonance-mediated decay processes occur[28] and ground state anions of tetracene ($C_{18}H_{12}$) and pentacene ($C_{22}H_{14}$) have been observed following electron impact energies of ~ 3 eV.[30]

All of the molecular anions that have had their existence confirmed in the interstellar medium are closed-shell[11,16,17,31–36] and thus the PAH anions predicted to exist in interstellar space are also likely to be closed-shell. This would favour deprotonated PAHs as likely candidates rather than the radical anions.[37] In the last few years this lab has developed anion photoelectron spectroscopy as a probe of resonances in a range of radical[25,26,38–40] and closed shell anions,[41–43] including the tetracenyl anion, $C_{18}H_{11}^-$.[24] Following excitation to an anionic excited state resonance, $C_{18}H_{11}^-$ showed a preference for internal conversion back to the ground state of the anion rather than autodetachment to the neutral. If a low-energy electron approaches a tetracene molecule, so long as the kinetic energy of that electron matches that of an anionic excited state, then the electron can be bound to form the ground state of the anion, despite the inherently unbound nature of the of the above-threshold resonance. These dynamics are enabled by a large number of π^* resonances, thus a prediction can be made that similar processes may occur in larger polyacenes than tetracene. Contrastingly, the question could be asked of how few states and by extension, how small a polyacene is required for efficient recovery of the anionic ground state after excitation to a resonance?

Given that tetracene is a system of four linearly fused benzene rings, the next step would be to investigate the relaxation dynamics of three benzene rings, anthracene. The possible deprotonation sites of neutral anthracene to form the anthracenyl radical are shown in Figure 3.1(a).

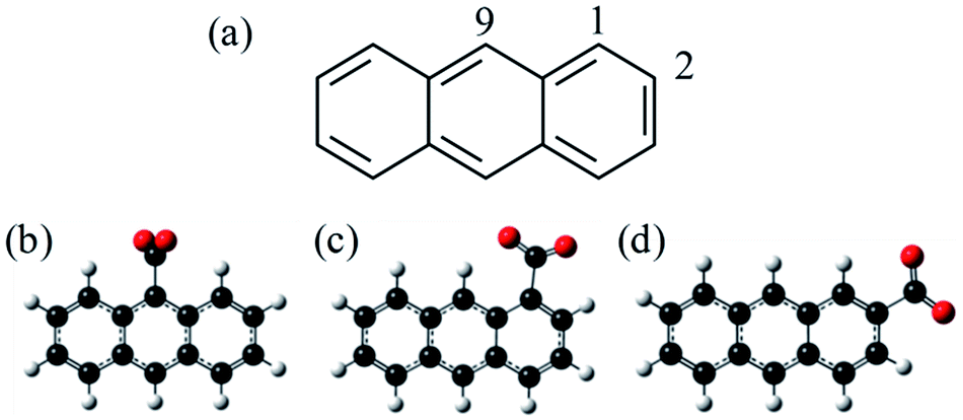

Figure 3.1 (a) Skeletal structure of neutral anthracene. (b)-(d) The three possible isomers of anthracene carboxylic acid, numbered according to the labels in (a).

3.2. Experiment

3.2.1. Practical Considerations

Frequency resolved data were taken using the nanosecond laser system described in section 2.1.2. This provided laser pulses of ~ 6 ns duration at photon energies spanning 300 nm (4.1 eV) to 590 nm (2.10 eV).

The study on the tetracenyl anion, $C_{18}H_{11}^-$, was performed using a solution of the neutral polyacene in toluene. This suffered from low deprotonated ion yield and overall measured ion signal instability. Performing electrospray directly with the neutral molecule allows for no selectivity as to the position of the localised charge on the molecule. The most likely outcome is of all isomers being formed with a preference for the more stable species.

Attempting a similar methodology upon neutral anthracene resulted in an impasse due to insufficient signal levels. Thus, an alternative anionic generation technique was required.

Within the mass-spectroscopy community, two methods have been developed to generate location specific carbanions.[44,45] The first relies on the reaction of a fluoride anion with a molecule with a trimethylsilyl group attached.[46,47] This works because the formation of the Si-F bond is highly selective, thus allowing for regioselective anion formation.[46] This was recently used by the Neumark group to study the neutral ground and first excited states of the three isomers n-$C_{14}H_9$ (with n = 1, 2, 9). Their methodology was by slow-electron velocity map imaging (SEVI) of $C_{14}H_9^-$ generated through molecular beam co-expansion of NF_3 and n-(trimethylsilyl)-anthracene in He carrier gas in the presence of excess electrons.[48] An alternative method of achieving regioselective anions is decarboxylation of a deprotonated carboxylic acid anion through collision induced dissociation (CID) with a backing gas.[49] This latter approach appealed due to a similar approach having been successful during a visit from Dr Berwyck Poad (University of Wollongong). During this visit, various molecules were studied following the CID and decarboxylation of a parent molecule. CID was achieved within the machine by increasing one of the DC control voltages early in the system. In particular, it was a significant increase in voltage point 7 (VP7), as labelled in Section 2.3.4 (the differential between the pinhole at the culmination of region 1 and the starting electrode of region 2) that appeared to generate the fragmentation products that he had seen previously under CID conditions. This methodology was selected and thus required solutions of the three isomeric forms of anthracene carboxylic acid as seen in Figure 3.1. In other respects, the experiment was performed as detailed in Chapter 2. The three isomers of n-$C_{14}H_9-CO_2H$ (procured from Tokyo Chemical Industry and used without further purification), were made up into an approximately 1 mM solution in methanol for electrospray ionisation.

Under normal operation, the potential difference applied between the pinhole and the first electrode of region 2, (VP7) would be between 0 and –2 V. This would be sufficient to guide the ions through the pinhole as seen by the ion signal. Under CID conditions, the potential difference was increased to up to −62 V.

Increasing the voltage applied to VP7 from 0 resulted in the formation of a fragment peak at *m*/*z* 44 below that of the parent ion, which would correspond to the mass loss of a CO_2 group. The relative quantity of the fragment could be increased by increasing the potential, which corresponds to the ions being accelerated more vigorously through the background gas into region 2. Under more conventional CID conditions the collisions of an organic carboxylic acid generally remove the CO_2 group to produce the deprotonated carbanion.[44,45] Under low-pressure conditions and "soft" CID, this negative charge generally remains localised in the location where the CO_2 was removed. However, in our setup, CID occurs in a region with a few orders of magnitude higher pressure than that of a typical CID mass-spectrometric experiment[44,50] and the timescales in our experiment are also very different (with the time from CID to photoelectron spectroscopy being several milliseconds).

However, despite initial apparent success, a difficulty was encountered. The standard procedure is to alter the electrical controls of the system to maximise the ion signal present in the time-of-flight spectrum before interrogating the ion packet with the laser. Performing this process upon the fragment peak gave a bright strong photoelectron signal that caused initial joy at the simplicity of the experimental method. However, comparison with the photoelectron spectra from the Neumark lab did not agree.[48] While the resolutions and aims of the experiments were different, it was expected to see agreement in the electron affinity and energetic positions of the neutral radical excited states. They bore little similarity.

It was concluded that under conditions of maximum ion signal, some other fragment or reaction was taking place. The exact nature of this reaction and fragment are still somewhat mysterious, however, it was noticed that the introduction of dry argon around the entrance capillary to region 1 drastically reduced the quantity of this signal present in the photoelectron image. Thus, it could be the result of some reactive fragment interacting with either water or oxygen from the air.

Having reached the unwelcome conclusion that a considerable amount of data was of an unknown, and in the context of the experiment, unwanted fragment, effort was taken to find a regime where the correct fragment could be achieved.

A regime was found to produce the anthracenyl anion, with mixed success. The lowest energy isomer, 9-$C_{14}H_9^-$, could be produced in sufficient quantity to take data under reduced VP7 voltage and a flow of argon into the chamber by application to the volume near the entrance capillary. While this would inherently generate the anion in a vibrationally excited, or hot, state, it is expected to have thermalized before extraction into the TOF. Attempts were made to find a regime where the other acid isomers could be used to exclusively produce the corresponding regiospecific anthracenyl anion but with no success. It was possible to produce some of the specific anion, but there was always significant contamination of 9-$C_{14}H_9^-$, despite there being none present in the solution.

Although in this study only a single isomer could be formed exclusively, the use of CID in forming the decarboxylated fragment anion is appealing for future work because it relies on electrosprayed anions for which there is essentially no size or volatility limit of the precursor anion. For larger PAHs, the vapour pressure rapidly reduces. For example, perylene has a vapour pressure of $\sim 4\times10^{-2}$ Pa at 400 K[51] and needs to be heated to very high temperatures for molecular beam studies. In contrast, electrospray ionisation of the perylene carboxylic acid is readily achieved.

3.2.2. Computational Methods

Density functional theory (DFT) calculations were performed by Cate Anstöter using the Gaussian 09 computational package[52] and the B3LYP functional with the 6-31+G** basis set, which has been shown to perform well for anionic PAHs.[48] The geometries of 1-, 2- and 9-$C_{14}H_9^-$ and their corresponding radical neutral species were optimized, and were confirmed to represent the geometric minima through vibrational frequency analysis. All of the geometries of n-$C_{14}H_9^-$ were confirmed to have planar minimum energy structures, in agreement with the previous

literature.[48,53,54] The calculated energetics have been corrected for zero-point energy. Calculations using time-dependent (TD) DFT employing the Tamm–Dancoff approximation[55] provided energetics and information about the character of both the anionic and neutral excited states accessed experimentally for 9-$C_{14}H_9^-$ which has C_{2v} symmetry. Additional ab initio calculations were carried out to predict the photoelectron angular distributions using the coupled-cluster equations of motion (EOM) formalism[56] and employing the QChem 4.4 package.[57] Specifically, EOM-IP-CCSD calculations (using the same basis set as before) were used to determine the Dyson orbital with the anion ground state as the initial reference wavefunction, Ψ^N, and the neutral ground state as the final wavefunction, Ψ^{N-1}.[58,59] The photoelectron angular distribution for this direct detachment channel was modelled using the ezDyson program (version 3.2) developed by Krylov and coworkers.[60,61]

3.3. Results and Discussion

3.3.1. Anthracene Carboxylic Acids

The photoelectron spectra of the three isomeric forms of *n*-$C_{14}H_9-CO_2^-$ taken at a photon energy of 4.13 eV (300 nm) using the nanosecond laser system are shown in Figure 3.2. Only the lowest electron affinity isomer, the 9-$C_{14}H_9-CO_2^-$, shows a clear direct detachment peak. At very low electron kinetic energy (eKE), the rising photoelectron feature is indicative of an indirect and delayed emission process. This is seen more clearly for the two other isomers, 1-$C_{14}H_9-CO_2^-$ and 2-$C_{14}H_9-CO_2^-$, where the direct detachment feature is partially obscured by this delayed emission. Despite this, the high eKE edge of the direct detachment feature of each of the three isomers allows for an approximate adiabatic detachment energy (ADE) measurement. These were determined to be 3.7(2), 3.8(2) and 3.5(1) eV for *n* = 1, 2,

and 9, respectively. Calculated ADE values were 3.69, 3.97 and 3.34 eV for *n* = 1, 2, and 9, respectively. $h\nu = 4.13$ eV

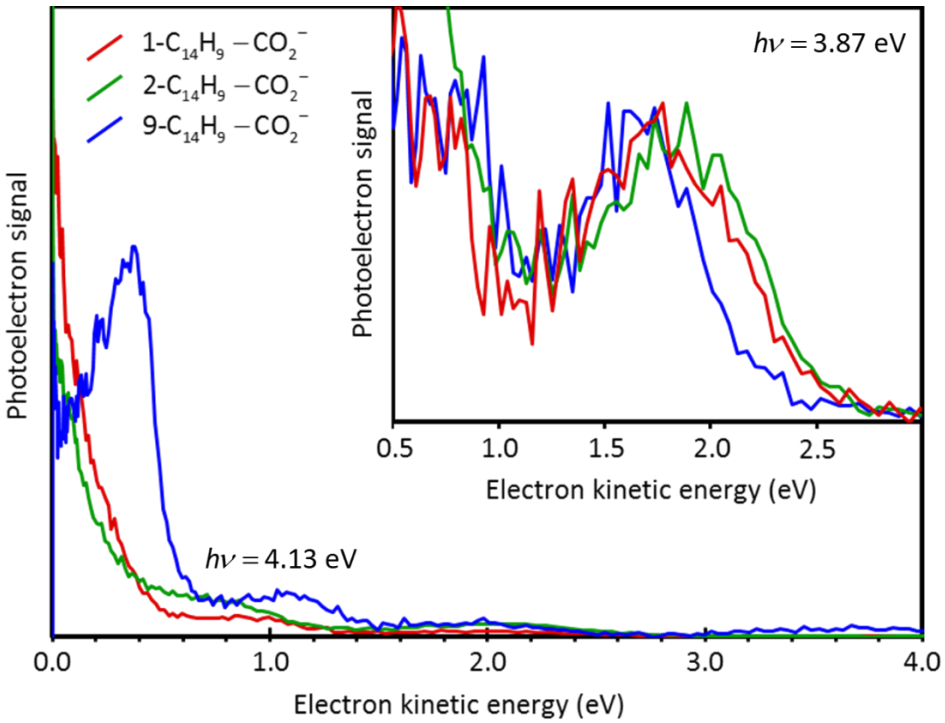

Figure 3.2 (Main) Photoelectron spectra of the three anthracene carboxylic acids at 300 nm (4.13 eV) (Inset) Vertically magnified section of photoelectron spectra of the same species at 320 nm (3.87 eV). The feature shown is present in the main part of the figure but is particularly obvious in the 320 nm spectra.

The fact that there is an indirect emission channel indicates that resonances in *n*-$C_{14}H_9 - CO_2^-$ are excited at 4.13 eV. At higher eKE, additional features can be seen in the photoelectron spectra. For all three isomers, there is a peak around eKE ~ 2 eV in addition to a shoulder just beyond the direct detachment. This region is shown more clearly in the inset of Figure 3.2, where 3.87 eV (320 nm) light was used to attain a higher signal-to-noise ratio. By extrapolation of the high-eKE edge of this higher-eKE detachment feature for each isomer, we obtain ADE values of 1.3(1), 1.3(1), and 1.6(1) eV for *n* = 1, 2, and 9, respectively. These are in reasonable agreement with the ADE values determined by the Neumark group for the n-$C_{14}H_9^-$ ions using SEVI (1.5436(2), 1.4671(2), and 1.7155(2) eV for the *n* = 1, 2, and 9, respectively) and with our calculated values of 1.50, 1.44 and 1.66 eV for *n* = 1, 2, and 9, respectively. Hence, the photoelectron peaks at eKE ~ 2 eV appear to arise

from the decarboxylated fragment n-$C_{14}H_9^-$ that has been formed by photodissociation during the ~ 6 ns laser pulse. A similar photo-induced decarboxylation has been observed by this lab in a linear polyene carboxylic acid anion.[43] The fact that the ADEs measured here are lower than those reported by the Neumark group is likely a result of hot-bands because the fragment is made with a large amount of internal energy; our calculations indicate that 2.26 eV is required to lose the CO_2 group, leaving ~ 2 eV of excess energy in the fragment anion.

The shoulder to the direct detachment from the fragment can be assigned to the first neutral excited state, which lies 1.205(6) eV[48] higher in energy than the neutral ground state for 9-$C_{14}H_9^-$, and which will be discussed in detail below when considering the frequency-resolved photoelectron imaging of 9-$C_{14}H_9^-$.

3.3.2. 9-Anthracene Charge-Localised Anion

9-$C_{14}H_9^-$ was produced by CID of 9-$C_{14}H_9-CO_2^-$ and its frequency-resolved photoelectron spectra are shown in Figure 3.3. It is composed of 21 photoelectron spectra taken at 0.1 eV intervals using the nanosecond laser system. Each spectrum has been normalised so that the highest energy peak has a unit maximum intensity. As the photon energy is increased, the eKE of the highest energy peak also increases linearly indicating that this is a direct detachment feature. Extrapolation of the high eKE edge yields ADE = 1.7(1) eV, which is in agreement with the value of 1.7155(2) eV determined by Neumark and coworkers.[48] This is also in agreement with the 9-$C_{14}H_9^-$ formed by photodissociation of the carboxylate described in the previous section. Given the difficulties encountered in making solely this product, as detailed in section 3.2.1, this was satisfactory proof of the formation of the intended product of CID.

At around $h\nu \approx 3.0$ eV, a second detachment channel opens up which also leads to a peak that increases linearly with photon energy. This feature can be assigned to

direct detachment to the first excited state of the 9-$C_{14}H_9$ neutral radical. The energy gap between these values from our measurements is 1.2(1) eV, which is in agreement with the gap of 1.205(6) eV determined by Neumark and coworkers and with the photodissociation product mentioned in the previous section.[48]

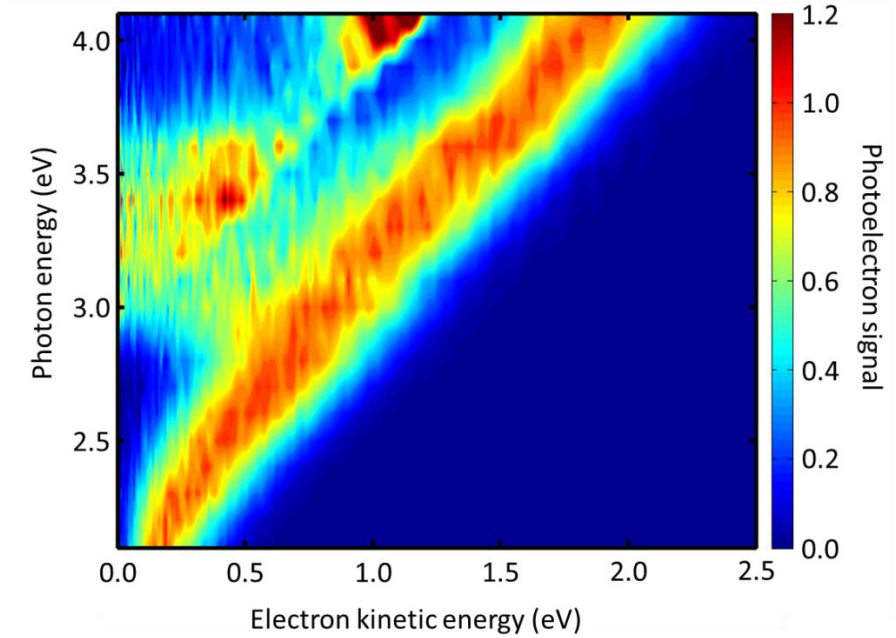

Figure 3.3 Frequency-resolved spectra of 9-$C_{14}H_9^-$ normalised to the intensity of the peak at highest eKE.

In addition to the two direct detachment features, there is evidence of delayed autodetachment at $2.8 < h\nu < 3.5$ eV. Instead of the expected increase of eKE with photon energy, the photoelectron spectra show signals at a lower eKE, indicating that some of the available eKE has been converted to kinetic energy of the nuclei, probably by internal conversion.[62] Hence, in the $2.8 < h\nu < 3.5$ eV energy range, a resonance appears to be excited and its nuclear wavepacket and/or internal conversion dynamics are in competition with autodetachment from the resonance.

For $h\nu > 3.8$ eV, there also appears to be a dramatic change in the ratio of formation of the ground and first excited state of the neutral following electron detachment. Specifically, the neutral excited state appears to be produced more favourably compared to the ground state. As discussed below, this arises from the presence of a resonance for which autodetachment to the first excited state may be more favourable.

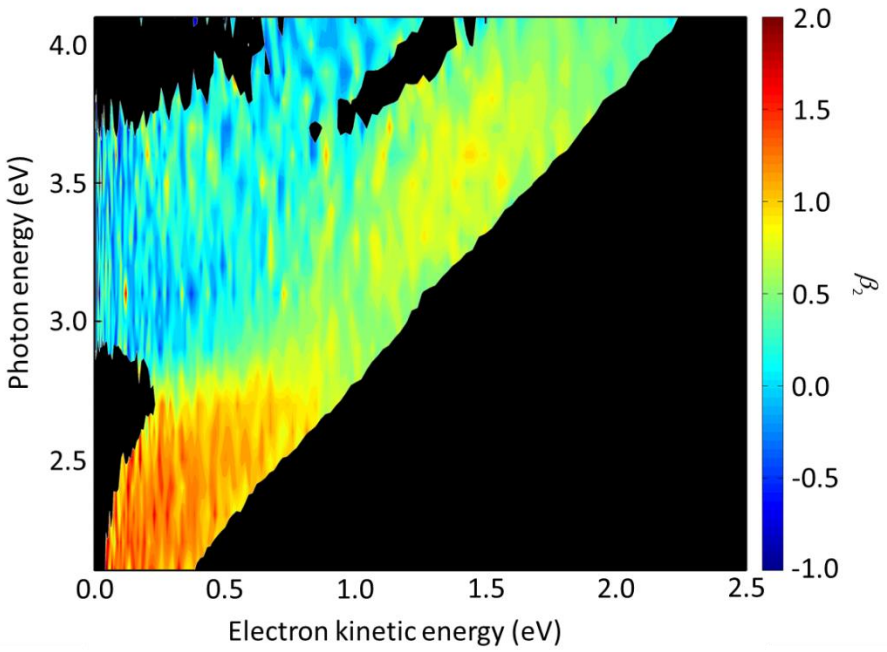

Figure 3.4 False-colour plot of the frequency-resolved β_2 spectra of 9-$C_{14}H_9^-$. The signals below intensity of 0.2 in Figure 3.3 have been blacked out because the signal levels were too low to determine a reliable β_2 parameter.

When comparing the two anion production schemes between the in-source CID and the photodissociation mentioned in section 3.3.1, it was clear that the optical process gave the better isomer selectivity, albeit at the expense of producing vibrationally hot molecules. By contrast the in-source methodology produces thermalized ions, however, due to the time delay between production at the start of the machine and photon interaction, on the order of milliseconds or more, various isomerisation processes could take place, and this is what was seen with the attempted production from the other initial acids.

Additional insight can be gained by considering the photoelectron angular distributions over those same features, as shown in Figure 3.4. The photoelectron spectra show strong anisotropy in certain spectral regions. The direct detachment feature that forms the neutral ground state exhibits an overall positive β_2. At low photon energy, the direct detachment has $\beta_2 = +1.3 \pm 0.1$. This is consistent with the observation of the Neumark group.[48] The photoelectrons arising from delayed autodetachment (lower eKE) in the $2.8 < h\nu < 3.5$ eV range are predominantly

isotropic with $\beta_2 \approx 0$. Similarly, detachment to form the first excited state of the neutral species appears to be isotropic.

Upon closer inspection, the anisotropy of the direct detachment feature that leaves the neutral radical in its ground state appears to change quite abruptly across the $h\nu$ range studied. In Figure 3.5, the β_2 parameter averaged over this direct detachment peak is shown as a function of $h\nu$ (and of eKE of the photoelectron). If direct detachment was the only available channel, the expectation would be to see slow variations with increasing photon energy. However, over the regions $2.8 < h\nu < 3.5$ eV and $h\nu > 3.8$ eV, there are strong deviations from this expected behaviour, which supports our earlier suggestion that resonances are excited in these regions.

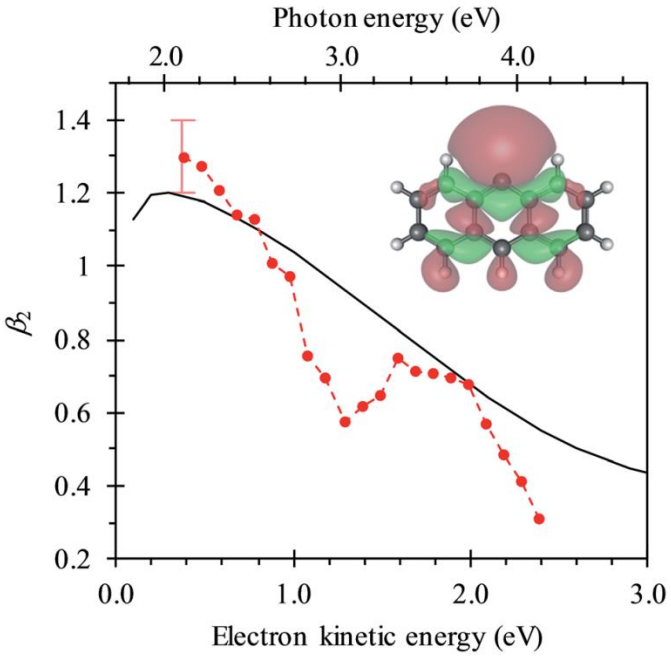

Figure 3.5 β_2 parameter of the direct detachment feature as a function of *hν* and eKE. The red points and dashed line indicate the experimentally determined values and the black solid line indicates the calculated β_2 parameter using the Dyson orbital shown. The experimental error shown on the first data point is similar for all the other data points.

Figure 3.6 shows the relevant calculated molecular orbitals (MOs) of 9-$C_{14}H_9^-$. The highest-occupied MO (HOMO) corresponds to the n-orbital localised primarily at the C9 position (see Figure 3.1), while the lowest-unoccupied MO (LUMO) is a

delocalised π^* orbital. Our calculations show that there are several excited states and resonances of 9-$C_{14}H_9^-$ that can be accessed in the photon energy range used in the present experiments. Figure 3.6 also shows an overview of the most relevant excited states (those with significant oscillator strengths). Many of the lowest lying excited states involve $^1n\pi^*$ states and consequently have very low oscillator strengths; the lowest lying anion $^1n\pi^*$ resonance is included in the energy level diagram. Based on our calculations, the most likely resonances that are excited around $2.8 < h\nu < 3.5$ eV and $h\nu > 3.8$ eV are the three lowest $^1\pi\pi^*$ transitions. The lowest $(1)^1\pi\pi^*$ transition is calculated to be at 3.14 eV. This calculated energy is consistent with the $2.8 < h\nu < 3.5$ eV range over which the deviation of the β_2 parameter was noted in Figure 3.5 and with the resonance signatures in the frequency-resolved photoelectron spectra in Figure 3.3. For $h\nu > 3.8$ eV, a deviation can be seen from the expected β_2 behaviour in Figure 3.5, which is consistent with the appearance of the next two $^1\pi\pi^*$ resonances: $(2)^1\pi\pi^*$ was calculated at 3.77 eV and $(3)^1\pi\pi^*$ at 4.12 eV photon energy. Interestingly, it is only the $(1)^1\pi\pi^*$ resonance that shows evidence of nuclear dynamics in competition with autodetachment as evidenced by Figure 3.3.

Figure 3.6 additionally shows the orbital configurations associated with the neutral ground state (X^2A_1) and its first excited state (A^2B_1). The ground state is formed by the loss of a non-bonding electron in the HOMO, while the first excited state is formed by the loss of a π-electron from the HOMO-1. All three $^1\pi\pi^*$ states predominantly involve the excitation of the HOMO-1 π-electron into a π^* MO. Hence, these resonances are of Feshbach character with respect to the electron-loss channel that forms the neutral ground state, but are of shape character with respect to the electron loss channel that leaves the neutral species in its first excited state. Because a Feshbach resonance involves a two-electron transition, the autodetachment lifetimes are typically longer compared to that of shape resonances, for which only a single electron transition is required.

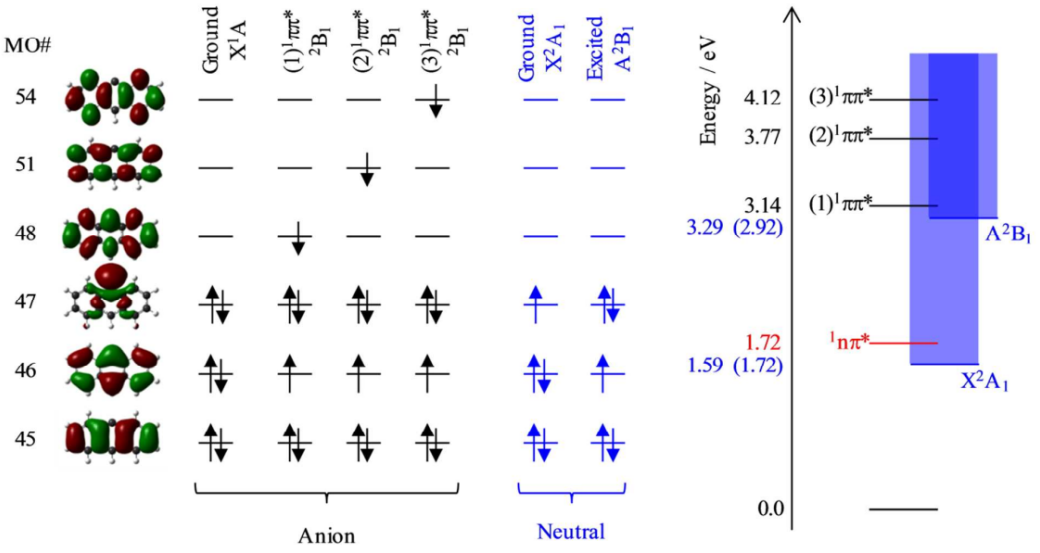

Figure 3.6 Summary of relevant molecular orbitals (MOs) of 9-$C_{14}H_9^-$ and dominant electron configurations of the relevant electronic states of the 9-$C_{14}H_9^-$ anion and the 9-$C_{14}H_9$ neutral. On the right are the calculated excited state energy levels with experimental values in parenthesis.

The adiabatic energy of the neutral excited state lies very close to the onset of the $(1)^1\pi\pi^*$ resonance, while the vertical energy of the neutral species (at the anion geometry) will be higher and was calculated to be at $h\nu = 3.29$ eV. As excitation occurs in the vertical region and the electron loss cross section is small for low eKE electrons, the $(1)^1\pi\pi^*$ resonance will predominantly decay by autodetachment to the ground state of the neutral species. This is a two-electron transition and as such autodetachment may be expected to be relatively slow. Therefore, one might anticipate that nuclear dynamics could compete with autodetachment, which is consistent with the observations in Figure 3.3.

The $(2)^1\pi\pi^*$ and $(3)^1\pi\pi^*$ excited states are too far above the threshold region for the autodetachment channel that leaves the neutral species in its excited state. Therefore, loss of the electron can proceed through a one-electron process (excited shape resonance) and the consequential increased autodetachment rate appears to outcompete the nuclear dynamics of the $(2)^1\pi\pi^*/(3)^1\pi\pi^*$ resonances so that the photoelectron peak essentially takes the spectral form of a direct detachment process as seen in Figure 3.3. As previously noted, the increase in yield of the neutral excited state when $h\nu > 3.8$ eV (see Figure 3.3) is fully consistent with the fact that the $(2)^1\pi\pi^*$ and $(3)^1\pi\pi^*$ resonances are only of shape-character with

respect to the neutral excited state, but of Feshbach-character with respect to the ground state. Hence autodetachment into the former channel is faster and therefore has a higher yield. Note that we cannot determine the branching ratios accurately because of the additional direct detachment channel that is always open for $h\nu > \text{ADE}$.

One aspect of the direct photodetachment from 9-$C_{14}H_9^-$ that is particularly clear is its anisotropy. This has previously been discussed by the Neumark group in their interpretation of their SEVI experiment.[48] The photoelectron angular distribution for direct detachment in the $0.0 < \text{eKE} < 0.3$ eV range was measured to be $\beta_2 = +1.3$.[48] This is in agreement with the β_2 parameters determined here in the same energy range (Figure 3.5). For higher eKE values, we observe a gradual decrease in β_2 as well as rapid changes. In order to confirm that the rapid changes correspond to the deviation of a smoothly varying β_2 parameter due to direct detachment, we have performed similar calculations to the Neumark group but over a wider eKE range. We believe that this specific β_2 parameter calculated by Neumark and coworkers may be erroneous because of the older version of QChem and/or ezDyson used in their calculations. In fact, visual inspection of the Dyson orbital shows that, while a large component of the orbital is of n-character which would lead to $\beta_2 = +2$, there is also significant π-character which should reduce this substantially, which is consistent with the predicted and observed β_2 parameter presented here.

The results from our calculations are shown by the solid line in Figure 3.5. The data are not scaled and yield $\beta_2 = +1.2$ for low eKE electrons, in excellent agreement with the experiment. As the eKE increases, the β_2 parameter smoothly decreases as anticipated. This overall trend is reproduced in the experimental data. However, over the ranges where resonance dynamics were noted ($2.8 < h\nu < 3.5$ eV and $h\nu > 3.8$ eV), the measured photoelectron angular distributions are significantly more isotropic than that predicted for direct detachment, confirming that the frequency-resolved β_2 parameter has identified the resonances.

The quantitative agreement between the experimental and calculated anisotropy is very encouraging. Our group has previously shown similar rapid changes in β_2 for *para*-benzoquinone radical anions,[39] which could also be correlated with the excitation and electron emission from resonances. This was previously discussed in section 1.4.2. However, in chemical derivatives of *para*-benzoquinone, the overall anisotropy tended to zero so that changes were difficult to discern.[25,26] For 9-$C_{14}H_9^-$, the clear anisotropy arises from its high (C_{2V}) symmetry, enabling full use of the angular dimension. Further theoretical developments to accurately predict photoelectron distributions for photo-detachment and specifically autodetachment may assist in identifying the nature of the resonances in favourable cases such as 9-$C_{14}H_9^-$.

3.3.3. Comparison to the Pyrene Anion

The frequency- and angle-resolved photoelectron spectra clearly show that nuclear resonance dynamics can compete with autodetachment from the $(1)^1\pi\pi^*$ resonance of 9-$C_{14}H_9^-$. The dynamics of the resonance involves nuclear wavepacket motion on the $(1)^1\pi\pi^*$ potential energy surface. Hence, autodetachment may occur along different coordinates of the $(1)^1\pi\pi^*$ surface which leads to different Franck-Condon factors to the neutral ground state and consequently to photoelectrons with a lower eKE relative to that for direct detachment. Additionally, internal conversion can occur from the $(1)^1\pi\pi^*$ resonance to lower-lying $^1n\pi^*$ resonances. Several such resonances were identified in our calculations. The population of the $^1n\pi^*$ resonances following a non-adiabatic transition from the $(1)^1\pi\pi^*$ state is expected to result in very fast autodetachment as these are of shape character relative to the neutral ground state. Unfortunately, we cannot determine whether such internal conversion processes are occurring from the present data.

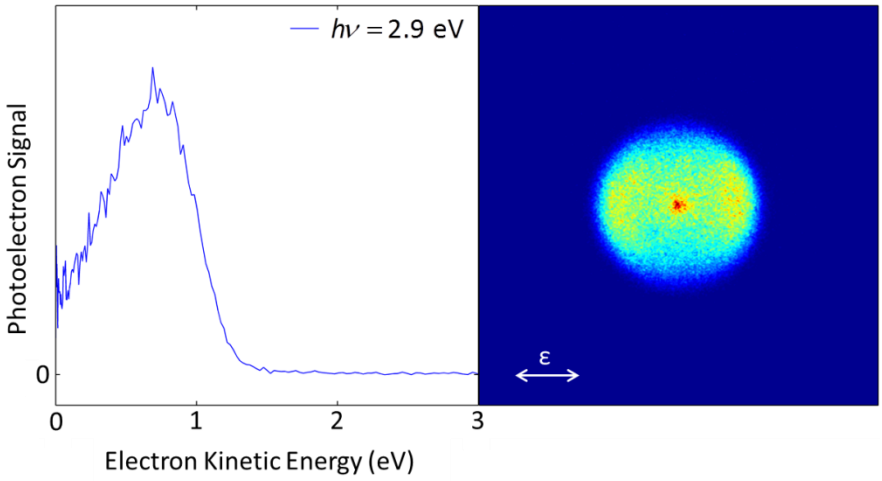

Figure 3.7 (Left) Individual photoelectron spectrum of 9-$C_{14}H_9^-$ taken at 2.9 eV of photon energy. (Right) The raw photoelectron image used to produce the spectrum. The laser polarisation is horizontal, as labelled.

Internal conversion to repopulate the ground electronic state of the anion is barely observed: this would be evidenced by the presence of very low energies in the photoelectron spectra that are statistically emitted (thermionic emission) from the hot anion. There is the suggestion of thermionic emission in the photoelectron images as can be seen in Figure 3.7, but the yield is very low. Hence, unlike the case of the tetracenyl anion, $C_{18}H_{11}^-$, for which intense thermionic emission was clearly seen, resonances in 9-$C_{14}H_9^-$ are not efficient in recovering the ground state. While 1-$C_{18}H_{11}^-$ has a higher density of resonances than 9-$C_{14}H_9^-$, a key additional difference between the two systems is that 1-$C_{18}H_{11}^-$ has several *bound* singlet excited electronic states. This is partly due to its higher ADE and partly due to the greater p-electron delocalisation in 1-$C_{18}H_{11}^-$. We have previously shown that in the menadione radical anion, efficient anion ground state recovery was facilitated by a bound excited state, which acted as an intermediate in an internal conversion cascade.[26] Hence, we suggest that 9-$C_{14}H_9^-$ does not efficiently reform the anion ground state in part because of the lack of anion bound states. We can therefore also suggest that 1-$C_{18}H_{11}^-$ is the smallest astrophysically relevant polyacenyl anion for which efficient ground state recovery can occur. Note that 1-$C_{14}H_9^-$, 2-$C_{14}H_9^-$, 2-$C_{18}H_{11}^-$ and 3-$C_{18}H_{11}^-$ may prove to be more efficient in this regard, but only the

lowest energy isomers (9-$C_{14}H_9^-$ and 1-$C_{18}H_{11}^-$) are expected to be prevalent in the interstellar medium; these can be formed by H-atom tunnelling from the other higher-lying isomers, which proceeds on timescales faster than the astronomically relevant ones.[63]

The observation of resonances in 9-$C_{14}H_9^-$ and their dynamics also has implications for the SEVI work reported by the Neumark group. Specifically, the SEVI experiment assumes that direct detachment into the continuum determines the vibrational structure of the neutral species. However, as the direct detachment cross section is low near the threshold, even optically weak transitions may become important, and we note that our calculations suggest that the lowest $^1n\pi^*$ resonance is close to the neutral state energy. If a resonance was accessed at the SEVI detachment energy, then this would lead to changes in the Franck–Condon factors of the neutral species, as was shown by Schiedt and Weinkauf in para-benzoquinone radical anions.[64] This should be apparent from changes in the peak intensities as the photon energy was changed and perhaps in the β_2 parameters associated with specific photoelectron peaks. In the data presented for the neutral ground state of 9-$C_{14}H_9^-$, there is no evidence of the participation of resonance excitation, however, the same is certainly not true for the first excited state of the neutral species. Fig. 3.3 clearly shows that the $(1)^1\pi\pi^*$ resonance produces photoelectrons essentially over the entire $\mathrm{eKE} < h\nu - \mathrm{ADE}$ range. Indeed, it is noted in their work that the β_2 parameters are likely distorted because of high-eKE electrons that are arising from direct detachment into the neutral ground state.[48] From our data, these "distorting" electrons are actually also at low-eKE because of the resonance dynamics of the $(1)^1\pi\pi^*$ state.

3.4. Conclusions

A new methodology for studying the resonances of closed shell PAH anions has been presented based on the CID of their respective carboxylic acids formed by electrospray ionisation. For different anthracene carboxylic acid isomers, only the most stable isomer of the anthracenyl anion ($9\text{-}C_{14}H_9^-$) is formed. It seems photodissociation yields the best isomer selectivity, although we note that the timescales of this experiment are very short (i.e. ~6 ns) such that any post-dissociation isomerisation may yet occur. Frequency and angle-resolved photoelectron imaging of $9\text{-}C_{14}H_9^-$ was used to identify and characterise the dynamics of a number of resonances. The lowest lying π^* resonance shows rapid nuclear dynamics that are in competition with autodetachment. However, ground-state recovery was observed to be inefficient. Two higher-lying π^* resonances were observed to rapidly decay by autodetachment. All observations could be accounted for using supporting electronic-structure calculations. In particular, our data and calculations show how photoelectron anisotropy can be used to identify the presence of resonances. Closed shell PAH anions have been implicated to exist in the interstellar medium, where, in the absence of a sufficiently large dipole moment, electron attachment through resonances may be a key formation mechanism. Our results show that the predominant decay mechanism for resonances in $9\text{-}C_{14}H_9^-$ is autodetachment, which is in contrast to the next polyacene increment, the tetracenyl anion, for which ground state recovery has been reported previously.[24] Therefore, the latter is the smallest polyacenyl anion for which this process can occur and therefore is also the smallest likely polyacenyl anion to be found in the interstellar medium. With the development of this new methodology, we will now be able to explore a wide range of large PAHs to determine the role of resonances in their anion formation.

3.5. References

1 C. Barckholtz, T. A. Barckholtz and C. M. Hadad, *J. Am. Chem. Soc.*, 1999, **121**, 491–500.
2 H. F. Calcote, *Combust. Flame*, 1981, **42**, 215–242.
3 H. Richter, O. A. Mazyar, R. Sumathi, W. H. Green, J. B. Howard and J. W. Bozzelli, *J. Phys. Chem. A*, 2001, **105**, 1561–1573.
4 R. G. Harvey and N. E. Geacintov, *Acc. Chem. Res.*, 1988, **21**, 66–73.
5 J. L. Durant, W. F. Busby, A. L. Lafleur, B. W. Penman and C. L. Crespi, *Mutat. Res. Toxicol.*, 1996, **371**, 123–157.
6 T. M. Figueira-Duarte and K. Müllen, *Chem. Rev.*, 2011, **111**, 7260–7314.
7 X. Guo, M. Baumgarten and K. Müllen, *Prog. Polym. Sci.*, 2013, **38**, 1832–1908.
8 H. Ju, K. Wang, J. Zhang, H. Geng, Z. Liu, G. Zhang, Y. Zhao and D. Zhang, *Chem. Mater.*, 2017, **29**, 3580–3588.
9 I. A. Rodríguez-Pérez, Z. Jian, P. K. Waldenmaier, J. W. Palmisano, R. S. Chandrabose, X. Wang, M. M. Lerner, R. G. Carter and X. Ji, *ACS Energy Lett.*, 2016, **1**, 719–723.
10 A. G. G. M. Tielens, *Annu. Rev. Astron. Astrophys.*, 2008, **46**, 289–337.
11 A. G. G. M. Tielens, *Rev. Mod. Phys.*, 2013, **85**, 1021–1081.
12 L. J. Allamandola, A. G. G. M. Tielens and J. R. Barker, *Astrophys. J. Suppl. Ser.*, 1989, **71**, 733–775.
13 J. L. Puget and A. Léger, *Annu. Rev. Astron. Astrophys.*, 1989, **27**, 161–198.
14 E. K. Campbell, M. Holz, D. Gerlich and J. P. Maier, *Nature*, 2015, **523**, 322–323.
15 M. C. McCarthy, C. A. Gottlieb, H. Gupta and P. Thaddeus, *Astrophys. J. Lett.*, 2006, **652**, L141.
16 S. Brünken, H. Gupta, C. A. Gottlieb, M. C. McCarthy and P. Thaddeus, *Astrophys. J. Lett.*, 2007, **664**, L43.
17 J. Cernicharo, M. Guélin, M. Agúndez, K. Kawaguchi, M. McCarthy and P. Thaddeus, *Astron. Astrophys.*, 2007, **467**, L37–L40.
18 N. J. Demarais, Z. Yang, O. Martinez, N. Wehres, T. P. Snow and V. M. Bierbaum, *Astrophys. J.*, 2012, **746**, 32.
19 S. Lepp and A. Dalgarno, *Astrophys. J.*, 1988, **324**, 553–556.
20 V. Wakelam and E. Herbst, *Astrophys. J.*, 2008, **680**, 371.
21 P. J. Sarre, *Mon. Not. R. Astron. Soc.*, 2000, **313**, L14–L16.
22 K. D. Jordan and F. Wang, *Annu. Rev. Phys. Chem.*, 2003, **54**, 367–396.
23 J. Simons, *J. Phys. Chem. A*, 2008, **112**, 6401–6511.
24 J. N. Bull, C. W. West and J. R. R. Verlet, *Phys. Chem. Chem. Phys.*, 2015, **17**, 32464–32471.
25 J. N. Bull, C. W. West and J. R. R. Verlet, *Chem. Sci.*, 2015, **6**, 1578–1589.
26 J. N. Bull, C. W. West and J. R. R. Verlet, *Phys. Chem. Chem. Phys.*, 2015, **17**, 16125–16135.
27 M. Bixon and J. Jortner, *J. Chem. Phys.*, 1968, **48**, 715–726.
28 K. D. Jordan and P. D. Burrow, *Chem. Rev.*, 1987, **87**, 557–588.
29 H. S. Taylor, G. V. Nazaroff and A. Golebiewski, *J. Chem. Phys.*, 1966, **45**, 2872–2888.

30 R. V. Khatymov, R. F. Tuktarov and M. V. Muftakhov, *JETP Lett.*, 2011, **93**, 437–441.
31 J. Cernicharo, M. Guélin, M. Agúndez, M. C. McCarthy and P. Thaddeus, *Astrophys. J. Lett.*, 2008, **688**, L83.
32 M. Larsson, W. D. Geppert and G. Nyman, *Rep. Prog. Phys.*, 2012, **75**, 066901.
33 G. Israël, C. Szopa, F. Raulin, M. Cabane, H. B. Niemann, S. K. Atreya, S. J. Bauer, J.-F. Brun, E. Chassefière, P. Coll, E. Condé, D. Coscia, A. Hauchecorne, P. Millian, M.-J. Nguyen, T. Owen, W. Riedler, R. E. Samuelson, J.-M. Siguier, M. Steller, R. Sternberg and C. Vidal-Madjar, *Nature*, 2005, **438**, 796–799.
34 A. J. Coates, F. J. Crary, G. R. Lewis, D. T. Young, J. H. Waite and E. C. Sittler, *Geophys. Res. Lett.*, 2007, **34**, L22103.
35 C. Walsh, N. Harada, E. Herbst and T. J. Millar, *Astrophys. J.*, 2009, **700**, 752.
36 R. C. Fortenberry, *J. Phys. Chem. A*, 2015, **119**, 9941–9953.
37 J. Gao, G. Berden and J. Oomens, *Astrophys. J.*, 2014, **787**, 170.
38 J. N. Bull, C. W. West and J. R. R. Verlet, *Chem. Sci.*, 2016, **7**, 5352–5361.
39 C. W. West, J. N. Bull, E. Antonkov and J. R. R. Verlet, *J. Phys. Chem. A*, 2014, **118**, 11346–11354.
40 D. A. Horke, Q. Li, L. Blancafort and J. R. R. Verlet, *Nat. Chem.*, 2013, **5**, 711–717.
41 C. W. West, A. S. Hudson, S. L. Cobb and J. R. R. Verlet, *J. Chem. Phys.*, 2013, **139**, 071104.
42 C. W. West, J. N. Bull, A. S. Hudson, S. L. Cobb and J. R. R. Verlet, *J. Phys. Chem. B*, 2015, **119**, 3982–3987.
43 C. W. West, J. N. Bull and J. R. R. Verlet, *J. Phys. Chem. Lett.*, 2016, **7**, 4635–4640.
44 R. R. Squires, *Acc. Chem. Res.*, 1992, **25**, 461–467.
45 Z. Tian and S. R. Kass, *Chem. Rev.*, 2013, **113**, 6986–7010.
46 I. H. Krouse and P. G. Wenthold, *J. Am. Soc. Mass Spectrom.*, 2005, **16**, 697–707.
47 C. H. DePuy, V. M. Bierbaum, L. A. Flippin, J. J. Grabowski, G. K. King, R. J. Schmitt and S. A. Sullivan, *J. Am. Chem. Soc.*, 1980, **102**, 5012–5015.
48 M. L. Weichman, J. A. DeVine, D. S. Levine, J. B. Kim and D. M. Neumark, *Proc. Natl. Acad. Sci.*, 2016, **113**, 1698–1705.
49 S. W. Froelicher, B. S. Freiser and R. R. Squires, *J. Am. Chem. Soc.*, 1986, **108**, 2853–2862.
50 F. Muntean and P. B. Armentrout, *J. Chem. Phys.*, 2001, **115**, 1213–1228.
51 J. L. Goldfarb and E. M. Suuberg, *J. Chem. Eng. Data*, 2008, **53**, 670–676.
52 M. J. Frisch, G. W. Trucks, J. R. Cheeseman, G. Scalmani, M. Caricato, H. P. Hratchian, X. Li, V. Barone, J. Bloino, G. Zheng, T. Vreven, J. A. Montgomery, G. A. Petersson, G. E. Scuseria, H. B. Schlegel, H. Nakatsuji, A. F. Izmaylov, R. L. Martin, J. L. Sonnenberg, J. E. Peralta, J. J. Heyd, E. Brothers, F. Ogliaro, M. Bearpark, M. A. Robb, B. Mennucci, K. N. Kudin, V. N. Staroverov, R. Kobayashi, J. Normand, A. Rendell, R. Gomperts, V. G. Zakrzewski, M. Hada, M. Ehara, K. Toyota, R. Fukuda, J. Hasegawa, M. Ishida, T. Nakajima, Y. Honda, O. Kitao and H. Nakai, *Gaussian 09*.
53 H. A. Galué and J. Oomens, *Astrophys. J.*, 2012, **746**, 83.
54 J. Schiedt and R. Weinkauf, *Chem. Phys. Lett.*, 1997, **266**, 201–205.
55 S. Hirata and M. Head-Gordon, *Chem. Phys. Lett.*, 1999, **314**, 291–299.
56 A. I. Krylov, *Annu. Rev. Phys. Chem.*, 2008, **59**, 433–462.
57 Y. Shao, Z. Gan, E. Epifanovsky, A. T. B. Gilbert, M. Wormit, J. Kussmann, A. W. Lange, A. Behn, J. Deng, X. Feng, D. Ghosh, M. Goldey, P. R. Horn, L. D. Jacobson, I.

Kaliman, R. Z. Khaliullin, T. Kuś, A. Landau, J. Liu, E. I. Proynov, Y. M. Rhee, R. M. Richard, M. A. Rohrdanz, R. P. Steele, E. J. Sundstrom, H. L. Woodcock III, P. M. Zimmerman, D. Zuev, B. Albrecht, E. Alguire, B. Austin, G. J. O. Beran, Y. A. Bernard, E. Berquist, K. Brandhorst, K. B. Bravaya, S. T. Brown, D. Casanova, C.-M. Chang, Y. Chen, S. H. Chien, K. D. Closser, D. L. Crittenden, M. Diedenhofen, R. A. DiStasio Jr, H. Do, A. D. Dutoi, R. G. Edgar, S. Fatehi, L. Fusti-Molnar, A. Ghysels, A. Golubeva-Zadorozhnaya, J. Gomes, M. W. D. Hanson-Heine, P. H. P. Harbach, A. W. Hauser, E. G. Hohenstein, Z. C. Holden, T.-C. Jagau, H. Ji, B. Kaduk, K. Khistyaev, J. Kim, J. Kim, R. A. King, P. Klunzinger, D. Kosenkov, T. Kowalczyk, C. M. Krauter, K. U. Lao, A. D. Laurent, K. V. Lawler, S. V. Levchenko, C. Y. Lin, F. Liu, E. Livshits, R. C. Lochan, A. Luenser, P. Manohar, S. F. Manzer, S.-P. Mao, N. Mardirossian, A. V. Marenich, S. A. Maurer, N. J. Mayhall, E. Neuscamman, C. M. Oana, R. Olivares-Amaya, D. P. O'Neill, J. A. Parkhill, T. M. Perrine, R. Peverati, A. Prociuk, D. R. Rehn, E. Rosta, N. J. Russ, S. M. Sharada, S. Sharma, D. W. Small, A. Sodt, T. Stein, D. Stück, Y.-C. Su, A. J. W. Thom, T. Tsuchimochi, V. Vanovschi, L. Vogt, O. Vydrov, T. Wang, M. A. Watson, J. Wenzel, A. White, C. F. Williams, J. Yang, S. Yeganeh, S. R. Yost, Z.-Q. You, I. Y. Zhang, X. Zhang, Y. Zhao, B. R. Brooks, G. K. L. Chan, D. M. Chipman, C. J. Cramer, W. A. G. III, M. S. Gordon, W. J. Hehre, A. Klamt, H. F. S. III, M. W. Schmidt, C. D. Sherrill, D. G. Truhlar, A. Warshel, X. Xu, A. Aspuru-Guzik, R. Baer, A. T. Bell, N. A. Besley, J.-D. Chai, A. Dreuw, B. D. Dunietz, T. R. Furlani, S. R. Gwaltney, C.-P. Hsu, Y. Jung, J. Kong, D. S. Lambrecht, W. Liang, C. Ochsenfeld, V. A. Rassolov, L. V. Slipchenko, J. E. Subotnik, T. V. Voorhis, J. M. Herbert, A. I. Krylov, P. M. W. Gill and M. Head-Gordon, *Mol. Phys.*, 2015, **113**, 184–215.

58 C. M. Oana and A. I. Krylov, *J. Chem. Phys.*, 2007, **127**, 234106.

59 Y. Liu and C. Ning, *J. Chem. Phys.*, 2015, **143**, 144310.

60 C. M. Oana and A. I. Krylov, *J. Chem. Phys.*, 2009, **131**, 124114.

61 A. I. Krylov and S. Gozem, *ezDyson*.

62 C. S. Anstöter, J. N. Bull and J. R. R. Verlet, *Int. Rev. Phys. Chem.*, 2016, **35**, 509–538.

63 F. Trixler, *Curr. Org. Chem.*, 2013, **17**, 1758–1770.

64 J. Schiedt and R. Weinkauf, *J. Chem. Phys.*, 1999, **110**, 304–314.

4. Dynamics of the Meta-Substituted Variant of the Chromophore Anion in the Green Fluorescent Protein.

This chapter describes the study of a structural isomer of the chromophore of the Green Fluorescent Protein (GFP). Frequency-, angle-, and time-resolved photoelectron spectroscopy were all brought to bear upon the problem. This provided some level of understanding of the dynamics, which is discussed with reference to the contributions of our computational collaborators.

4.1. Introduction

Fluorescent proteins and their subsequent use for the study of biological processes has dramatically altered the field of molecular biology since their discovery. Their ability to be added to the genome of a target organism and expressed with a clear fluorescence from within a living target was noticed early. However it was the possibility of detection when expressed attached or even within another protein that has caused their rise from obscurity.[1–3] The discovery and development of the first of these, the green fluorescent protein (GFP), as an optical probe for previously invisible processes such as the growth of nerve cells in the brain was recognised with the 2008 Nobel Prize in Chemistry.[1] The fluorescent properties that make GFP so useful to biologists are due to the presence of a central chromophore. When present as part of GFP, the chromophore is held in a 11 stranded β-barrel, as seen in Figure 4.1.[4]

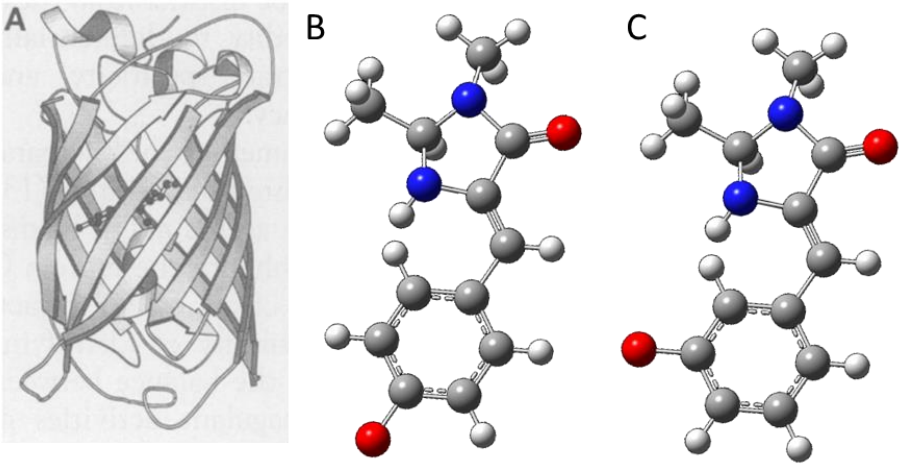

Figure 4.1 (A) Schematic drawing of the structure of the GFP, showing the chromophore within the β-barrel structure. From Ref. 4 Reprinted with permission from AAAS. (B) Ball-and-stick model of the 4-(*para*-hydroxybenzylidene)-5-imidazolinone (*para*-HBDI) anion. (C) Ball-and-stick model of the *meta*-HBDI anion.

The chromophore present in GFP is structurally similar to the molecule shown in Figure 4.1 (B), 4-(*para*-hydroxybenzylidene)-5-imidazolinone (HBDI).[5,6] Furthermore it is also known that both neutral and anionic (deprotonated) forms are present within the protein.[7,8] GFP is known for having two broad absorption peaks, with each having a different assignment. The higher energy band (centred around 396

nm) is an absorption by the neutral molecule with subsequent proton transfer to produce the anionic form.[9,10] The lower energy band (centred around 476 nm) is assigned to an absorption by the anionic form of the chromophore. The fluorescence is in either case from the deprotonated anion.

The presence of the protein and the corresponding interactions clearly have an effect on the chromophore's dynamics. The intact protein has a high fluorescence quantum yield,[11,12]

$$\Phi_f \approx 0.8 \ . \tag{4.1}$$

In solution, the isolated chromophore had a quantum yield of

$$\Phi_f < 0.0001 \tag{4.2}$$

and did not fluoresce until the sample had been frozen as part of an ethanol glass.[13] In addition, the absorption bands of GFP are shifted when compared to that of the chromophore in solution. Comparison of different solvents showed that the anionic form was more affected by the presence of solvent, but there was always a shift from higher energy to lower energy upon formation of the anion.[13] However, both absorption peaks were blue-shifted relative to the corresponding band of the protein.

The structure of the protein backbone could be seen as providing a nearly gas-phase environment, due to the β-barrel excluding solvent molecules from the vicinity of the chromophore. However, the photophysics is not that simple. The neutral from of HBDI in the gas phase has been observed to have a significant blue shift (0.5 eV) in the absorption spectrum relative to the protein.[14] Conversely, the anionic form more closely resembles the absorption of the GFP protein.[14,15] The transition to the first exited state of the bare anion has been shown to be extremely similar to that when present in the barrel.[15] This implies that the protein structure has an effect on the dynamics of the chromophore, which is most pronounced upon the neutral form.

Considerable work has been done to understand the dynamics of the anionic chromophore in the gas phase.[2,5,6,16–18] Much less has focussed on the structurally similar *meta*- variation, shown in Figure 4.1 (C). This chapter presents the investigation of the excited-state behaviour of the deprotonated anion, *meta*-HBDI$^-$, especially taking a view of contrast to the *para*- version. It is hoped that some light may be shed on the "choice" of *para*-HBDI as the chromophore, rather than perhaps the *meta*- form. To compare these two similar molecules and the effect of that small structural change has upon their energy levels and dynamics is a fundamental question of physical chemistry.

4.2. Experimental

Data was taken using the previous design of the spectrometer as detailed in chapter 2. *Meta*-HBDI was provided by the group of Professor Lars Andersen of Aarhus University. The HBDI anions were produced by electrospray ionisation of a $\sim$1 mM solution of the neutral molecule in MeOH which was deprotonated by the addition of a few drops of a 2M solution of NH_3 in MeOH. Frequency resolved data were taken using the nanosecond laser system described in section 2.1.2. This provided laser pulses of $\sim$6 ns duration at photon energies spanning 270 nm (4.6 eV) to 680 nm (1.82 eV). Time-resolved experiments were conducted using the femtosecond laser system described in section 2.1.2. This was used to provide an 800 nm probe pulse directly and the second-harmonic stage was used to generate a 400 nm pump pulse.

4.3. Results and Analysis

The frequency-resolved spectra were taken of *meta*-HBDI$^-$ for photon energies ranging from 2.5 eV (500 nm) to 4.3 eV (290 nm) in steps of 10 nm. This is presented in Figure 4.2. This data has been normalised to the maximum peak intensity for each spectrum. Presented below it is the associated anisotropy

parameter, β_2, with the shaded regions corresponding to those regions of the frequency spectra where the normalised peak intensity was less than 0.3.

A few features are immediately obvious. The simplest of these to explain is the direct detachment peak progressing diagonally for $h\upsilon > 2.8$ eV. Using the outer edge of this peak, the adiabatic detachment energy (ADE) of the *meta*-HBDI anion is 2.30 ± 0.05 eV. This is in agreement with the lower resolution photoelectron spectra taken by Bochenkova *et al*.[6] The direct detachment process corresponds to removal of an electron from the highest-occupied molecular orbital (HOMO) to the ground state (doublet, D_0) of the neutral.

In addition to this direct detachment to the neutral ground state, there is some evidence for a detachment to an excited state. A faint diagonal can be seen for $h\nu > 3.9$, starting from an eKE of ~ 0.5 eV. This feature follows the main direct detachment feature looking approximately parallel. This peak would be indicative of a direct detachment to this neutral excited state.

The majority of the dynamics takes place between $2.5 \leq h\nu \leq 3.5$ eV. Within this energy range, photodissociation was observed by the emergence of a peak of lower flight time in the TOF mass-spectrum upon the addition of the laser beam. Specifically, after the laser interaction, the ion beam is deflected onto the MCP and this short acceleration acts as a secondary time-of-flight spectrometer, although it offers very little mass resolution. The most likely fragment is loss of CH_3 from the *meta*-$HBDI^-$, similar to that observed in the *para*- isomer.[6,17]

A clear feature below eKE of 0.2 eV can be seen in Figure 4.2 that is independent of photon energy. The fact that it is invariant with photon energy and appears at low eKE is indicative of a relatively slow and indirect detachment process. However, this peak does not have the appearance of thermionic emission which has a typical Boltzmann distribution. We therefore tentatively assign this feature to arise from a decay though vibrational autodetachment. This process comprises the ejection of an electron after the coupling of an excited electronic state of the anion to a vibrationally-excited neutral ground state.

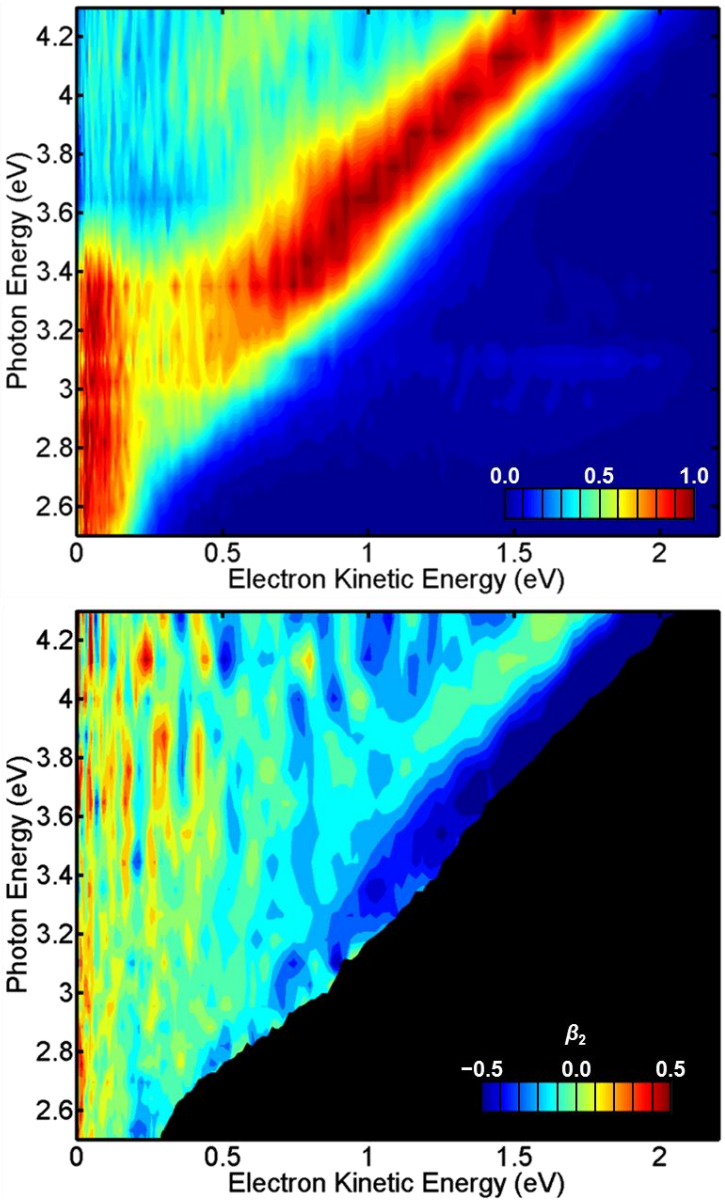

Figure 4.2 (Upper) Frequency-resolved spectra of *meta*-HBDI$^-$ normalised to the maximum peak intensity from 2.47 eV to 4.27 eV (500 nm to 290 nm) of incident photon energy. (Lower) the associated anisotropy parameters, with the shaded area corresponding to regions of normalised intensity <0.3.

The presence of a resonance can be seen in the anisotropy parameter, β_2. Looking at the direct detachment peak as it passes though $h\upsilon \approx 3.2$ eV, a fairly sharp decrease occurs, inferring the contribution of a new electronic state.

Lastly, a small quantity of multi-photon signal can be seen at $h\nu = 3.1$ eV, present at eKE ≈ 1.8 eV . This is mildly unexpected as this is a wavelength of lower power due to the OPO used to generate the laser pulses. This observation suggests the presence of a resonance that leads to a sufficiently long-lived excited state that can

absorb a second photon at this photon energy. In order to further study these apparent dynamics, we used time-resolved photoelectron spectroscopy.

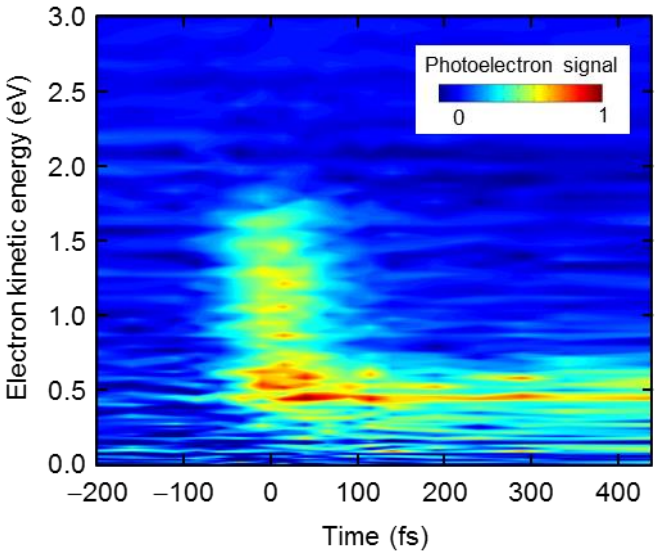

Figure 4.3 False colour photoelectron spectra of *meta*-HBDI$^-$ taken with a 400 nm (3.1 eV) pump followed by an 800 nm (1.55 eV) probe. The signal has been background subtracted using (t_0 -500) fs data.

Figure 4.3 shows the time-resolved photoelectron spectra following excitation at 400 nm and probing at 800 nm. Each spectrum has a photoelectron spectrum from 500 fs before t_0 subtracted such that only time-evolving features remain. The intensity of the laser was kept low to avoid multiphoton processes (when the 800 nm is too intense, it can excite the resonance through a two-photon transition leading to dynamics in the reverse temporal direction). Two features evolving at different timescales are immediately obvious in the time-resolved data presented in Figure 4.3. There is a fast-decaying feature at $0.8 < \mathrm{eKE} < 1.5$ and a much-slower decaying feature at $\mathrm{eKE} \approx 0.4$ eV. This lower energy feature can be seen to shift with time, from an initial value just after t_0 of around 0.6 eV, changing quickly to 0.4 eV and remaining there. To measure the lifetimes of these signals, the signal was integrated and the results shown in Figure 4.4.

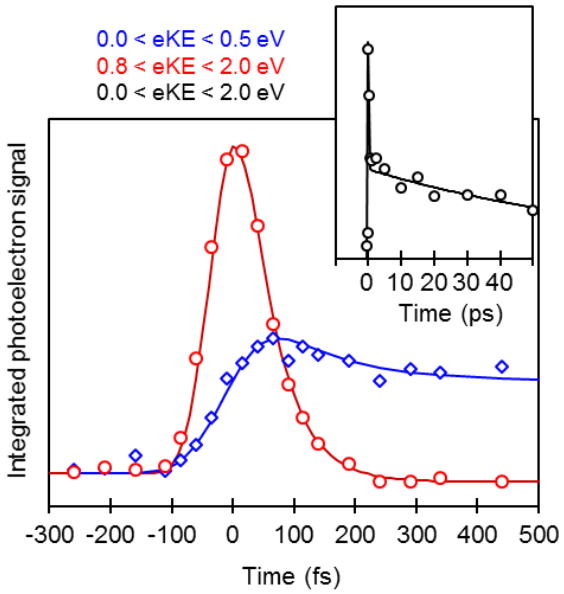

Figure 4.4 Integrated signal of the features present in the time-resolved spectra of *meta*-HBDI$^-$. (Main) Integrated signal for the fast decay, red, over the eKE range shown in the key, and for the slower feature, blue. Both are plotted using the data set for Figure 4.3. (Inset) Signals integrated over both features for long time delay information. This was taken from an earlier dataset to consider slower dynamics. Associated lifetimes are present in the text.

The fast feature, plotted in red in Figure 4.4, has been fitted to a convolution of an exponential and a Gaussian with a full-width-half-maximum of 80 fs. This decays quickly with a measured lifetime of $\tau = 50 \pm 10$ fs. This decay aligns with the rise of the longer-lived feature, plotted in blue, implying the movement of population from the first state to the second. This was again fitted to a convolution of a Gaussian and an exponential and produced a decay lifetime of 120 ± 15 fs. A separate dataset was used for long time-delay data points to estimate the lifetime of the slower delay, pictured in the inset of Figure 4.4. This was estimated as 90 ± 30 ps.

4.4. Discussion

To consider the dynamics of the system it is useful to consider the energetics of the possible states that are involved; this is presented in Figure 4.5. This shows the expected positions of both neutral and anionic states that could be involved in either the frequency- or time-resolved experiments. Their relative energies and labels are taken from the computational work done by Bochenkova *et al*.[6]

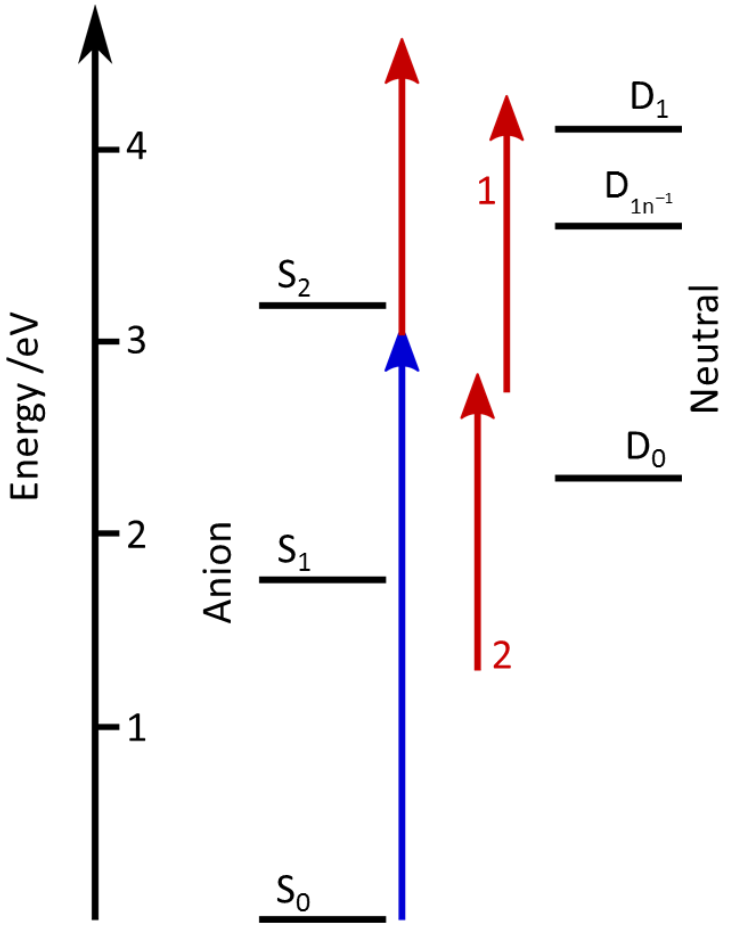

Figure 4.5 To-scale Jablonski diagram of the ground states and excited states potentially involved in the experiment of both the neutral and anionic form of *meta*-HBDI$^-$. The energy scale is relative to the anion ground state. The pump pulse of the time-resolved work is represented by the blue arrow, the probe pulse by red arrows. Energy levels used are those calculated by Bochenkova *et al.,* with the exception of the D_0 state, this is plotted at the ADE given earlier.[6] The two numbered probe pulses indicate particular situations, which are explained in the text.

The direct detachment feature to an excited neutral state, seen in Figure 4.2, is clear at $h\nu = 4.0\,\text{eV}$ providing an estimate of the adiabatic energy being $\sim 3.5\,\text{eV}$ above that of the anionic ground state. Comparison with Figure 4.5 would tentatively assign this to production of the $D_{1n^{-1}}$ neutral state at 3.6 eV. This would correspond to the production of a neutral via the loss of a non-bonding electron and would account for the significantly lower intensity of this peak in comparison to that of the ground state direct detachment.

The low-energy feature (eKE <0.2 eV) in the frequency-resolved spectra appears to arise from an indirect vibrational autodetachment process. The closest anionic state to that of the neutral is the S_1 state predicted at around 700 nm (1.77 eV).[6]

Autodetachment from vibrational states of S_1 would be consistent with the observed feature. However, Bochenkova *el al*. also noted that a dipole-bound state exists near threshold and they suggested that electron emission may be due to vibrational autodetachment from this dipole-bound state.[6]

The resonance shown by the multi-photon process along with the change in the anisotropy parameter in Figure 4.2 can be assigned to the presence of the S_2 anionic excited state, which is calculated to lie at 385 nm (3.2 eV).[6]

Hence, excitation at 400 nm and the subsequent dynamics shown in Figure 4.3, starts with population of the S_2 state. The fast decay process has a maximum eKE of around 2 eV. The pump and probe energy combined is 4.65 eV and the D_0 state is 2.3 eV above the anion. Therefore, the maximum kinetic energy release in the outgoing electron from the S_2 state is ~ 2.35 eV. The observed maximum is somewhat less than this suggesting that some energy (~ 0.3 eV) has already dissipated. This situation is shown by the probe pulse labelled 1 in Figure 4.5. This could correspond to ultrafast conversion to the vibrationally-excited region of the S_1 state before absorption of the probe pulse and would imply that the initially excited S_2 state is not observed in the time-resolved measurements, perhaps because of a low detachment cross section.

The other important feature is that at $\text{eKE} \approx 0.5$ eV. The origin of this detachment peak is schematically represented by the arrow marked 2 in Figure 4.5. The energetic position of this arrow implies one of two situations, either there has been more fast internal conversion, or the S_1 state has a lower global minimum than that of the vertical transition from the anionic ground state.

The above interpretation has been reached though a collaboration with the computational group of Anastasia Bochenkova.[19] Their work has found three different conical intersections, one between the S_2 and S_1 state and two separate intersections between the S_1 and S_0 states. Upon excitation at 400 nm, the S_2 state is populated but immediately starts a process of internal conversion to the S_1 sate via the S_2/S_1 conical intersection. From the S_1 state the system can then progress in two different directions and the wavepacket bifurcates. There is a fast decay back

to the anionic ground state through a relatively low gradient conical intersection. The alternative is to progress towards an alternative conical intersection that has a local minimum nearby. This minimum allows for the system to "sit" near to the conical intersection for a time before progressing though it as a barrier on the excited state surface impedes direct access to the conical intersection. The length of time spent in this local minimum would result in a relatively narrow eKE distribution, consistent with the narrow distribution observed in the time-resolved photoelectron electron spectra and its associated long lifetime of ~ 90 ps.

The computational results provide an explanation of the dynamics seen within the experiment. The initial fast decay is sampling the system as it progresses on the S_1 surface immediately after internal conversion though the S_2/S_1 CI. The width of the photoelectron peak points to a large difference in gradients of the S_1 and final D_0 states and the lifetime corresponds to rapid internal conversion from S_1 to S_0 through one of two S_1/S_0 conical intersections. However, this decay only captures part of the wavepacket. A portion of the wavepacket on the S_1 state progresses to a minimum where is remains for some time as internal vibrational redistribution dissipates the initial motion along a few vibrational modes to all the available modes in the molecule. A barrier on the S_1 state to a second conical intersection with the S_0 state can then be "thermally" accessed leading to the much slower decay observed and the narrow eKE distribution. The observed 120 fs timescale is likely an artefact of the fact that both dynamics are spectrally overlapping and the low eKE peak contains some decay of the fast channel.

It is instructive to compare these dynamics with that of the *para*- chromophore. The *para*-HBDI$^-$ S_1 state is one of the principal states for fluorescence in the protein.[11,19] This state is formally bound with respect to the D_0 ground neutral state. However, autodetachment is seen from the S_1 state.[5] It is also an optically very bright state. At higher excitation energies, *para*-HBDI$^-$ shows the onset of a pair of excited anionic states with a considerable broadening feature due to the internal conversion form the optically accessible S_3 state to the S_2 state followed by autodetachment to the D_0 ground state. For $h\nu > 4.2$ eV, this autodetachment

channel switches due to the onset of the D_1 state. The dynamics in the meta isomer are at first glance very different. The meta-substitution on the phenolate ring disrupts the resonance structure of its para-isomer which causes much of the observed changes. Nonetheless, there are also some remarkable similarities. In a very recent study, the isolated para-HBDI$^-$ S_1 state has been observed to have a strongly temperature dependent lifetime.[21] At low temperature, the S_1 state effectively becomes fluorescent, similar to observations in solution. Calculations show that, similar to *meta*-HBDI$^-$, the S_1 state has a barrier to overcome before it can reach the conical intersection that takes it to the ground state. At high *T*, this barrier is readily overcome by the thermal energy in all the modes of the molecule (see Chapter 1). Hence, while *para*-HBDI$^-$ is of course different, it is perhaps surprising to note that the S_1 state of both *meta*- and *para*-isomers have similar barriers to accessing efficient decay routes. Of course, *meta*-HBDI$^-$ has a second direct path to the ground state which the *para*-isomer does not. This direct path will lower the ultimate fluorescence quantum yield achievable and consequently, *para*-HBDI$^-$ represents a better chromophore for GFP.

4.5. Conclusion

To summarise, frequency-, angle-, and time-resolved photoelectron spectroscopy has been utilised to study the *meta*- variant of a model GFP chromophore. The frequency-resolved spectra show the effect of direct detachment to the neutral ground state along with a small contribution to a neutral excited state. The effect of one anionic excited-state resonance was also observed, the S_2 state, for $h\nu \approx 3.1$ eV.

The dynamics of the resonance around 3.1 eV were then studied using time-resolved photoelectron spectroscopy. After excitation to this state, population is believed to progress quickly though a conical intersection to the S_1 state. The motion on the S_1 sate was then probed with two possible CI decay routes proposed.[19] One of these is a fast, relatively broad eKE decay, with the other route

being defined by a localised minimum near to the CI that correspondingly has a much longer decay rate and a narrower eKE profile.

To discuss the *meta*-HBDI anion, it is inherently necessary to compare it to its better-known isomer, the biologically favoured *para*-HBDI chromophore. One of the major differences comprises the nature of the first excited state, in the *para*-form, this is a very bright state that contributes to the fluorescence of the GFP structure. This fluorescence is not generally seen in the gas phase due to a rotation around a central carbon bond that is inhibited within the protein, suspended in a glass or cooled to cryogenic temperatures.[11,22] The first excited state of the *meta*-form is inherently a dark state (low oscillator strength) that is difficult to populate via direct optical mechanisms. While it can be reached via excitation to the second anionic excited state, this would likely result in an energetically wasteful potential fluorescence. Given the energy discrepancy between input photon energy and that of the photoelectrons shown in the time resolved experiment, it would be expected that a fluorescence process from the minimum on the S_1 state near the CI would result in considerable energy being left in the molecule in the form of heat in various vibrational modes. This might preclude it from use as a biological chromophore. This difference in behaviour comes from the different position of a function group upon a ring system and the effect that has on the electronic states of the molecule.

4.6. References

1 The Nobel Prize in Chemistry 2008 - Press Release, https://www.nobelprize.org/nobel_prizes/chemistry/laureates/2008/press.html, (accessed 4 August 2017).
2 C. R. S. Mooney, D. A. Horke, A. S. Chatterley, A. Simperler, H. H. Fielding and J. R. R. Verlet, *Chem. Sci.*, 2013, **4**, 921–927.
3 R. Y. Tsien, *Annu. Rev. Biochem.*, 1998, **67**, 509–544.
4 M. Ormö, A. B. Cubitt, K. Kallio, L. A. Gross, R. Y. Tsien and S. J. Remington, *Science*, 1996, **273**, 1392–1395.
5 C. W. West, A. S. Hudson, S. L. Cobb and J. R. R. Verlet, *J. Chem. Phys.*, 2013, **139**, 071104.
6 A. V. Bochenkova, B. Klærke, D. B. Rahbek, J. Rajput, Y. Toker and L. H. Andersen, *Angew. Chem. Int. Ed.*, 2014, **53**, 9797–9801.
7 M. Zimmer, *Chem. Rev.*, 2002, **102**, 759–782.
8 W. Weber, V. Helms, J. A. McCammon and P. W. Langhoff, *Proc. Natl. Acad. Sci.*, 1999, **96**, 6177–6182.
9 M. Chattoraj, B. A. King, G. U. Bublitz and S. G. Boxer, *Proc. Natl. Acad. Sci. U. S. A.*, 1996, **93**, 8362–8367.
10 G. Bublitz, B. A. King and S. G. Boxer, *J. Am. Chem. Soc.*, 1998, **120**, 9370–9371.
11 N. M. Webber, K. L. Litvinenko and S. R. Meech, *J. Phys. Chem. B*, 2001, **105**, 8036–8039.
12 H. Morise, O. Shimomura, F. H. Johnson and J. Winant, *Biochemistry (Mosc.)*, 1974, **13**, 2656–2662.
13 H. Niwa, S. Inouye, T. Hirano, T. Matsuno, S. Kojima, M. Kubota, M. Ohashi and F. I. Tsuji, *Proc. Natl. Acad. Sci.*, 1996, **93**, 13617–13622.
14 J. B. Greenwood, J. Miles, S. D. Camillis, P. Mulholland, L. Zhang, M. A. Parkes, H. C. Hailes and H. H. Fielding, *J. Phys. Chem. Lett.*, 2014, **5**, 3588–3592.
15 S. B. Nielsen, A. Lapierre, J. U. Andersen, U. V. Pedersen, S. Tomita and L. H. Andersen, *Phys. Rev. Lett.*, 2001, **87**, 228102.
16 C. West, PhD thesis, Durham University, 2016.
17 C. W. West, J. N. Bull, A. S. Hudson, S. L. Cobb and J. R. R. Verlet, *J. Phys. Chem. B*, 2015, **119**, 3982–3987.
18 A. V. Bochenkova and L. H. Andersen, *Faraday Discuss.*, 2013, **163**, 297–319.
19 A. V. Bochenkova, Personal Communication, 2015.
20 M. E. Martin, F. Negri and M. Olivucci, *J. Am. Chem. Soc.*, 2004, **126**, 5452–5464.
21 A. Svendsen, H. V. Kiefer, H. B. Pedersen, A. V. Bochenkova and L. H. Andersen, *J. Am. Chem. Soc.*, 2017, **139**, 8766–8771.

5. Conclusions and Outlook

This chapter summarises the contents of the preceding chapters, with a brief discussion of the major conclusions, if any, to be drawn. This is followed by a discussion of possible future additions to the experimental setup to allow for a greater variety of possible molecules or control. Finally, this concludes with a look towards possible future research directs for the lab.

5.1. Summary

Chapter 1 provided a general review of the area of photoelectron spectroscopy, with emphasis on the techniques used in this lab. This included both time- and frequency-resolved spectroscopy. A general overview of the energy-storage and transfer mechanisms of atoms and molecules was covered to underpin the discussions made in the results chapters (chapters 3 & 4).

The design and construction of novel ion traps, guides and vacuum chambers for integration into an existing photoelectron spectrometer is presented in chapter 2. While the cryogenic cooling component is still under review and improvement, the other design improvements of the brief have been met. This was proved by using the new equipment to study new species of interest and even incorporate a new ion production methodology.

Chapter three discusses the study of anthracene and its carboxylic acid along with a discussion of the new in-source ion-fragmentation technique. This allowed for the production of previously impossible-to-study ions to be produced in significant quantity. The technique is not without flaws and being sure of the products of the fragmentation may restrict its use in the future. The most stable of the three isomers of the deprotonated anthracene ion was studied with a view to understanding the electron attachment mechanism for interstellar anion formation. To that end, it was found that autodetachment from resonances was the preferred decay mechanism for the anthacenyl anion, unlike that of the tetracenyl anion studied previously.[1]

Finally, chapter four describes the study of the *meta*- isomer of the chromophore for the green fluorescent protein (GFP). This included the full frequency-, angle- and time-resolved study of the molecule to unravel its intrinsic dynamics. In contrast to the more famous *para*- variation, the first excited state of the *meta*- isomer anion is well below threshold and is known to be formally dark with respect to photoexcitation. Access to this state can be achieved by excitation to the second anionic excited state which seems to undergo fast internal conversion onto the S_1

state potential energy surface. Signal from this state has a major long time-delay component, highlighting the presence of relatively stable configuration.

5.2. Possible Experimental Techniques

While one of the major outcomes of this thesis was the design and construction of an improved ion trap and guides for use with electrospray ionisation, other methods can provide alternative species of interest for study. Some examples are that of short lived radical species or species too reactive to be produced by electrospray ionisation. Further study of clusters has also shown to be highly informative but is currently impossible using the existing setup. Some of these could be studied by introducing a pulsed molecular beam into the experiment. As the experiment relies on the species of interest being anions, the beam would require ionisation and different methodologies would produce different products for study. Two possibilities are presented here.

Previous studies on oligonucleotides have made the technique of ion mobility spectrometry particularly appealing as complementary technique. A certain variation, known as trapped ion-mobility spectrometry separates molecules by their cross-section-to-charge ratio but in a much more confined space.[2] A few small changes could allow for a partial form of this technique to be implemented into the machine as described in Section 5.2.3.

5.2.1. Discharge Source

The introduction of a pulsed beam into the experiment has been attempted before. The ionisation method used previously was an electrical discharge. This pulse was positioned to arrive orthogonally to the central axis of the machine, and aimed to arrive at the centre of the TOF optics in R3, as shown in the schematic diagram Figure 2.1. The discharge was achieved by applying a constant high voltage between parallel meshes. Under standard vacuum conditions, no discharge was seen, the passage of a pulse of gas through the mesh lowered the breakdown voltage and

discharge occurred while the gas passed through the meshes. This high energy ionization technique can produce a huge variety of different products.[3]

This lab has previously attempted to study the anions of the fullerenes. These have been challenging to produce by electrospray using our setup. To this end a carbon-based discharge source has been designed but is as yet untested. The hope is that a carbon-based discharge may form the C_{60} radical anion in sufficient quantity for study. The discharge source consists of a ring applied to the end of a pulsed solenoid valve (Parker, General Valve, series 9) supporting a pair of graphite rods with their ends close together. In a similar manner to the previous discharge, the expectation is to apply a high potential difference between the rods that will inherently discharge at the passage of a gas pulse (Ar or He). The design is shown in Figure 5.1.

The material choice of the part is still under debate. A prototype has been produced using the lab's 3D printer using PLA thermoplastic. However, there are concerns that the heat generated by the discharge will melt the plastic. An alternative would be to construct the part from PTFE or a ceramic material.

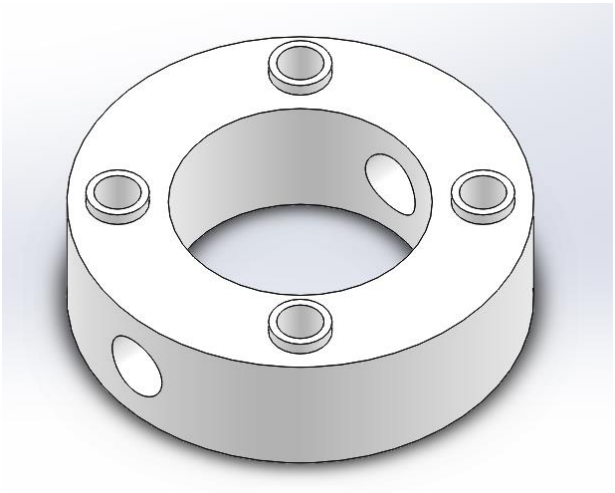

Figure 5.1 Representation of the intended carbon discharge source. The material used is currently under debate. The gas pulse is expected to pass vertically through the part, with the graphite rods held perpendicularly though the visible holes.

5.2.2. Ring Ioniser

While the high-energy ionisation sources discussed above are ideal for making otherwise challenging species, a softer electron-impact source would provide access to other species. A simple solution to this is to use an electron gun. This is often best positioned such that the electron beam is perpendicular to the gas pulse and the electron beam only interacts at one location while not being incident upon the source valve.

An alternative design has been proposed that would be more simply positioned .[4] The principle of operation is to force a ring of electrons to collapse radially though the gas pulse. This is achieved by a thoriated tungsten filament, seen in Figure 5.2, bent into a ring which produces electrons by thermionic emission upon the conduction of a current though the wire (typically a few amperes). This is supported by small coils of tungsten, again supported through ceramic tubes. Further out, the surround is pulsed to a negative potential, causing the electrons to move radially inwards through a grounded mesh. The grounded mesh is held inside to ensure the most linear field applied to the electrons and limit the effect on the subsequent ion beam.

This has been designed, but not yet implemented into the machine.

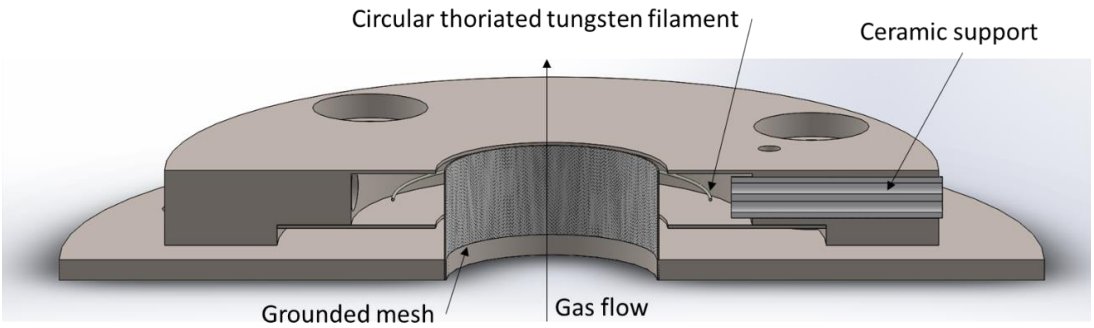

Figure 5.2 Cross section view of the ring ioniser.

5.2.3. Ion Mobility

Ion-mobility spectrometry (IMS) has come into its own for its ability to separate conformers by their collision cross section. The original form of IMS, known as drift-tube IMS, used an external electric field to move ions though a static gas. Trapped ion-mobility spectrometry (TIMS) uses a steady gas flow in one direction and uses an electric field to hold the ions in position against that flow.[2,5] By altering the applied electric field, a range of molecules with different charge-to-cross-section ratios can be investigated.

The conditions required for a TIMS operation are a constant flow of gas through a system with a radially confining electric field and a DC linear gradient applied along the length of the system. The pressures of gas required is usually of the order of 1-4 mbar (0.75 – 3 Torr).[2,5,6] This is all currently present within region one of the spectrometer.

A few crucial differences are worth noting. A TIMS analysis is inherently a pulsed process.[2] A visual representation is presented in Figure 5.3. The process begins with an accumulation phase where ions are introduced to the entrance funnel using a repulsive deflection plate. Ions pass through the entrance and into the analysis region and reach a point of equilibrium.

The equilibrium is reached when the drift velocity of the ions matches that of the buffer gas. Ions with a large collision cross-section, or low mobility coefficient, come to reside at positions high up the rising edge of the electric field shown in Figure 5.3 (b). Conversely, smaller or multiply-charged ions will reach a stable position nearer to the entrance of the analyser.

At some point later, the deflection plate is switched to an attractive potential so no more ions are able to enter the system. The ions are then left for another time period, often of the order of a few milliseconds, to allow for all the ions to reach their equilibrium position. Finally, the gradients are steadily reduced and ions are pushed from the analyser by the gas pressure, coming off in order of decreasing cross section.

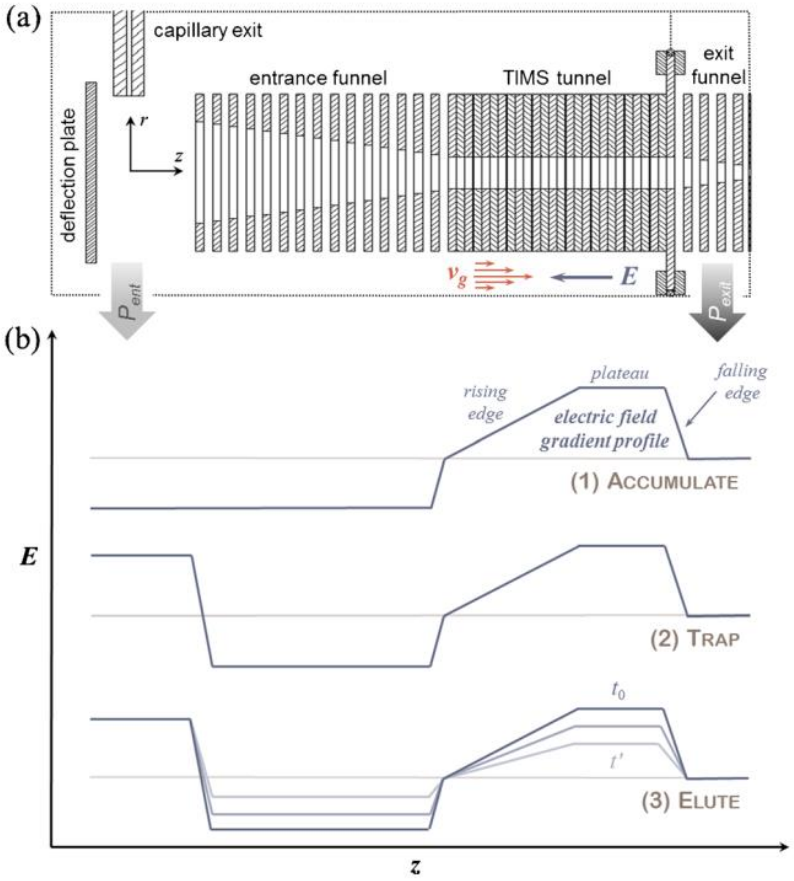

Figure 5.3 Schematic representation of a TIMS setup. (a) Cross section view of the physical components. (b) Representations of the three phases of a TIMS analysis. Reproduced from Ref. 2 With permission of Springer.

While this pulsed analysis would be difficult to implement in the current scheme due to the pressure and drift time in the subsequent region, a different possibility could be realised. Instead of using the system to acquire the full mobility spectrum of an incident electrospray source, it could be possible to use this as a filter, preventing the passage of multiply charged ions and allowing for the separate analysis of components with a higher collision cross-section.

5.3. Outlook

Looking to the future from the culmination of this work, it is obvious that work is required to finish optimising the trap parameters and in particular understand the unusual behaviour of the system under cryogenic cooling. As mentioned in section 2.3.4, the cooling process seems to induce some form of instability into the system, be it directly electronic or the result of changes in gas dynamics. The reduced pressure and cryopumping associated with the large reservoir would be expected to significantly alter the net movement of gas through the pinholes. Couple this with the requirement of introduced helium flow, the result is a system with a huge number of interconnecting factors that will require thorough and careful experimentation to fully explore and comprehend. However, I firmly believe that the system will work, but will require some further development before it is ready to be used as a cryogenic system for the study of a cooled molecule.

Once these issues have been resolved and cooling can be achieved upon the molecules of interest in the experiment, the obvious molecules to study would be to re-investigate the oligonucleuotides mentioned in section 2.1.3. Our previous work showed no drastic changes between the single unit and the start of a single strand. It has been shown that the system should prefer a stacked conformation and that this should be visible in the time-resolved spectra.[7,8]

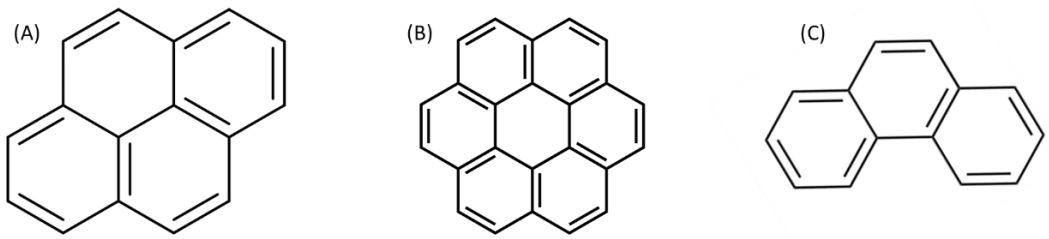

Figure 5.4 Structures of (A) pyrene, (B) coronene and (C) Phenanthrene.

In terms of moving on to different molecules, given the relative ease of the CID technique described in section 3.2.1, the use of this to study previously impossible compounds would be an exciting new avenue. An obvious direction would be to

continue with other polyaromatic hydrocarbons, such as pyrene and coronene, shown in Figure 5.4. After the reasonable level of success achieved in the production of the anthracenyl anion, the comparison between the teatracenyl and the pyrenyl anion would again be relevant from an astrophysical perspective for the formation of PAHs in the interstellar medium. Alternatively, a comparison could be drawn against the phenanthrene molecule to see if the simple movement of one ring relative to the others can make a difference to the dynamics. Experience from the *meta*- GFP chromophore would imply that there could be a marked difference.

5.4. References

1 J. N. Bull, C. W. West and J. R. R. Verlet, *Phys. Chem. Chem. Phys.*, 2015, **17**, 32464–32471.
2 K. Michelmann, J. A. Silveira, M. E. Ridgeway and M. A. Park, *J. Am. Soc. Mass Spectrom.*, 2015, **26**, 14–24.
3 M. A. Duncan, *J. Phys. Chem. A*, 2012, **116**, 11477–11491.
4 O. Cheshnovsky, 2016, Personal Communication.
5 J. A. Silveira, M. E. Ridgeway and M. A. Park, *Anal. Chem.*, 2014, **86**, 5624–5627.
6 J. A. Silveira, K. A. Servage, C. M. Gamage and D. H. Russell, *J. Phys. Chem. A*, 2013, **117**, 953–961.
7 J. Gidden and M. T. Bowers, *Eur. Phys. J. - At. Mol. Opt. Plasma Phys.*, 2002, **20**, 409–419.
8 A. S. Chatterley, C. W. West, G. M. Roberts, V. G. Stavros and J. R. R. Verlet, *J. Phys. Chem. Lett.*, 2014, **5**, 843–848.